NEAR-FIELD RADIATIVE ENERGY TRANSFER AT NANOMETER DISTANCES

A Dissertation
Presented to
The Academic Faculty

By

Soumyadipta Basu

In Partial Fulfillment
of the Requirements for the Degree
Doctor of Philosophy in the
School of Mechanical Engineering

Georgia Institute of Technology
December 2009

NEAR-FIELD RADIATIVE ENERGY TRANSFER AT NANOMETER DISTANCES

Approved by:

Dr. Zhuomin Zhang, Advisor
George W. Woodruff School of Mechanical Engineering
Georgia Institute of Technology

Dr. Yogendra Joshi
George W. Woodruff School of Mechanical Engineering
Georgia Institute of Technology

Dr. Peter J. Hesketh
George W. Woodruff School of Mechanical Engineering
Georgia Institute of Technology

Dr. Andrew F. Peterson
School of Electrical and Computer Engineering
Georgia Institute of Technology

Dr. David S. Citrin
School of Electrical and Computer Engineering
Georgia Institute of Technology

Date Approved: 10/15/2009

ACKNOWLEDGEMENTS

I am grateful to my PhD adviser Dr. Zhuomin Zhang for providing me with an opportunity to work in his research group and for his guidance and motivation throughout my PhD study. I would also like to thank my dissertation committee members, Dr. Peter Hesketh, Dr. Yogendra Joshi, Dr. Andrew Peterson, and Dr. David Citrin, for agreeing to serving on my committee and offering valuable advice. Special mention must also be made about my professors at Jadavpur University, India who encouraged me to aspire for graduate studies in the United States. The financial support from the National Science Foundation and the Department of Energy is much appreciated.

Throughout my PhD study I have benefited immensely from my interactions with my former and present colleagues of the nanoscale thermal radiation laboratory. I have enjoyed fruitful collaborations with Dr. Yu-bin Chen, Dr. Keunhan Park, Dr. Bong Jae Lee, Liping Wang, and Xiaojia Wang. I would cherish my association with Andrew McNamara, Trevor Bright, and Qinghe Li.

My PhD study would not have been possible without the support and encouragement of my family and friends back in India. My parents and my brother have been pillars of support for me and have always been there for me through the thick and thin of my PhD. The love and encouragement of my parents-in-law have made my study easier. Finally, I wish to thank my wife Arunima Basu for her constant encouragement.

TABLE OF CONTENTS

LIST OF TABLES

LIST OF FIGURES

LIST OF SYMBOLS AND ABBREVIATIONS

c speed of light in vacuum, 2.998×10^{8} m s^{-1}

d vacuum gap thickness, m

D density of states, s rad^{-1} m^{-3}

e electron charge, 1.602×10^{-19} C

$\mathbf{E}$ electric field vector, V m^{-1}

$\overline{\overline{\mathbf{G}}}$ dyadic Green function, m^{-1}

$\mathbf{H}$ magnetic field vector, A m^{-1}

$\hbar$ Planck constant divided by 2π, 1.055×10^{-34} J s

$\mathbf{j}$ fluctuating current density, A m^{-2}

$\mathbf{k}$ wavevector, m^{-1}

k_{B} Boltzmann constant, 1.381×10^{-23} J K^{-1}

m^{*} carrier effective mass, kg

N carrier concentration, cm^{-3}

q'' Heat flux, W m^{-2}

$\mathbf{r}$ vector in the radial direction, m

r Fresnel reflection coefficient

$\mathbf{S}$ spectral Poynting vector, W m^{-2} s rad^{-1}

u energy density, J m^{-3}

T Temperature, K

t Fresnel transmission coefficient

$\mathbf{z}$ vector in the direction normal to surfaces, m

Greek symbols

β parallel wavevector component, m^{-1}

γ wavevector component in the z-direction, m^{-1}; also scattering rate, rad s^{-1}

ε relative permittivity (i.e., dielectric function)

ε_0 permittivity of vacuum, 8.854×10^{-12} F m^{-1}

Θ mean energy of the Planck oscillator, J

κ extinction coefficient

λ wavelength in vacuum, m

μ mobility, cm^2 V^{-1} s^{-1}

μ_0 permeability of vacuum, $4\pi \times 10^{-7}$ H m^{-1}

ρ resistivity, $\Omega \cdot$cm

σ Stefan-Boltzmann constant, 5.67×10^{-8} W m^{-2} K^{-4}

τ relaxation time, s

ω angular frequency, rad s^{-1}

Superscripts

p *p* polarization

s *s* polarization

Subscripts

0 vacuum

1 medium 1

2 medium 2

c critical

E electric

evan evanescent wave

M magnetic

max maximum

opt optimum

p plasma

SUMMARY

Near-field thermal radiation which can exceed blackbody radiation by several orders of magnitude has potential applications in energy conversion devices, nanofabrication, and near-field imaging. The present dissertation provides a comprehensive and thorough investigation of near-field heat transfer between parallel plates at nanometer distances.

The first part of this dissertation focuses on the fundamentals of nanoscale thermal radiation through a systematic study on the near-field heat transfer between doped Si plates. In order to calculate the near-field heat transfer, it is important to accurately predict the dielectric function of doped Si. The dielectric function of doped Si which is described by the Drude model is a function of carrier concentration and mobility. Hence, accurate ionization and carrier mobility models for both *p*- and *n*-type Si are identified after a careful review of the available literature. The radiative properties calculated using the improved dielectric function agrees to a good extent with measurements performed using a FTIR. The near-field heat transfer between doped Si plates at varying doping levels is then calculated using the improved dielectric functions. Several important and characteristic features of near-field radiation are revealed in the analysis. An interesting issue regarding the maximum achievable nanoscale thermal radiation arises out of the study on near-field heat transfer in doped Si.

The second part of this dissertation investigates the maximum achievable near-field thermal radiation between two plates at finite vacuum gaps. Initially, both the emitter and the receiver are assumed to have identical frequency-independent dielectric functions and a cut off in the order of the lattice spacing is set on the upper limit of the

wavevector. The energy transfer is maximum when the real part of dielectric function is around −1 due to surface waves. On the other hand, there is a strong relationship between the imaginary part of the dielectric function and the vacuum gap. While the study using frequency independent dielectric function is not realistic, it lays down the guidelines for the parametric optimization of dielectric functions of real materials for achieving maximum near-field heat transfer. A parametric study of the different adjustable parameters in the Drude and Loretz model is performed in order to analyze their effect on the near-field heat transfer. It is seen that the optimized Drude model always results in greater near-field heat transfer compared to the Lorentz model and the maximum achievable near-field heat transfer is nearly 1 order greater than that between real materials.

In the third part of this dissertation, the unusual penetration depth and the energy streamlines in near-field thermal radiation are studied. It is seen that unlike far-field radiation, the penetration depth in near-field heat transfer is dependent on the vacuum gap. This unusual feature results in a 10 nm thick SiC film behaving as completely opaque when the vacuum gap is around 10 nm. The energy streamlines inside the emitter, receiver, and the vacuum gap are calculated using fluctuation electrodynamics and errors generated due to thin film optics are pointed out. It is seen that the lateral shift of the streamlines inside the emitter can be greater than that in the vacuum gap for SiC. However, for doped Si, the lateral shift is comparable in the different media. While the study on the penetration depth determines the thickness of the emitter, the streamlines determine the lateral dimension.

CHAPTER 1

INTRODUCTION

The Stefan-Boltzmann law predicts the maximum radiative heat flux between two flat plates separated by vacuum to be $\sigma(T_1^4 - T_2^4)$, where σ is the Stefan-Boltzmann constant and T_1 and T_2 are the temperatures of the two media, respectively. This law, however, is only applicable when the two emitting/absorbing bodies are separated by a distance d much greater than the characteristic wavelength of thermal radiation (λ_T) that can be obtained from Wien's displacement law (Siegel and Howell, 2002). As the distance decreases and becomes comparable with or shorter than λ_T, near-field effects become important and ray optics can no longer be used to obtain the energy transfer between the two bodies.

The spacing effect on the net heat transfer arises from two effects that are interrelated. The first is wave interference that is important when d is close to but greater than λ_T. In such cases, radiative transfer between two bodies must be analyzed by considering the wave nature of energy propagation. An electromagnetic wave emitted from one medium, which is transmitted to the vacuum gap separating the two bodies, is subject to multiple reflections inside the gap. The resulting wave interference can be either constructive or destructive, depending on the phase differences between the multiply reflecting waves. The second spacing effect is due to photon tunneling that contributes significantly to near-field energy transfer when $d < \lambda_T$. When an electromagnetic wave traveling in a medium encounters a second medium which is optically rarer than the first one, it exhibits total internal reflection at the interface when

the angle of incidence is greater than the critical angle. Though the wave is totally reflected inside the first medium, there exists an evanescent wave in the second medium whose amplitude decays exponentially from the interface (Cravalho *et al*., 1967; Zhang, 2007). The evanescent wave does not carry energy in the normal direction since the time average of the Poynting vector normal to the interface is zero. On the other hand, if a third medium with refractive index greater than the second medium is brought in close vicinity to the first medium, i.e., within the decay length of the forward evanescent wave, the evanescent wave gets reflected at the interface between the second and the third media. The Poynting vector of the coupled evanescent fields has a nonzero normal component, suggesting that energy from the first medium has tunneled through the second medium and reached the third medium. This phenomenon is known as photon tunneling or radiation tunneling, which is the key for enhanced energy transfer in the near field (Zhang, 2007). The near-field heat transfer between the two SiC plates at 1 nm apart near room temperature can exceed blackbody radiation by five orders of magnitude.

The possibility of achieving enhanced energy transfer in the near field has attracted much attention of many researchers during the past half a century. Initial studies were mostly devoted towards understanding the fundamentals of near-field radiation between semi-infinite plates made of different materials. A number of studies have also been performed regarding application of near-field thermal radiation in energy systems (Pan *et al*., 2000; Whale and Cravalho, 2002; Narayanaswamy and Chen, 2003; Laroche *et al*., 2006; Park *et al*., 2008), nano-fabrication (Liu *et al*., 2005; Wang *et al*., 2006; Lee *et al*., 2008), and near-field imaging (De Wilde *et al*., 2006). Recently Basu *et al*. (2009c)

presented a detailed review about the fundamentals and applications of near-field radiation in energy systems.

Fast depleting reserves of conventional energy sources coupled with the ever increasing levels in the emission of greenhouse gases have forced the scientific community to seek alternative power generation technologies. Thermophotovoltaic (TPV) systems, which operate on the principle similar to that of solar cells, have been looked upon as one of the possible candidates for alternative electrical power generation due to their silent operation and versatility in the fuel usage. However, lower throughput and poor conversion efficiencies have restricted the use of TPV systems as portable power sources (Basu *et al*., 2007). A possible method of improving the performance of TPV systems is by employing micro/nanoscale radiation to the energy conversion. For example, the conversion efficiency can be improved by using micro/nanostructured emitter or filter, while the power throughput can be enhanced by placing the TPV cell close to the emitter and utilizing the near-field enhancement in the radiative energy transfer for power generation. This new type of TPV systems called near-field thermophotovoltaic systems has recently attracted much attention (Di Matteo *et al*., 2004; Laroche *et al*., 2006; Park *et al*., 2008).

Another important application of near-field radiation is in the field of nanomanufacturing. Enhanced transmission of metallic films perforated with subwavelength holes as shown by Ebbesen *et al*. (1998) stirred the interest in studying light transmission through nanostructures. It is believed that the coupled and localized surface polaritons and Fabry-Perot type resonances are responsible for the transmission enhancement through nanostructures. Liu *et al*. (2005) proposed a new nanolithography

technique based on the interference of surface plasmon waves. This technique can break the diffraction limit of light and can pattern 1-D or 2-D periodical structures of 40-100 nm features. Wang *et al*. (2006) used bowtie shaped aperture to produce sub-50-nm holes in a positive photoresist. Such nanoapertures behave as an antenna to collect light and then focus it in the near field. Large transmission enhancement and strong field localization have also been predicted from nanoscale Al slit arrays with mid-infrared radiation and may be used for nanolithography (Lee *et al*., 2008).

Near-field radiation has also been used for imaging beyond the diffraction limit. De Wilde *et al*. (2006) developed an infrared near-field scanning optical microscope (NSOM) which utilizes the thermal infrared evanescent fields emitted by the surface to be imaged and do not require any external illumination. Termed as the Thermal Radiation Scanning Tunneling Microscope, it utilizes a tungsten tip oscillating perpendicular to the surface to be imaged. The tip acts as a scattering center and radiates in the far field a signal linearly related to the infrared evanescent fields emitted by the surface. Kittel *et al*. (2008) showed that a near-field scanning thermal microscope can be employed for nanoscale imaging of structures. These microscopes measure the local density of states.

Theoretical studies on near-field enhancement have been performed between parallel surfaces, two dipoles, or dipole and a flat surface. Rytov and coworkers were the first to propose fluctuational electrodynamics, by introducing the fluctutation-dissipation theorem to Maxwell's equations, for the analysis of thermal radiation (see Rytov *et al*., 1987). Cravalho *et al*. (1967) predicted the near-field energy transfer between two dielectrics at liquid-helium temperature separated by a vacuum gap. Polder and Van Hove (1971) employed fluctuational electrodynamics and predicted a near-field

enhancement between metallic materials. Loomis and Maris (1994) investigated the effect of resistivity on near-field energy transfer between two materials whose dielectric functions were modeled by a simplified Drude model. Pendry (1999) introduced the concept of wave vectors as channels of radiative transfer and developed a relationship between the real and imaginary parts of the reflection coefficients of the two emitting media required for the maximum achievable near-field enhancement. Mulet *et al*. (2002) predicted that the near-field heat transfer between dielectrics supporting surface phonon polaritons is dominated by the contribution from surface waves and, hence, the heat flux becomes nearly monochromatic at nanometric distances. Volokitin and Persson (2004) extended Pendry's study and obtained the maximum achievable near-field heat transfer. Fu and Zhang (2006) studied the near-field heat transfer between doped Si media at different doping levels. Chapuis e*t al*. (2008a) calculated the near-field heat transfer between two semi-infinite gold plates using two different nonlocal dielectric function models and compared their results with the heat transfer computed using the Drude model. Recently, Francoeur *et al*. (2009) analyzed near-field thermal radiation in one-dimensional layered media using Dyadic Green's function where the amplitude of the field in each layer was calculated via a scattering matrix approach. By using the scattering matrix technique they were able to circumvent the numerical instabilities in the commonly used transfer matrix formulation for multilayer geometries. Ben-Abdallah *et al*. (2009) investigated the effect of film thickness on the near-field heat transfer between two thin films. As the vacuum gap decreases, the influence of film thickness on the energy transfer decreases due to the reduction in the penetration depth of the evanescent waves.

Among other geometries, Mulet *et al*. (2001) studied the near-field heat transfer between a particle (modeled as a point-like dipole) and a semi-infinite plane medium, separated by vacuum. Both the particle and the plane medium were taken as SiC. It was predicted that the near-field heat transfer increases as d^{-3}, where d is the separation between the particle and the plane medium. The near-field radiative transfer between two spherical particles and that between a spherical particle and a flat surface were also calculated by Volokitin and Persson (2001) under proximity limit approximation. Chapuis *et al*. (2008b) investigated the radiative heat transfer between two nanoparticles in the near field and far field. They showed that the heat transfer was dominated by electric dipole-dipole interaction for identical dielectric particles and by magnetic dipole-dipole interaction for identical metallic particles. Both the metallic and dielectric particles exhibit the same d^{-6} dependence for the near-field heat flux. Narayanaswamy and Chen (2008) developed a more general formulation for the near-field heat transfer between two spheres of arbitrary diameters without taking into account the dipole or proximity assumption as employed by previous researchers. By nondimensionalizing the sphere radius with respect to the vacuum gap and wavelength, they constructed a regime map showing the applicability of different solution techniques. Recently, Biehs (2008) studied the near-field radiative heat transfer and local density of states between a metallic nanosphere and a semi-infinite structured surface.

Along with the theoretical studies, experiments have also been performed to measure the near-field radiative transfer by different research groups. Domoto *et al*. (1970) measured the radiative heat transfer at cryogenic temperatures between two copper plates at gaps from 1 mm to 10 μm. While the near-field heat transfer was 2.3

times greater than that of far-field, the measured heat flux was only 3% of the energy transfer between blackbodies. Hargreaves (1969,1973) measured the near-field heat transfer between two chromium plates separated by vacuum gaps from 6 to 1.5 μm. At 1.5 μm vacuum gap, the near-field heat transfer at room temperature was 5 times greater than that in the far field. However, the measured heat flux was still only 40% of that between two blackbodies. Xu *et al.* (1994) were the first to measure near-field heat transfer between indium needle and gold plates at vacuum gaps less than 1 μm in order to analyze the heat transfer between the probe and the sample in a scanning thermal profiler (Williams and Wickramasinghe, 1986). The minimum achievable vacuum gap was estimated to be 12 nm. The results showed a smaller heat transfer rate and weaker distance dependence than those predicted; this may be attributed to the lack of sensitivity in the experiments. Kittel *et al*. (2005) measured the near-field heat transfer between the tip of a scanning thermal microscope and gold or gallium nitride plates for vacuum gaps from 100 nm to 1 nm. For vacuum gaps greater than 10 nm, their measurements clearly showed near-field enhancement and agreed well with predicted values. However for gaps less than 10 nm, the measured heat flux saturates and differs from the divergent behavior of the predicted results. The authors attributed this difference to the spatial dependence of the dielectric function of materials. Hu *et al*. (2008) measured the near-field heat transfer near room temperature between two parallel glass plates which support surface phonon polaritons in the infrared region. The measured near-field heat flux exceeded that between two blackbodies by 35 % when the vacuum gap was 1.6 μm. Narayanaswamy *et al*. (2008) developed a sensitive technique for measuring near-field radiation between a silica microsphere and a glass substrate using bimaterial atomic force microscope

cantilevers as thermal sensors. Using this setup, the maximum measured conductance due to near-field radiation at 100 nm vacuum gap was 20% greater than that between two blackbodies. Shen *et al*. (2009) measured the near-field heat transfer between silica microsphere and substrates made of doped Si, Au, and glass down to a vacuum gap of 30 nm. Of the different substrates, glass provided the maximum near-field enhancement due to coupling of surface phonon polaritons at the two interfaces.

This dissertation is devoted to a thorough analysis of near-field energy transfer at nanometer distances between two semi-infinite plane media. To start with, infrared radiative properties of heavily doped Si are experimentally investigated near room temperature. Accurate carrier mobility and ionization models are identified via a critical review of available literature and then incorporated in to a Drude model to predict the dielectric function of heavily doped Si. The calculated radiative properties of several samples are compared with those measured with a Fourier-transform infrared spectrometer. The improved dielectric function model is then employed to calculate near-field radiative energy transfer between two semi-infinite Si plates using fluctuational electrodynamics. The effects of doping level, polarization, and vacuum-gap width on the spectral and total radiative transfer are studied. An intriguing question in nanoscale thermal radiation has been the existence of an upper limit of the heat transfer between two media as the separation distance is arbitrarily reduced. This issue is addressed here by calculating the maximum achievable near-field heat transfer between two parallel plates separated at very small distances. Initially, frequency-independent dielectric functions are considered to determine what combinations of the real and imaginary parts of the dielectric function will maximize the heat transfer. This is followed by a

parametric optimization of the Drude and the Lorentz model for maximum achievable near-field heat transfer in realistic material systems. A better understanding of the surface wave effect on near-field heat transfer is thus obtained. Furthermore, it is found that, unlike far-field radiation, the penetration depth during near-field heat transfer depends on the vacuum gap thickness in addition to material properties. Consequently, a 10 nm thick SiC film can become essentially opaque when the vacuum gap is less than 10 nm. In addition to the calculation of near-field energy transfer between the two media, it is important to understand the direction of energy flow between them. An improved algorithm that is consistent with the fluctuational electrodynamics is developed to correctly trace the energy streamlines, representing the direction of energy flow, inside the emitter, receiver, and the vacuum gap. The results obtained from this research will facilitate the future design of MEMS devices and applications of nanoscale radiation for energy harvesting.

CHAPTER 2

THEORETICAL BACKGROUND

This Chapter provides theoretical background necessary for the analysis of near-field radiative heat transfer between two parallel plates. To start with, a brief discussion about fluctuation-dissipation theorem and dyadic Green's function is provided in Section 2.1. In section 2.2, dielectric functions of different materials are discussed. Section 2.3 analyzes density of states and the role of surface polaritons in near-field heat transfer.

2.1 Fluctuation-dissipation Theorem and Dyadic Green's Function

Thermal radiation between solids is often treated as a surface phenomenon and analyzed using ray optics with the assistance of the concept of emissivity, reflectivity and absorptivity of the surfaces (Siegel and Howell, 2002). On the other hand, radiation heat transfer inside a semitransparent medium is traditionally dealt with by the radiative transfer equation (RTE), considering emission, absorption, and scattering (Siegel and Howell, 2002). These phenomenological approaches do not fully account for the origin of thermal emission and break down when wave interference and diffraction become important.

According to the fluctuation-dissipation theorem, thermal emission is originated from the fluctuating currents induced by the random thermal motion of charges, known as thermally induced dipoles. Furthermore, Maxwell's equations describe the propagation of electromagnetic waves and their interactions with matter. The fluctuational electrodynamics, pioneered by Rytov and co-workers in 1950s combined the fluctuation-dissipation theorem with Maxwell's equations to fully describe the emission, propagation,

and absorption of thermal radiation in both the near and far field (Rytov *et al*., 1987). The random thermal fluctuations produce a spatial and time-dependent electric current density $\mathbf{j}(\mathbf{x},t)$ inside the medium whose time average is zero. The time-dependent current density can be decomposed into $\mathbf{j}(\mathbf{x},\omega)$ in the frequency domain using the Fourier transform. The inclusion of the fluctuating current in Ampere's law makes the Maxwell equations stochastic in nature (Loomis and Maris, 1994). For prescribed geometric conditions and temperature distribution, Maxwell's equations need to be solved in order to obtain the electric and magnetic fields. This can be done with the help of the dyadic Green's function, which makes the formulations simple and compact.

With the assistance of the dyadic Green's function $\overline{\overline{\mathbf{G}}}(\mathbf{x},\mathbf{x}',\omega)$, the induced electric and magnetic fields due to the fluctuating current density can be expressed in the frequency domain as a volume integration:

$$\mathbf{E}(\mathbf{x},\omega) = \mathrm{i}\omega\mu_0 \int_V \overline{\overline{\mathbf{G}}}(\mathbf{x},\mathbf{x}',\omega)\cdot\mathbf{j}(\mathbf{x}',\omega)\mathrm{d}\mathbf{x}' \tag{2.1}$$

$$\mathbf{H}(\mathbf{x},\omega) = \int_V \nabla\times\overline{\overline{\mathbf{G}}}(\mathbf{x},\mathbf{x}',\omega)\cdot\mathbf{j}(\mathbf{x}',\omega)\mathrm{d}\mathbf{x}' \tag{2.2}$$

where μ_0 is the magnetic permeability of vacuum, and the integral is over the region V that contains the fluctuating sources. Detailed discussions about the solution of Maxwell's equations can be obtained from Francoeur and Menguc (2008). The dyadic Green's function, $\overline{\overline{\mathbf{G}}}(\mathbf{x},\mathbf{x}',\omega)$ is essentially a spatial transfer function between a current source $\mathbf{j}$ at a location $\mathbf{x}'$ and the resultant electric field $\mathbf{E}$ at $\mathbf{x}$ (Mulet *et al.*, 2002; Fu and Zhang, 2006). Based on the ergodic hypothesis, the spectral energy flux is given by (Basu *et al*., 2009b)

$$\left\langle \mathbf{S}(\mathbf{x},\omega)\right\rangle = \int_0^\infty \frac{1}{2}\left\langle \mathrm{Re}[\mathbf{E}(\mathbf{x},\omega)\times\mathbf{H}^*(\mathbf{x},\omega')]\right\rangle \ \mathrm{d}\omega' \tag{2.3}$$

where <> represents ensemble averaging, **S** is the spectral Poynting vector, ω and ω' are the angular frequencies, and * denotes the complex conjugate. In order to obtain the spectral energy flux, it is important to know the ensemble average of the spatial correlation function of the fluctuating current densities which acts as the source for thermal radiation. The spectral density of the fluctuating currents is related to the local temperature of the body through the fluctuation-dissipation theorem. The ensemble average of the fluctuating current densities is given by (Joulain *et al.*, 2005)

$$\left\langle j_m(\mathbf{x}',\omega)\, j_n{}^*(\mathbf{x}'',\omega')\right\rangle = \frac{4}{\pi}\omega\varepsilon_0\,\mathrm{Im}(\varepsilon(\omega))\delta_{mn}\delta(\mathbf{x}'-\mathbf{x}'')\Theta(\omega,T)\delta(\omega-\omega') \tag{2.4}$$

where j_m and j_n (m, n = 1, 2, or 3) stands for the x, y, or z component of **j,** δ_{mn} is the Kronecker delta and $\delta(\omega-\omega')$ is the Dirac delta function. In Eq. (2.4), $\Theta(\omega,T)$ is the mean energy of a Planck oscillator at frequency ω in thermal equilibrium and is given by

$$\Theta(\omega,T) = \frac{\hbar\omega}{\exp(\hbar\omega/k_\mathrm{B}T)-1} \tag{2.5}$$

where $\hbar$ is the Planck constant divided by 2π, k_B is the Boltzmann constant, and T is the absolute temperature of the source medium. In Eq. (2.5), the term $\frac{1}{2}\hbar\omega$ that accounts for vacuum fluctuation is omitted since it does not affect the net radiation heat flux. A factor of 4 has been included in Eq. (2.4) to be consistent with the conventional definitions of the spectral energy density and the Poynting vector expressed in Eq. (2.3) since only positive values of frequencies are considered here (Fu and Zhang, 2006).

It should be noted that Eq. (2.4) assumes that the dielectric function is a scalar (isotropic media) and independent of the wavevector (local assumption). In the extreme

proximity (less than 1 nm distance), the dielectric function is not *local* and its dependence on wavevector must be considered (Joulain, 2008). Recently, Chapuis *et al*. (2008a) used two different non-local dielectric function models to calculate the near-field heat transfer between two semi-infinite gold plates and compared their results with the heat flux calculated using the Drude model for gold. The heat flux for *s* polarization is identical for both local and non-local dielectric function models. On the other hand, for *p* polarization, the heat flux predicted using the two different dielectric models starts to differ when the vacuum gap is less than 0.1 nm. While, the non-local dielectric function saturates the heat flux, using local dielectric function will cause the heat flux to diverge as the vacuum gap $d \to 0$. In this dissertation, only the local form of dielectric function models is considered since they are valid for most practical problems encountered.

The somewhat modified expression of the spectral energy flux in Eq. (2.3) as compared to earlier publications (Fu and Zhang, 2006; Park *et al.*, 2008) is due to the fact that the Dirac delta function $\delta(\omega - \omega')$ has been included in the spatial correlation function of the currents in Eq. (2.4). At first sight, it might appear that using the expression of spectral energy flux as mentioned by Fu and Zhang (2006) and Park *et al*. (2008) will cause some inconsistency in units. It should be noted that the expression for the fluctuating current densities in those studies was obtained after an integration of Eq. (2.4) over ω'. Hence, the final results obtained from these references are consistent with other publications.

Consider near-field radiative heat transfer between two semi-infinite solids separated by a vacuum (or a dielectric medium in some studies), as illustrated in Fig. 2.1. Both media are nonmagnetic, isotropic, and homogeneous. Furthermore, each medium is

assumed to be at a thermal equilibrium, which is often reasonable due to the relatively large thermal conductivity of solid materials. As shown in Fig. 2.1, a vacuum gap of width d separates the two parallel and smooth surfaces of the semi-infinite media at temperatures T_1 and T_2, respectively. In this study, it is always assumed that medium 1 (emitter) is at a higher temperature than medium 2 (receiver). Note that the radiative energy from the lower-temperature medium to the higher-temperature medium must also be considered. The random motion of the dipoles represented as ellipses in the figure results in a space-time dependent fluctuating electric field, **E**. Cylindrical coordinate system is used so that the space variable $\mathbf{x} = \mathbf{r} + \mathbf{z}$, with r-direction being parallel to the interface and z-direction perpendicular to the interface. β and γ_j refer to the r-component and z-component of the wavevector $\mathbf{k}_j$, respectively. Thus, $\mathbf{k}_j = \beta\hat{\mathbf{r}} + \gamma_j\hat{\mathbf{z}}$ and $k_j^2 = \beta^2 + \gamma_j^2$, for j = 0, 1, and 2. The magnitude of $\mathbf{k}_j$ is related to the dielectric function ε_j by $k_0 = \omega/c$, $k_1 = \sqrt{\varepsilon_1}\ \omega/c$, and $k_2 = \sqrt{\varepsilon_2}\ \omega/c$, with c being the speed of light in vacuum and ε_1 and ε_2 being the dielectric functions (or relative permittivity) of medium 1 and 2, respectively. With the relationship between the fluctuating current densities and the temperature of the emitting medium being established through Eq. (2.4), the spectral energy flux can now be calculated once the dyadic Green's function, $\overline{\overline{\mathbf{G}}}(\mathbf{x}, \mathbf{x}', \omega)$ is obtained. The dyadic Green's function depends on the geometry of the physical system and for two semi-infinite media shown in Fig. 1, it takes the following form (Sipe, 1987),

$$\overline{\overline{\mathbf{G}}}(\mathbf{x}, \mathbf{x}', \omega) = \int_0^\infty \frac{\mathrm{i}}{4\pi\gamma_1}\left(\hat{\mathbf{s}}t_{12}^{\mathrm{s}}\hat{\mathbf{s}} + \hat{\mathbf{p}}_2 t_{12}^{\mathrm{p}}\hat{\mathbf{p}}_1\right)\mathrm{e}^{\mathrm{i}(\gamma_2 z - \gamma_1 z')}\mathrm{e}^{\mathrm{i}\beta(r-r')}\beta\,\mathrm{d}\beta \tag{2.6}$$

where $\mathbf{x} = r\hat{\mathbf{r}} + z\hat{\mathbf{z}}$ and $\mathbf{x}' = r'\hat{\mathbf{r}} + z'\hat{\mathbf{z}}$. t_{12}^{s} and t_{12}^{p} are the transmission coefficients from

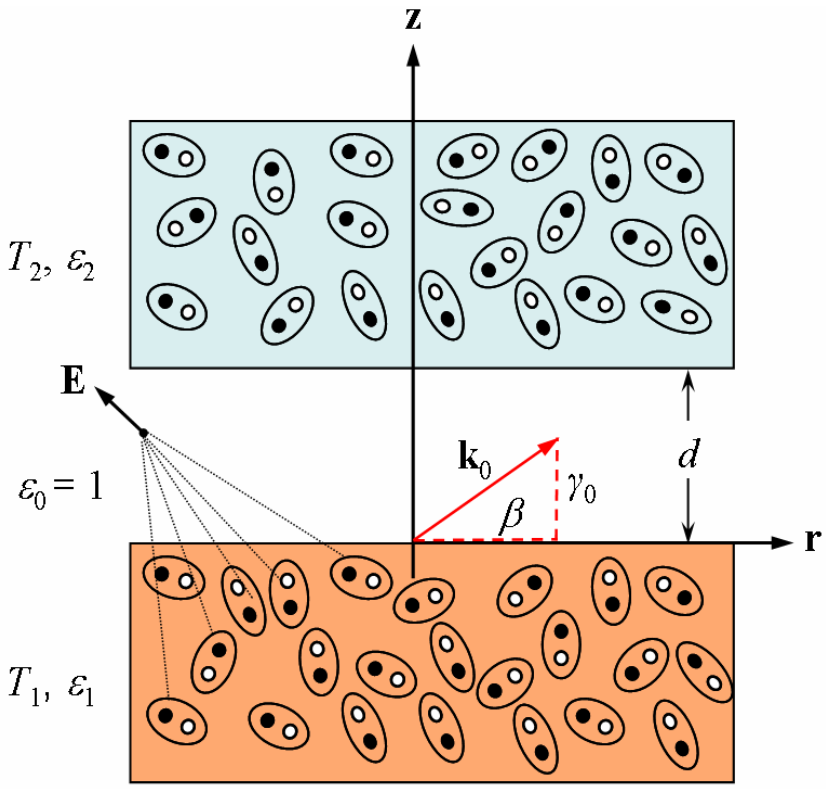

Figure 2.1 Schematic for near-field radiation between two closely placed parallel plates at temperatures T_1 and T_2, separated by a vacuum gap d. The random motion of the charges results in a time-dependent fluctuating electric field.

medium 1 to medium 2 for *s* and *p* polarizations, respectively, which are given by Airy's formula (Zhang, 2007). The unit vectors are $\hat{\mathbf{s}} = \hat{\mathbf{r}} \times \hat{\mathbf{z}}$, $\hat{\mathbf{p}}_1 = \left(\beta \hat{\mathbf{z}} - \gamma_1 \hat{\mathbf{r}}\right)/k_1$, and $\hat{\mathbf{p}}_2 = \left(\beta \hat{\mathbf{z}} - \gamma_2 \hat{\mathbf{r}}\right)/k_2$. Note that the Green's function in Eq. (2.6) helps to calculate the energy transferred from the emitter to the receiver and vice versa.

The net energy flux between the two media is (Basu and Zhang, 2009)

$$q''_{\text{net}} = \frac{1}{\pi^2}\int_0^\infty \mathrm{d}\omega \left[\Theta(\omega, T_1) - \Theta(\omega, T_2)\right] \int_0^\infty s(\omega, \beta)\,\mathrm{d}\beta \tag{2.7}$$

Note that the integration of $s(\omega,\beta)$ over β gives a weighted function to modify the Planck blackbody distribution function. Expression of $s(\omega,\beta)$ is different for propagating ($\beta < \omega/c$) and evanescent ($\beta > \omega/c$) waves,

$$s_{\text{prop}}(\omega,\beta) = \frac{\beta(1-\rho_{01}^{\text{s}})(1-\rho_{02}^{\text{s}})}{4\left|1-r_{01}^{\text{s}}r_{02}^{\text{s}}\text{e}^{\text{i}2\gamma_0 d}\right|^2} + \frac{\beta(1-\rho_{01}^{\text{p}})(1-\rho_{02}^{\text{p}})}{4\left|1-r_{01}^{\text{p}}r_{02}^{\text{p}}\text{e}^{\text{i}2\gamma_0 d}\right|^2} \tag{2.8}$$

and

$$s_{\text{evan}}(\omega,\beta) = \frac{\text{Im}(r_{01}^{\text{s}})\,\text{Im}(r_{02}^{\text{s}})\beta\text{e}^{-2\text{Im}(\gamma_0)d}}{\left|1-r_{01}^{\text{s}}r_{02}^{\text{s}}\text{e}^{-2\text{Im}(\gamma_0)d}\right|^2} + \frac{\text{Im}(r_{01}^{\text{p}})\,\text{Im}(r_{02}^{\text{p}})\beta\text{e}^{-2\text{Im}(\gamma_0)d}}{\left|1-r_{01}^{\text{p}}r_{02}^{\text{p}}\text{e}^{-2\text{Im}(\gamma_0)d}\right|^2} \tag{2.9}$$

In Eqs. (2.8) and (2.9), the first term on the right-hand side refers to the contribution of *s* polarization or TE wave, while the second term refers to the contribution of *p* polarization or TM wave. Note that $r_{0j}^{\text{s}} = \left(\gamma_0 - \gamma_j\right)\big/\left(\gamma_0 + \gamma_j\right)$ and $r_{0j}^{\text{p}} = \left(\varepsilon_j\gamma_0 - \gamma_j\right)\big/\left(\varepsilon_j\gamma_0 + \gamma_j\right)$ are the Fresnel reflection coefficients for *s* and *p* polarization, respectively, at the interface between vacuum and medium *j* (1 or 2). On the other hand, $\rho_{0j} = \left|r_{0j}\right|^2$ is the far-field reflectivity at the interface between vacuum and medium *j*.

For evanescent waves, when $\beta >> \omega/c$, $\gamma_1 \approx \gamma_2 \approx \gamma_0 \approx \text{i}\beta$. As a result, r_{01}^{s} and r_{02}^{s} are negligibly small, and the contribution of TE waves can be ignored. Furthermore, $r_{01}^{\text{p}} \approx \dfrac{\varepsilon_1 - 1}{\varepsilon_1 + 1}$ and $r_{02}^{\text{p}} \approx \dfrac{\varepsilon_2 - 1}{\varepsilon_2 + 1}$ are independent of β. Hence, Eq. (2.9) can be simplified as,

$$s_{\text{evan}}(\omega,\beta) \approx \frac{\beta\,\text{Im}(r_{01}^{\text{p}})\,\text{Im}(r_{02}^{\text{p}})\,\text{e}^{-2\beta d}}{\left|1-r_{01}^{\text{p}}r_{02}^{\text{p}}\,\text{e}^{-2\beta d}\right|^2} \tag{2.10}$$

As shown recently by Chapuis *et al*. (2008a), for metals, the contribution from TE waves is more significant when $\omega/c \ll \beta \ll \sqrt{|\varepsilon_1|}\,\omega/c$, while the contribution from TM waves is more important for $\beta \gg \sqrt{|\varepsilon_1|}\,\omega/c \gg \omega/c$. Subsequently, for metals, heat transfer due to TM waves becomes dominant only at very short distances.

Using the relation, $\mathrm{Im}\left(\dfrac{\varepsilon-1}{\varepsilon+1}\right)=\dfrac{2\varepsilon''}{|\varepsilon+1|^2}$, and assuming identical permittivity for both media, the spectral heat flux from 1 to 2 in the limit $d \to 0$ is given by (Basu and Zhang, 2009)

$$q''_{\omega,1-2} \approx \frac{4\Theta(\omega,T_1)}{\pi^2 d^2}\int_{\xi_0}^{\infty}\frac{\varepsilon''^2 \mathrm{e}^{-2\xi}\xi \mathrm{d}\xi}{\left|(\varepsilon+1)^2-(\varepsilon-1)^2\,\mathrm{e}^{-2\xi}\right|^2} \tag{2.11}$$

where $\xi=\beta d$, $\xi_0 = d\omega/c$, and ε'' is the imaginary part of the dielectric function. As seen from Eq. (2.11) the heat flux will be proportional to d^{-2} in the proximity limit.

2.2 Dielectric Function

For thermal radiation, the polarization **P** is linearly related to the electric field given by (Griffiths, 1999),

$$\mathbf{P}(\mathbf{x},\omega)=\varepsilon_0\chi_{\mathrm{e}}(\mathbf{x},\omega)\mathbf{E}(\mathbf{x},\omega) \tag{2.12}$$

where $\chi_{\mathrm{e}}(\mathbf{x},\omega)$ is the electric susceptibility of the medium and ε_0 is the permittivity of vacuum. The value of $\chi_{\mathrm{e}}(\mathbf{x},\omega)$ depends on the microscopic structure of the medium. The electric displacement vector **D** can be expressed as

$$\mathbf{D}(\mathbf{x},\omega)=\varepsilon(\omega)\mathbf{E}(\mathbf{x},\omega) \tag{2.13}$$

In Eq. (2.13), the dielectric function or relative permittivity $\varepsilon(\omega)$ of the medium is given by $\varepsilon(\omega)=\varepsilon_0(1+\chi_e(\omega))$. Due to the assumption of a local form of the dielectric function, the spatial dependence term drops out from the expressions of susceptibility and relative permittivity. The real and imaginary parts of the dielectric function are intrinsically related based on the Kramers-Kronig dispersion relation, which is a consequence of the causality and is very useful in determining the frequency-dependent dielectric functions of real materials (Zhang, 2007).

2.2.1 Drude Model

The Drude model describes the frequency-dependent conductivity of metals and can also be extended to semiconductors. In a good conductor, electrons in the outermost orbits are "free" to move in accordance with the external electric field. The dielectric function of a conductor can be modeled by considering the electron movement under the electric field and is related to the conductivity by (Zhang, 2007)

$$\varepsilon(\omega)=\left(n+\mathrm{i}\kappa\right)^2=\varepsilon_\infty-\frac{\sigma_0/\tau}{\varepsilon_0\left(\omega^2+\mathrm{i}\omega/\tau\right)} \tag{2.14}$$

where ε_∞ accounts for high-frequency contributions, τ is the relaxation time (inverse of scattering rate), σ_0 is the dc conductivity, and n and κ are the refractive index and extinction coefficient respectively. Based on Eq. (2.14), the real and imaginary parts of the dielectric function can be expressed as $\varepsilon'=n^2-\kappa^2$ and $\varepsilon''=2n\kappa$, respectively. The plasma frequency is defined as $\omega_\mathrm{p}=\sqrt{\sigma_0/\tau\varepsilon_0}$ and is in the ultraviolet region for most metals. When $\omega<\omega_\mathrm{p}$, $n<\kappa$ and ε' becomes negative. At very low frequencies, the real part of the dielectric function is much smaller than the imaginary part and, therefore,

$n \approx \kappa$. Generally speaking, metals become highly reflective in the visible and infrared regions. Drude model for doped Si will be discussed in Chapter 3.

2.2.2 Lorentz Model

Unlike metals, the electrons in a dielectric are bound to molecules and cannot move freely. In contrast to free electrons, bound charges experience a restoring force in addition to the damping force. While the restoring force is given by the spring constant, the scattering rate is a measure of the damping force. The response of a single-charge oscillator to a time-harmonic electric field can be extended to a collection of oscillators. Assuming *N* types of oscillators in a dielectric, the dielectric function can be given by the Lorentz model (Zhang, 2007),

$$\varepsilon(\omega) = \varepsilon_\infty + \sum_j^N \frac{\omega_{\mathrm{p},j}^2}{\omega_j^2 - \omega^2 - \mathrm{i}\omega/\tau_j} \tag{2.15}$$

where $\omega_{\mathrm{p},j}$, ω_j, τ_j may be viewed as the plasma frequency, resonance frequency and the relaxation time of the j^{th} oscillator, respectively. Since the parameters for the Lorentz model are more difficult to be modeled as compared to those for the Drude model, they are considered as adjustable parameters that are determined from fitting. It can be seen from Eq. (2.15) that for frequencies far greater or lower than the resonance frequency, the extinction coefficient becomes negligible and the dielectrics are completely transparent. Absorption is appreciable only with an interval ($1/\tau_j$) around the resonance frequency. Therefore, dielectrics become highly reflective near the resonance frequency, and radiation inside them is rapidly attenuated or dissipated. The spectral region with a large imaginary part of the dielectric function is also called the region of resonance absorption.

2.3 Density of States

The spectral energy density in the vacuum space between the two semi-infinite surfaces is given by (Joulain *et al.*, 2005; Zhang, 2007)

$$\left\langle u\left(\mathbf{x},\omega\right)\right\rangle = \int_0^\infty \frac{\varepsilon_0}{4}\left\langle \mathbf{E}\left(\mathbf{x},\omega\right)\bullet\mathbf{E}^*\left(\mathbf{x},\omega'\right)\right\rangle + \frac{\mu_0}{4}\left\langle \mathbf{H}\left(\mathbf{x},\omega\right)\bullet\mathbf{H}^*\left(\mathbf{x},\omega'\right)\right\rangle \mathrm{d}\omega' \qquad (2.16)$$

The spectral energy density can be looked upon as the electromagnetic energy per unit volume per unit angular frequency. It is the product of the local density of states (LDOS), $D\left(z,\omega\right)$, and the mean energy of the Planck oscillator, i.e.,

$$\left\langle u\left(z,\omega\right)\right\rangle = D\left(z,\omega\right)\Theta\left(\omega,T\right) \qquad (2.17)$$

The LDOS is the number of modes per unit frequency interval per unit volume. It is a fundamental quantity and can provide a qualitative understanding of the enhanced near-field radiation. In Eq. (2.17), the LDOS is expressed as a function of z only due to the continuous translation symmetry of the system in the radial direction. Several studies have discussed the LDOS for a free-emitting surface, i.e., without medium 2 (Joulain *et al.*, 2005; Fu and Zhang, 2006). Basu *et al*. (2009b) developed an expression for LDOS in the vacuum gap by considering multiple reflections from the receiver. Neglecting the emission from the receiver, the LDOS can be expressed as the sum of electric and magnetic density of states; thus,

$$D\left(z,\omega\right) = D_{\mathrm{E}}\left(z,\omega\right) + D_{\mathrm{M}}\left(z,\omega\right) \qquad (2.18)$$

It can be shown that

$$D_{\mathrm{E}}\left(z,\omega\right) = \frac{\omega\,\mathrm{Im}(\varepsilon_1)}{16\pi^2 c^2}\int_0^\infty \left[\left(\left|\gamma_0 t_1^{\mathrm{p}}\right|^2 + \left|\beta t_2^{\mathrm{p}}\right|^2\right)\frac{\beta^2+\gamma_1\gamma_1^*}{k_1 k_1^*} + \left|k_0 t_2^{\mathrm{s}}\right|^2\right]\frac{\beta}{\left|\gamma_1\right|^2\,\mathrm{Im}(\gamma_1)}\mathrm{d}\beta \qquad (2.19)$$

and $$D_{\mathrm{M}}(z,\omega)=\frac{\omega\,\mathrm{Im}(\varepsilon_1)}{16\pi^2c^2}\int_0^{\infty}\left(\left|k_0t_2^{\mathrm{p}}\right|^2\frac{\beta^2+\gamma_1\gamma_1^*}{k_1k_1^*}+\left|\gamma_2t_1^{\mathrm{s}}\right|^2+\left|\beta t_2^{\mathrm{s}}\right|^2\right)\frac{\beta}{\left|\gamma_1\right|^2\,\mathrm{Im}(\gamma_1)}\mathrm{d}\beta \quad (2.20)$$

In the above expressions, $t_1=t_+-t_-$ and $t_2=t_++t_-$, where

$$t_+=\frac{t_{10}\mathrm{e}^{\mathrm{i}\gamma_0 z}}{1-r_{02}r_{01}\mathrm{e}^{\mathrm{i}2\gamma_0 d}} \quad (2.21)$$

and

$$t_-=\frac{t_{10}r_{02}\mathrm{e}^{\mathrm{i}2\gamma_0(d-z)}}{1-r_{02}r_{01}\mathrm{e}^{\mathrm{i}2\gamma_0 d}} \quad (2.22)$$

where $t_{10}=1+r_{10}$ is the Fresnel transmission coefficient for a given polarization (Zhang, 2007; Born and Wolf, 1999). Note that subscripts + and – represent the forward and backward waves (due to multiple reflections from both surfaces), respectively, in the vacuum gap. As seen from Eqs. (2.19) and (2.20), the density of states is a function of the material properties of the emitter and the receiver which are temperature dependant. As a result, LDOS is an implicit function of temperature.

Figure 2.2 shows the LDOS calculated at different heights over a semi-infinite SiC medium. The dielectric function of SiC is calculated using the Lorentz model (Zhang, 2007). From Fig. 2.2, notice that the LDOS increases as the distance to the emitter decreases. The increase in LDOS is due to additional modes provided by the evanescent waves which are confined close to the surface and cannot be seen in the far field. An increase in the number of modes enhances the heat transfer since it provides more channels of energy transfer (Pendry, 1999). Also around $\omega = 1.79 \times 10^{14}$ rad/s there is a near monochromatic increase in the LDOS. This is due to resonance caused by the excitation of surface waves and will be discussed in details later. The resonance frequency will be denoted by ω_{m} throughout this dissertation. When $z \to 0$,

$$D_{\text{evan}}(z,\omega) \approx \frac{1}{4\pi^2 \omega z^3} \frac{\text{Im}(\varepsilon)}{|\varepsilon+1|^2} \tag{2.23}$$

The LDOS increases by three orders of magnitude around ω_m as the vacuum gap is reduced by one order due to the z^{-3} dependence of LDOS as seen from Eq. (2.23).

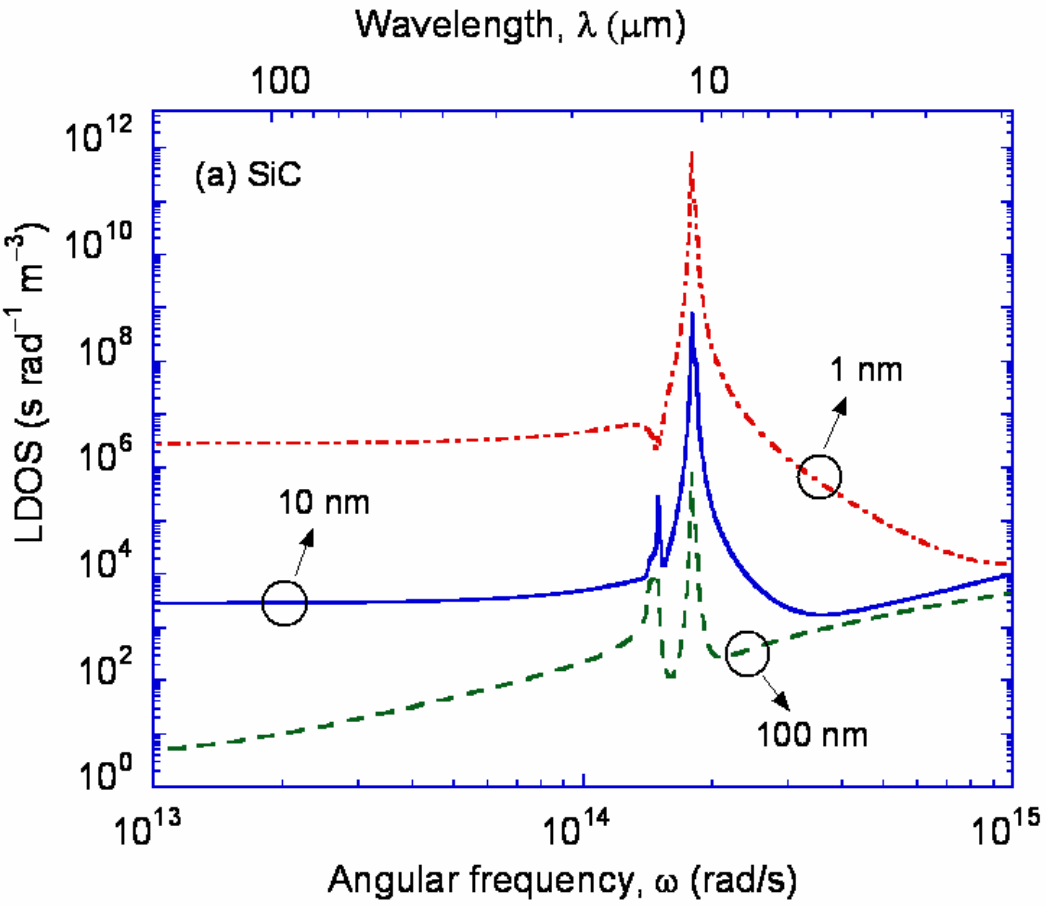

Figure 2.2 Local density of states for SiC plates.

2.4 Surface Waves

Surface waves are electromagnetic waves that propagate along the interface between two different media without radiation and their amplitude decays away from the interface (Zhang, 2007). The excitation of surface waves is a resonance phenomenon and is due to the coupling of electromagnetic waves with electrons (conductors) and phonons (polar materials). The requirement of evanescent waves on both sides of the interface prevents the coupling of propagating waves in air to the surface waves. For TM waves, the permittivity of the two media should have opposite signs for excitation of surface waves. However, for TE waves, magnetic materials are needed with negative permeability in order to excite surface waves (Zhang, 2007). All the materials considered in this research have permeability = 1. Hence, surface wave effects are considered only for TM waves. The near-field heat transfer between two media can be enhanced by several orders if surface waves are excited at the interface of both the emitter and the receiver and vacuum gap.

Due to the coupling of surface polaritons at the two interfaces, there exist two branches of dispersion curves for the *p* polarization as follows:

Symmetric mode: $$\frac{\gamma_0}{\varepsilon_0}+\coth\left(-\frac{\mathrm{i}\gamma_0 d}{2}\right)\frac{\gamma_1}{\varepsilon_1}=0 \tag{2.24a}$$

Asymmetric mode: $$\frac{\gamma_0}{\varepsilon_0}+\tanh\left(-\frac{\mathrm{i}\gamma_0 d}{2}\right)\frac{\gamma_1}{\varepsilon_1}=0 \tag{2.24b}$$

The lower-frequency branch corresponds to the symmetric mode, and the higher-frequency branch represents the asymmetric mode (Park *et al*., 2005). As will be seen later, the dispersion curve becomes almost flat at ω_{m} implying that surface polaritons can be excited over a large range of β values resulting in large near-field enhancement.

CHAPTER 3

INFRARED RADIATIVE PROPERTIES OF HEAVILY DOPED SILICON AT ROOM TEMPERATURE

This chapter describes an experimental investigation on the infrared radiative properties of heavily doped Si at room temperature. Initially accurate carrier mobility and ionization models are identified before incorporating them in the Drude model for predicting the radiative properties of heavily doped Si at room temperature. The calculated radiative properties are then validated with experiments in the infrared.

3.1 Dielectric Function of Doped Si

For heavily doped Si at room temperature, ionized donors or acceptors produce free carriers which can greatly enhance the absorption in the infrared region. The Drude model, originally developed to describe the frequency-dependent conductivity of metals, has been employed to model the free-carrier absorption of doped Si in many studies (Hesketh *et al*., 1988; Marquier *et al*., 2004). For doped silicon in the infrared region $\left(\lambda > 2\,\mu\text{m}\right)$, the Drude model gives the dielectric function or relative permittivity as follows,

$$\varepsilon(\omega)=\varepsilon_{\text{bl}}-\frac{\omega_{\text{p}}^2}{\omega\left(\omega+i/\tau\right)} \tag{3.1}$$

where ω is the angular frequency, ε_{bl} is ≈ 11.7 for heavily doped Si in the infrared (Marquier *et al*., 2004). The plasma frequency and relaxation time can be expressed as $\omega_{\text{p}}=\sqrt{Ne^2/m^*\varepsilon_0}$ and $\tau=m^*\mu/e$ respectively, where ε_0 is the permittivity of free

space, e is the electron charge, N is the carrier concentration, m^* is the carrier effective mass, and μ is the mobility (Ashcroft and Mermin, 1976). Notice that for heavily doped Si at room temperature, the scattering process is dominated by impurity scattering. Hence, lattice or phonon scattering is neglected. The effective mass in general depends on the carrier concentration and frequency. In the case of heavily doped silicon, the effective mass is independent of carrier concentration unless it exceeds $5\times10^{20}\,\mathrm{cm}^{-3}$ (Howarth and Gilbert, 1963; Riffe, 2002). The effective mass of electron or hole is taken as $0.27\,m_0$ or $0.37\,m_0$, respectively, where m_0 is the free electron mass in vacuum (Zhang, 2007). The effective mass is assumed to be independent of frequency. In order to obtain the optical constants of heavily doped silicon, it is very important to accurately model the mobility and carrier concentration at a given doping concentration. Hence, to begin with different mobility and ionization models are examined. Hereafter, phosphorus and boron implanted Si is referred to as *n*-type and *p*-type Si, respectively.

Caughey and Thomas (1967) proposed an empirical model for carrier mobility for Si in the doping range from 10^{15} to $10^{21}\,\mathrm{cm}^{-3}$ by fitting the measured resistivity of Si with both *p*-type and *n*-type dopants. Using a different fitting procedure for the same expression, Baccarani and Ostoja (1975) obtained different coefficients for *n*-type Si. On the other hand, Wagner (1972) and Antoniadis *et al*. (1978) obtained different coefficients for *p*-type Si. Masetti *et al*. (1983) improved the above-mentioned mobility models in order to fit the experimental data more accurately at higher carrier concentrations. The mobility expression for *n*- and *p*-type Si are given as

$$\mu = \mu_1 + \frac{\mu_{\max} - \mu_1}{1 + (N_e / C_r)^{\alpha}} - \frac{\mu_2}{1 + (C_s / N_e)^{\beta}} \tag{3.2}$$

and

$$\mu = \mu_1 \exp(-p_c / N_h) + \frac{\mu_{\max}}{1 + (N_h / C_r)^{\alpha}} - \frac{\mu_2}{1 + (C_s / N_h)^{\beta}} \tag{3.3}$$

Values of different symbols in Eqs. (3.2) and (3.3) can be obtained from Masetti *et al*. (1983).

A comparison of the different mobility models with experimentally measured values is shown in Figs. 3.1(a) and (b) for *p*- and *n*-type Si, respectively. The solid lines refer to the models while the symbols refer to the experimental data. It can be clearly seen that while the mobility models used by Caughey and Thomas (1967), Baccarani and Ostoja (1975), Wagner (1972), and Antoniadis *et al*. (1978) predict a constant value beyond carrier concentration of 5×10^{19} cm^{-3}, the model suggested by Masetti *et al*. (1983) can accurately fit the experimental data at higher carrier concentrations. While the first two terms in the Eqs. (3.2) and (3.3) exhibit a trend similar to the mobility expressions used by previous researchers, the third term accounts for the decreasing mobility at higher doping concentrations. Since this term is negligible for carrier concentrations lower than 5×10^{19} cm^{-3}, the different mobility models exhibit a similar trend at lower carrier concentrations. Hence, the mobility model proposed by Masetti *et al*. (1983) is adopted in the present study for calculation of the carrier mobility.

Marquier *et al*. (2004) assumed complete impurity ionization over the entire doping concentration range in their calculation of the radiative properties of doped Si. Similar assumptions have also been made in some previous studies by different researchers (Caughey and Thomas, 1967; Sze and Irvin, 1968). Fu and Zhang (2006) on

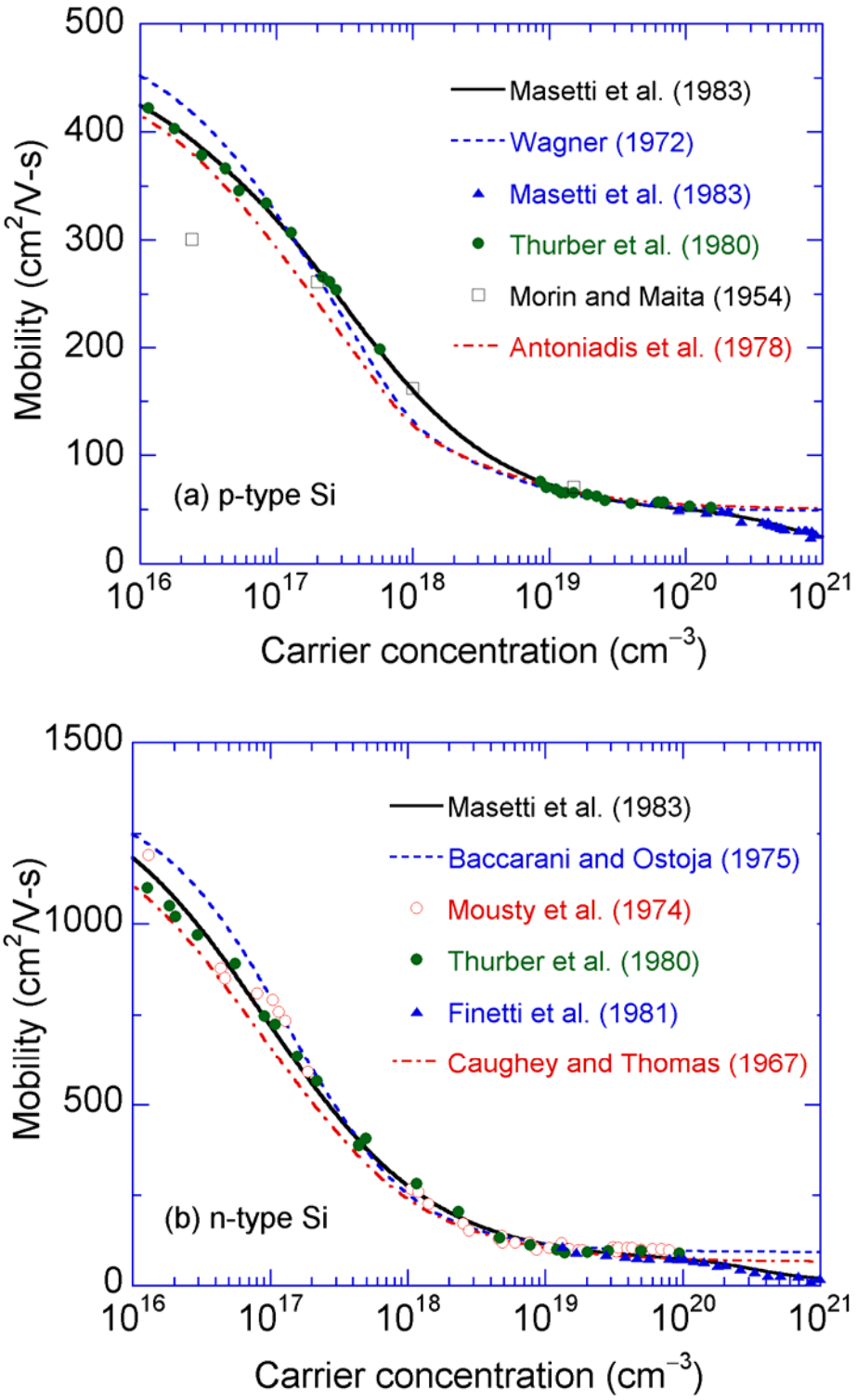

Figure 3.1 Comparison of different mobility models for (a) *p*-type and (b) *n*-type Si at room temperature with experimental data.

the other hand considered complete ionization for doping concentrations below 10^{17} cm^{-3}, and partial ionization beyond 10^{17} cm^{-3}. They had adopted the ionization model proposed by Gaylord and Linxwiler (1976) in their analysis. Recently, Park *et al*. (2007) reported a doping density model which was accurate to 8% of the measured values for doping concentration lower than 10^{18} cm^{-3} within the temperature range of 50-300 K. However, for concentrations greater than 10^{19} cm^{-3}, the model generated considerable error. Previous experimental results on doped Si have indicated that only in the doping range from about 10^{17} to 10^{19} cm^{-3}, the dopant atoms are not completely ionized and the majority carrier concentration can be lower than the doping concentration. Between 10^{16} and 10^{18} cm^{-3}, the Fermi level is located close to the doping level; this results in the dopant states being occupied and leads to incomplete ionization (Kuzmicz, 1986). However, beyond 10^{18} cm^{-3} the donor energy band gets broadened and merges with the conduction band; this generates more free carriers and increases the degree of ionization as the doping level further increases. As a result of the two competing effects, the degree of ionization is the lowest around 10^{18} cm^{-3}. Kuzmicz (1986) included this effect of partial ionization while considering a wide range of doping concentrations for both *p*- and *n*-type Si and developed an empirical model. Figures 3.2 (a) and (b) compare the different ionization models for *p*- and *n*-type Si, respectively. The degree of ionization has been presented as insets in the two figures. For the model proposed by Kuzmicz (1986), the degree of ionization first reduces to 0.75 for *p*-type Si and 0.9 for *n*-type Si around 10^{18} cm^{-3}, and then increases to almost unity at doping concentrations greater than 10^{19} cm^{-3}, suggesting partial ionization in the doping range from 10^{17} and 10^{19} cm^{-3},

for both *p*- and *n*-type Si. On the other hand, the model predicted by Gaylord and Linxwiler (1976) suggests incomplete ionization for both *p*- and *n*-type Si over the entire doping range and the carrier concentration is only 5% of the doping concentration at doping levels exceeding $10^{21}\,\mathrm{cm}^{-3}$. For complete ionization model, the degree of ionization is always 1. Using the different ionization models, the carrier concentrations can be obtained which, when multiplied by mobility expressions in Eqs. (3.2) and (3.3) will yield resistivity.

The dc resistivity is a function of the carrier concentration and mobility given as $\rho = (Ne\mu)^{-1}$. Figures 3.3 (a) and (b) compare the measured resistivity values, taken from previous studies with those calculated from different ionization models. The solid lines represent the resistivity predicted with the carrier concentration obtained from Kuzmicz (1986) and mobility from Eqs. (3.2) and (3.3), for *p*- and *n*-type Si, respectively. For comparison, the resistivity for *p*-type Si calculated using the ionization model from Gaylord and Linxwiler (1976) is shown as the dash-dotted line and the resistivity calculated by assuming complete ionization is shown as the dashed line in Fig. 3.3(a). Clearly, the model proposed by Gaylord and Linxwiler (1976) results in an overprediction of the resistivity beyond $10^{18}\,\mathrm{cm}^{-3}$. On the other hand, the full ionization model yields an underprediction of the resistivity in the doping range between 10^{17} and $10^{19}\,\mathrm{cm}^{-3}$. The resistivity obtained from the ionization model of Kuzmicz (1986) agrees very well with the experimental measurements over a wide range of doping concentrations and, hence, is adopted in this study. Beyond $10^{20}\,\mathrm{cm}^{-3}$, the data from Beadle *et al*. (1985) do not match well with the prediction for *p*-type Si as can be seen in

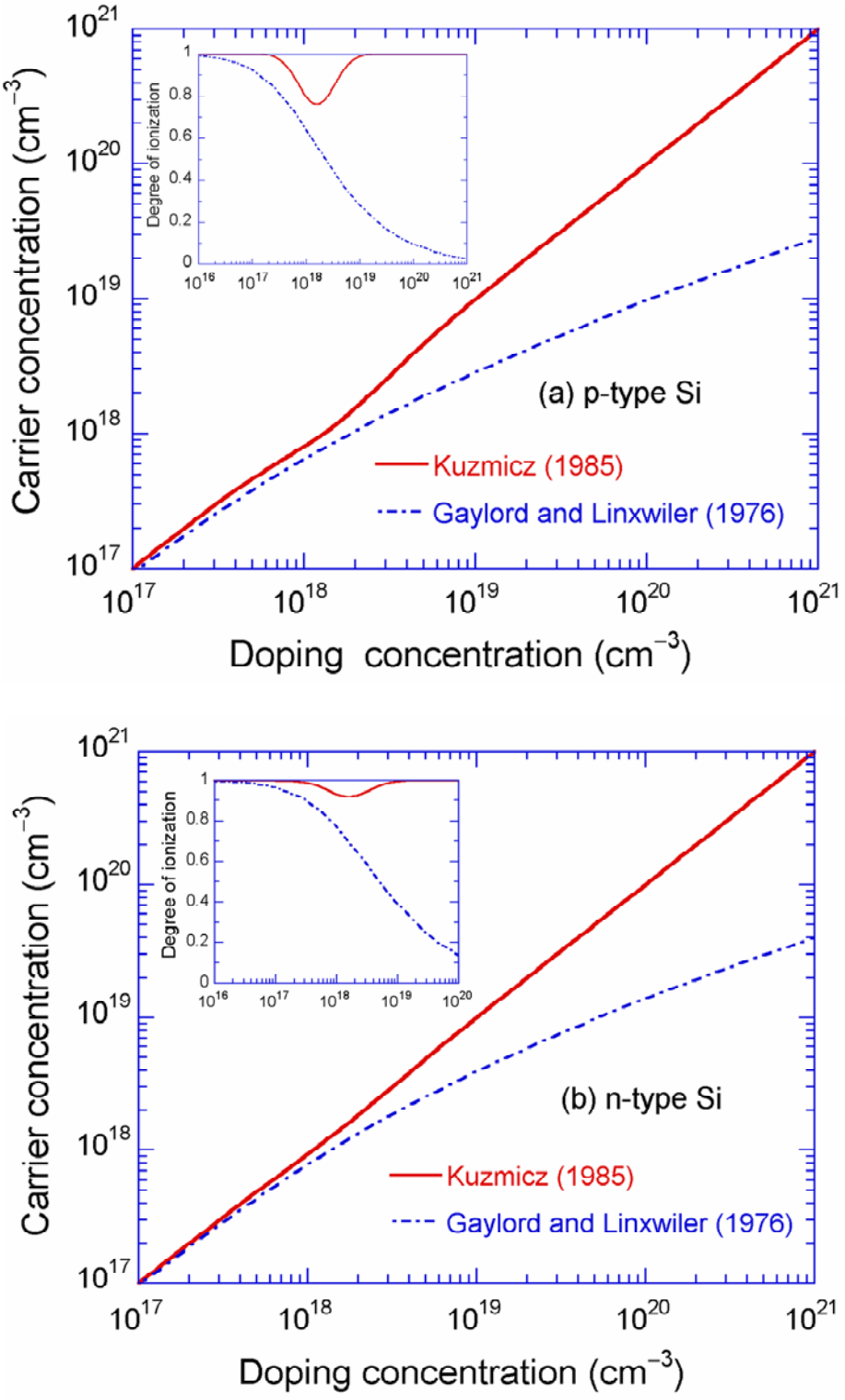

Figure 3.2 Carrier concentrations versus doping level calculated from two models for (a) *p*-type and (b) *n*-type Si at room temperature. The insets show the degree of ionization.

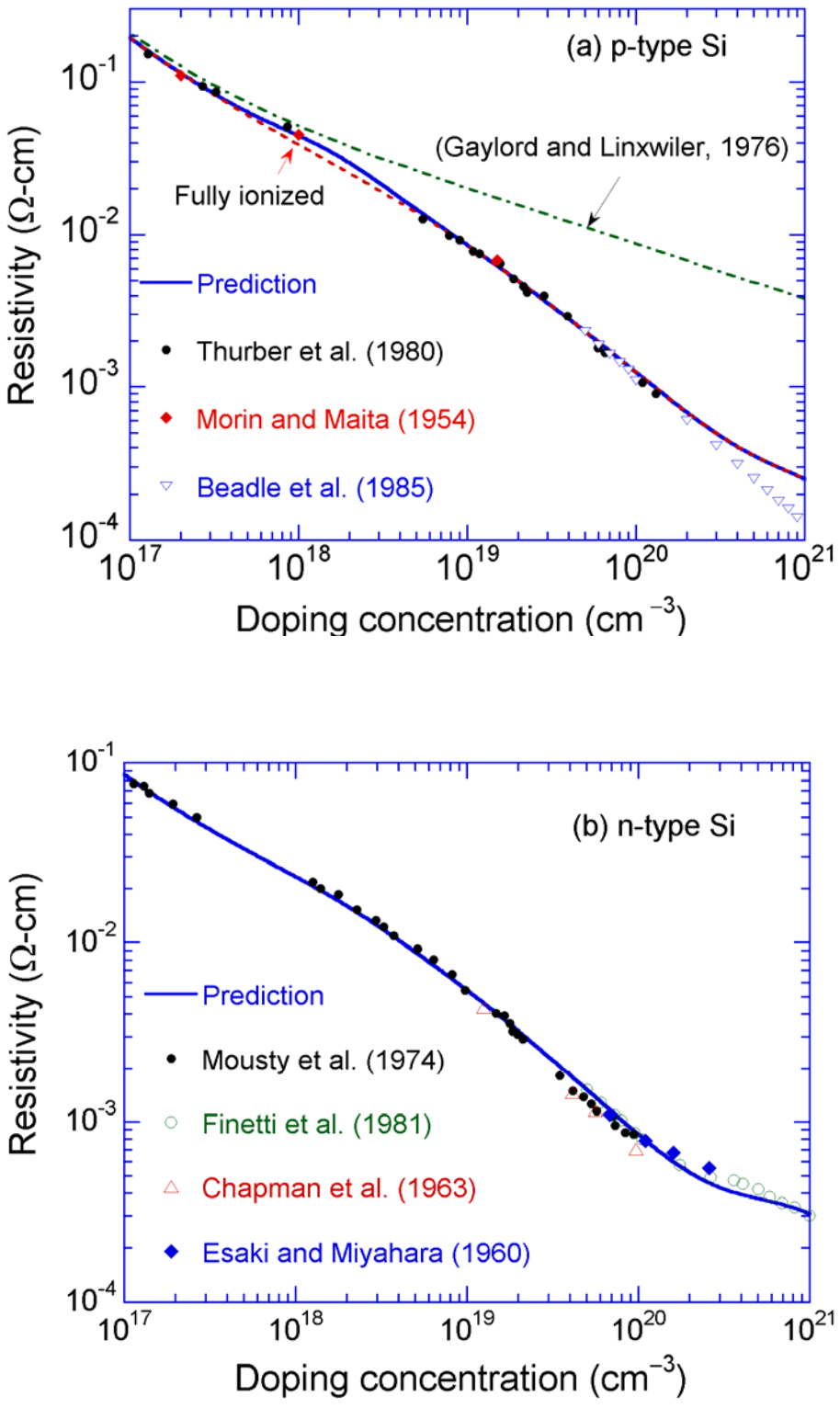

Figure 3.3 Comparison of calculated resistivity with measurements from different studies for (a) *p*-type and (b) *n*-type Si, for different doping levels at room temperature.

Fig. 3.3(a). At doping concentrations greater than $10^{20}\,\mathrm{cm}^{-3}$, the carrier mobility and degree of ionization depend on the doping and annealing methods.

3.2 Sample Preparation and Characterization

In this study, lightly doped ($10^{15}\,\mathrm{cm}^{-3}$) Si wafers (400 μm thick) were ion-implanted by a commercial vendor, using 70 keV boron and 160 keV phosphorus atoms with dosage of $6.4\times10^{14}\,\mathrm{cm}^{-2}$ and $6.4\times10^{15}\,\mathrm{cm}^{-2}$,respectively. These dosages correspond to as-implanted peak doping concentrations of $10^{20}\ \mathrm{cm}^{-3}$ and $10^{21}\ \mathrm{cm}^{-3}$, respectively. To activate the implanted ions, subsequent annealing is required at appropriate combinations of time and temperature (May and Sze, 2004).

Rapid thermal annealing was selected in order to prevent substantial dopant diffusion into the sample. Before annealing, the doped Si wafers were diced into $25\times25\,\mathrm{mm}^2$ samples and a 500-nm thick silicon dioxide layer was deposited on the wafers using low-pressure chemical vapor deposition at 300°C, in order to prevent out-diffusion of boron and phosphorus ions during annealing. Different temperatures were selected for studying the influence of temperature on activation of the implanted ions. The *p*-type wafers were annealed at 850, 950, and 1100°C for 60 s, while the *n*-type wafers were annealed at 850, 950, and 1050°C for 60 s in vacuum. The ramp time required to attain the annealing temperature was set to 10 s, consistent with the furnace specifications. The wafers were allowed to cool below 100°C before being taken out of the annealing chamber. The temperature of the wafers was constantly monitored using thermocouples. After annealing, the deposited oxide layer was etched away using dilute hydrofluoric acid.

Transmittance and reflectance for the doped Si samples were measured by a commercial FTIR spectrometer, equipped with a globar source and a pyroelectric detector (Lee *et al*., 2005). The spectra were measured at room temperature with a spectral resolution of 4 cm^{-1} in the spectral range from 500 to 5000 cm^{-1}. For the transmittance measurements, the sample holder with an aperture of 6-mm diameter limits the beam diameter on the sample. The spectrometer and sample compartment were purged with N_2 gas for about 30 min to reduce the absorption by water vapor and CO_2 molecules in air. An average over 64 scans was used. The uncertainty was estimated to be 0.01 with 95% confidence level (Lee *et al*., 2005). Reflectance was measured at an incidence angle of 10° using a specular reflectance accessory with an Au mirror as the reference. The reflectance of Au mirror was calculated using the tabulated optical constants (Palik, 1985). The sample holder has a hole which is smaller than the beam diameter. As a result, part of the beam is reflected back from the sample holder for measurements of both the sample and the reference. The reflectance from the backside of the holder was measured by removing the samples and is always less than 0.02. The overall uncertainty for reflectance measurements was estimated to be 0.02 with 95% confidence level, taking into account the different error sources.

Figure 3.4 compares transmittance of both *p*- and *n*-type Si wafers when annealed to different temperatures. Without annealing, both the *p*- and *n*-type as-implanted samples behave like lightly doped Si as seen from the transmittance measurements. For the $10^{20} cm^{-3}$ *p*-type Si, it is observed that the samples attain full dopant activation at 950°C since there is no further change in the transmittance when annealed to 1100°C. However, for the $10^{21} cm^{-3}$ *p*-type Si, higher temperature is required to activate majority

of the dopants as seen in Fig. 3.4(a). The dashed line with symbols in Fig. 3.4(b) shows the calculated transmittance of the lightly doped Si substrate used in this study, to be discussed later. Based on the transmittance measurements, the four fully activated samples were selected for SIMS analysis. Table 1 tabulates the as-implanted and post-annealing peak doping concentration of the fully activated samples, along with the corresponding annealing temperatures. Hereafter, these four samples will be referred by their numbers.

SIMS analysis was provided by a commercial supplier for the four selected samples. Since SIMS is a destructive test (May and Sze, 2004), one of the wafers was used for SIMS analysis while optical measurements were performed on the other sample but from the same batch. Due to the formation of a native-oxide layer of a few nanometers on the surface of Si, the doping concentration in the skin layer close to the surface is not accurate as is seen from the SIMS profile and this layer was subtracted from the total film thickness during modeling. Figure 3.5 shows the doping profiles obtained from SIMS measurements.

Table 1 Samples for SIMS analysis and spectrometric measurements

Sample number	Dopant type	As-implanted peak doping concentration (cm^{-3})	Annealing temperature (°C)	Peak doping concentration after annealing (cm^{-3})
1	Phosphorus	1.0×10^{20}	950	3.1×10^{19}
2	Boron	1.0×10^{20}	1100	3.8×10^{19}
3	Phosphorus	1.0×10^{21}	950	2.8×10^{20}
4	Boron	1.0×10^{21}	1100	1.5×10^{20}

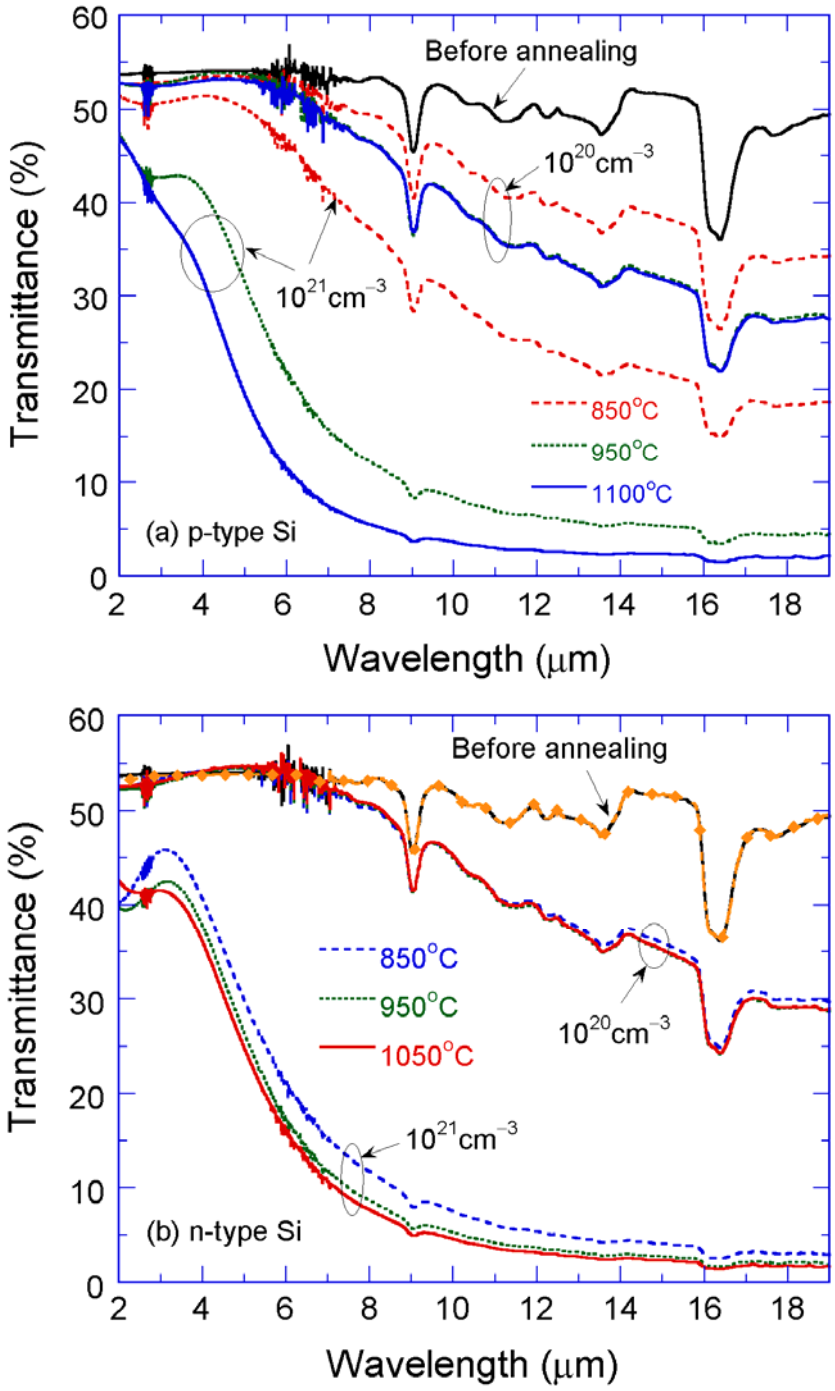

Figure 3.4 Measured transmittance of (a) *p*-type and (b) *n*-type Si annealed at different temperatures. The dashed line with symbols in (b) refers to the transmittance calculated based on the refractive index of Si obtained from Palik (1985) and the extinction coefficient extracted from the measured transmittance at 4 cm^{-1} resolution. The doping concentration refers to the peak concentration before annealing of the samples.

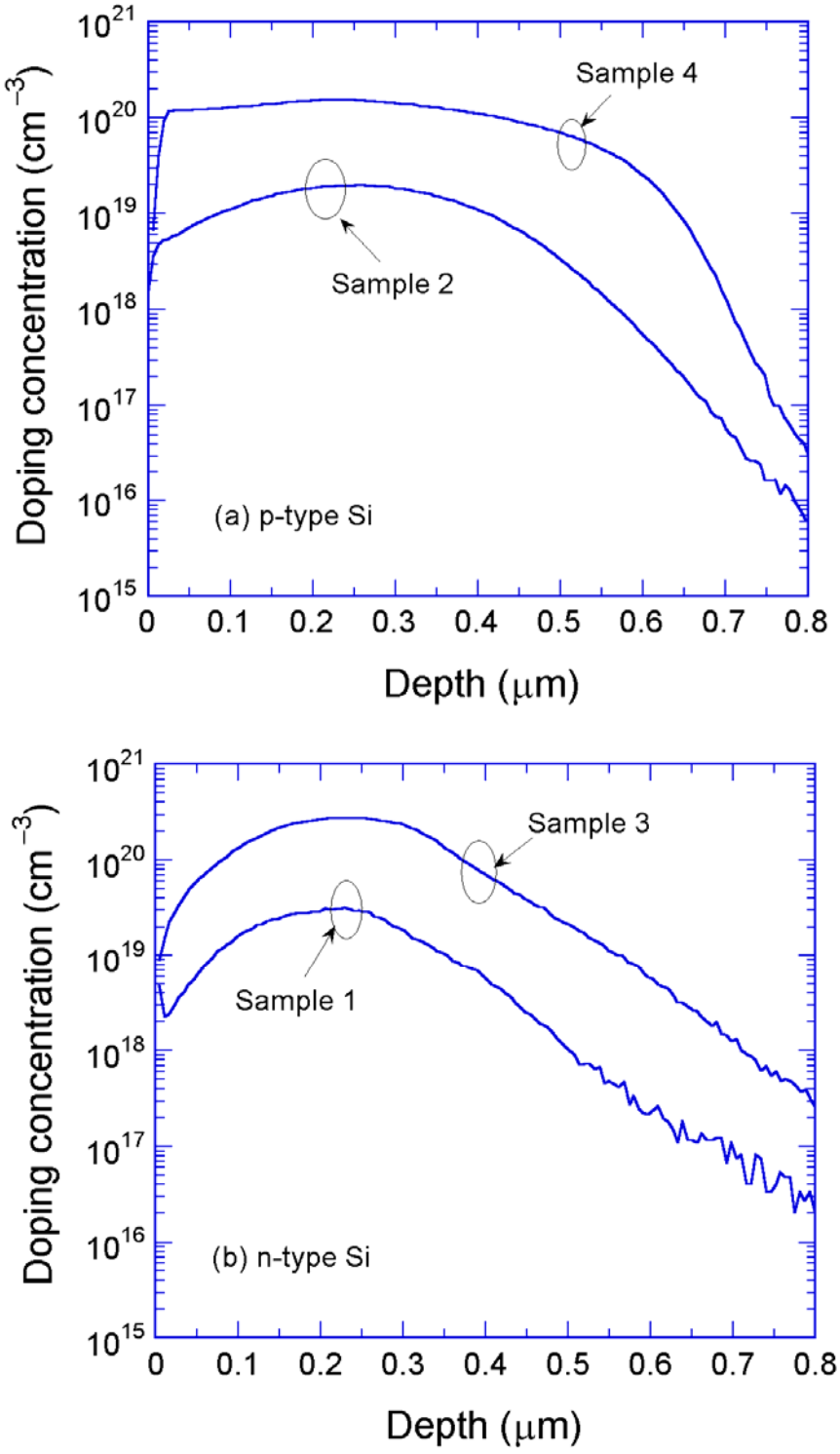

Figure 3.5 Comparison of the doping profiles obtained from SIMS for (a) *p*-type Si (Samples 2 and 4) and (b) *n*-type Si (Samples 1 and 3).

3.3 Measurement Results and Comparison with Modeling

The doped Si samples can be treated as a multilayer structure of thin films of varying doping concentrations on a thick Si substrate. For the Si substrate, the refractive index was obtained from the tabulated data in Palik (1985). The extinction coefficient for the Si substrate was extracted from the measured transmittance at 4 cm^{-1} resolution. The tabulated values of the extinction coefficient from Palik (1985) cannot account for the absorption due to the interstitial oxygen at around 9 μm (Zhang, *et al*., 1996) and the lattice absorption around 16 μm for the lightly doped Si substrate used in the present study. The doping profile down to a doping concentration of $1\times10^{17}\,cm^{-3}$, obtained from SIMS measurements was approximated by a step function and broken into 10 nm thin films. The film thickness was also reduced to 5 nm and the difference in modeling results was observed to be less than 0.03%. The carrier concentrations were obtained from the doping concentrations using the ionization model of Kuzmicz (1986), and consequently the optical constants could be calculated for each layer using the Drude model, discussed earlier. For the structure of thin films on a thick substrate, radiation inside the film can be treated as coherent and that in the substrate as incoherent. The transmittance and reflectance for the radiation incident on the substrate as well as the film were calculated using thin film optics (Zhang, 2007).

Figure 3.6 shows the measured transmittance and reflectance compared with theoretical modeling results for samples 1 to 4. The transmittance and reflectance is calculated using the doping profiles obtained from SIMS measurements. In the calculation, the doped Si region is considered up to the doping level of $10^{17}\,cm^{-3}$ with a total of 65 layers, each 10 nm thick. For Sample 1, the calculated results based on the

Drude model agree very well with the experimental measurements for both transmittance and reflectance. The reflectance for radiation incident on both the film and the substrate is close to that of the lightly doped Si substrate up to 8 μm. Beyond 8 μm, however, the reflectance for radiation incident on the substrate changes little while the reflectance from the film increases with wavelength. For a doping concentration of 2×10^{19} cm^{-3}, the penetration depth increases with wavelength and, at 8 μm, the penetration depth is about 15 μm, which is much greater than the thickness of the doping region. As the wavelength further increases, the penetration depth continues to decrease while the refractive index of the doping region decreases with wavelength. Both effects contribute to the reduction in the reflectance for incidence on the film. Note that the decreased refractive index of the film results in an antireflection effect. Generally speaking, the transmittance and reflectance for Samples 1 and 2 follow the same trends due to the similar optical constants as a result of the similar doping concentrations. For Sample 2, however, the measured transmittance is lower than that predicted. The difference significantly exceeds the uncertainty of FTIR measurements. While the model may have some limitations, this discrepancy may also be caused by the nonuniformity in the dopant distribution during the ion bombardment as well as the annealing process.

For Samples 3 and 4, the heavily doped region causes significant absorption, especially at longer wavelength and results in a reduction in the transmittance. The measured and predicted radiative properties agree fairly well, except for the transmittance at shorter wavelengths. The reflectance is much higher for incidence on the film due to the metallic behavior of the heavily doped silicon. The location of the reflectance minima matches with that in the refractive index for the average doping concentration. Sample 3

has a slightly higher peak doping concentration, and the reflectance minimum is shifted to a slightly shorter wavelength than that for Sample 4. Note that the minimum value of the reflectance at around 4 μm for incidence on the film is less than that for incidence on the substrate. This implies that the absorptance is greater for incidence on the film. At longer wavelengths, however, the reflectance for incidence on the substrate is smaller, indicating a higher absorptance than incidence on the film. While the transmittance for Samples 1 and 2 shows dips at 9 and 16 μm due to lattice vibration, these dips are essentially not observable for Samples 3 and 4 due to the screening effect of the film. In fact, the reflectance for incidence on the film does not show dips at all, because the penetration depth is much less than the thickness of the doping layer. Due to multiple reflections, the absorption at 9 and 16 μm is greatly enhanced for incidence on the substrate, as can be seen by the magnitude of the dips in the reflectance. This can be understood as an optical cavity effect.

To sum up, we have measured the transmittance and reflectance of heavily doped Si up to a doping concentration of 10^{21} cm^{-3} in the wavelength region from 2 to 20 μm. Drude model was employed for modeling the dielectric function of doped Si based on the selected carrier mobility and ionization models. The doped Si samples were modeled as multilayer structure of heavily doped Si thin films deposited on a thick lightly doped Si substrate. The calculated results are in good agreement with transmittance and reflectance measurements, suggesting that the Drude model developed in this study is appropriate in predicting the radiative properties of heavily doped Si near room temperature. This model will be used in the next chapter to calculate near-field heat transfer.

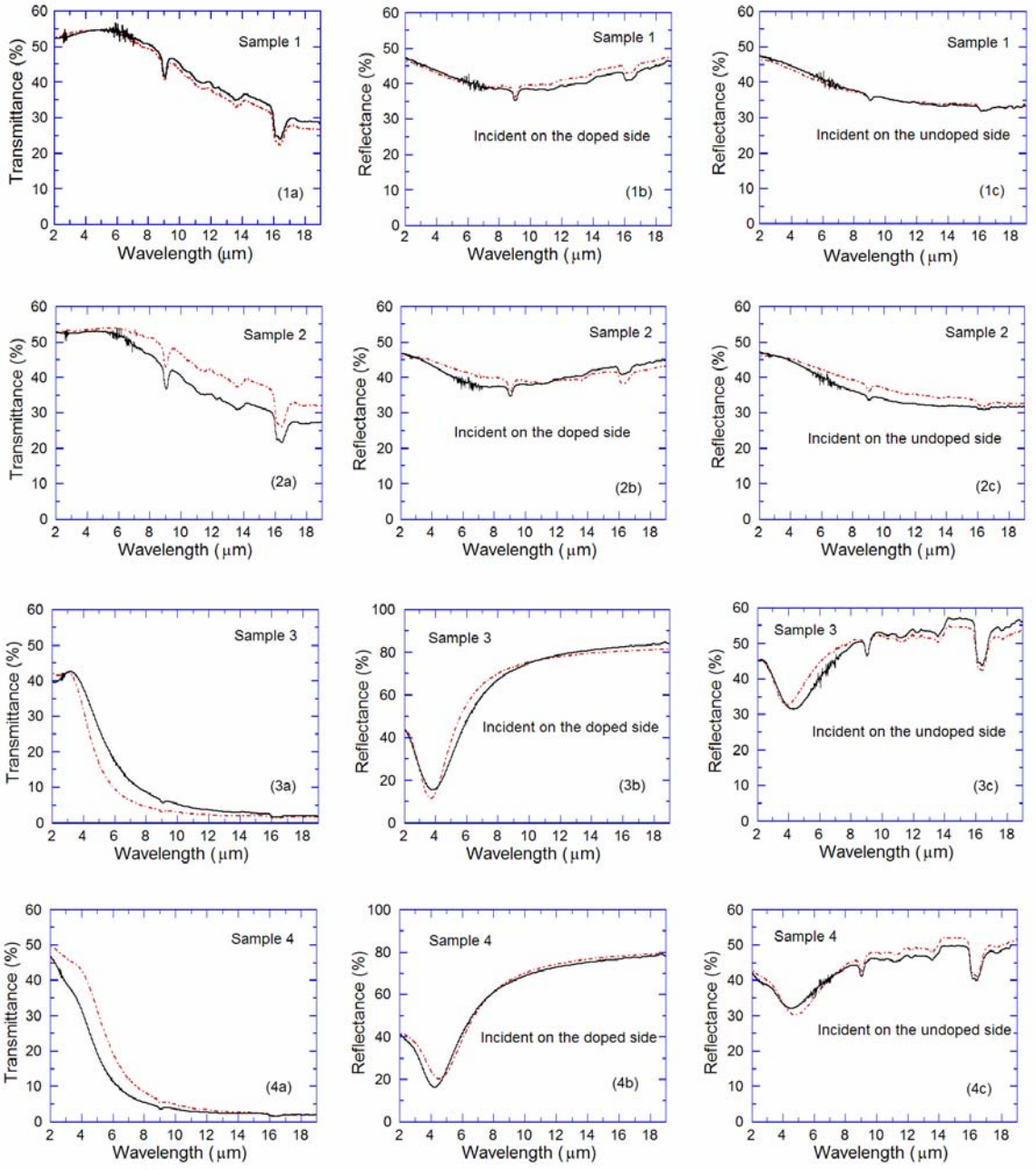

Figure 3.6 Comparison of measured (solid lines) and calculated (dash-dotted lines) transmittance and reflectance (for incidence from either side) of all four samples.

CHAPTER 4

NEAR-FIELD THERMAL RADIATION IN HEAVILY DOPED SILICON

Doped Si has been extensively used in microelectronics and optoelectronics industries. As seen from the previous chapter, the optical properties of doped Si can be tuned by changing the doping concentration. Hence, the study of near-field radiation between doped Si is of great significance. Marquier *et al*. (2004) studied near-field radiative transfer between doped-silicon plates near room temperature using a simplified Drude model, without considering the effect of doping level. Fu and Zhang (2006) calculated the radiative energy transfer between two plates of doped silicon at different temperatures for various doping levels and vacuum gap widths. However, the employed ionization and mobility models may not be appropriate for heavily doped silicon near room temperature, which in turn, may cause inaccuracies in the prediction of energy transfer.

This chapter describes a theoretical investigation of near-field radiative heat transfer between doped silicon surfaces separated by a vacuum gap using the improved dielectric function model for heavily doped silicon discussed in the previous chapter. The effects of surface waves, doping level, polarization, and vacuum-gap width on the spectral and total radiative transfer are studied based on the fluctuational electrodynamics. The local density of states near the emitter is also calculated with and without the receiver. Surface roughness and tilting effects are not considered. The emitter

is maintained at 400 K, while the receiver is maintained at 300 K. Only *n*-doped Si is considered in this study, since the results for *p*-doped Si would be similar.

Before looking into near-field radiation in doped Si, the dielectric function of *n*-type Si at 400 K is plotted in Fig. 4.1. The dielectric function is calculated using the improved Drude model discussed in the previous chapter. With increase in the doping level, the real part of dielectric function ε' decreases, while the imaginary part ε'' increases, due to increased free carrier concentration. An order of magnitude increase in the doping concentration of Si results in a tenfold increase in ε''. A negative ε' with simultaneously very large ε'' results in metallic behavior of heavily doped silicon. The dielectric function adopted by Fu and Zhang (2006) fails to capture the metallic behavior of Si at doping levels greater than 10^{20} cm^{-3} due to lesser number of free carriers. On the other hand, the simple model used by Marquier *et al*. (2004) cannot accurately predict the dielectric function for Si in the doping range from 10^{17}–10^{19} cm^{-3} since it assumes that all the dopant atoms in Si are fully ionized irrespective of doping level.

4.1 Effect of Surface Waves

As can be seen from Eq. (2.7), the net energy transfer involves integration over both ω and β. The function $s(\omega,\beta)/2\pi$ is illustrated in Fig. 4.2 as a contour plot for 10^{20} cm^{-3} doped Si plates separated by a 10 nm vacuum gap. It should be noted that Fig. 4.1 is for TM waves since the contribution for TE waves is negligible for doping levels between 10^{18} and 10^{20} cm^{-3}. The color bar on the right shows the scale for $s(\omega,\beta)/2\pi$ with the brightest color representing the peak value at $\omega_{\mathrm{m}} = 2.67\times10^{14}\,\mathrm{rad/s}$, corresponding to $\lambda_{\mathrm{m}} \approx 7\,\mu\mathrm{m}$, and $\beta_{\mathrm{m}} = 62\omega/c$. Most of the energy transfer will occur around this peak and

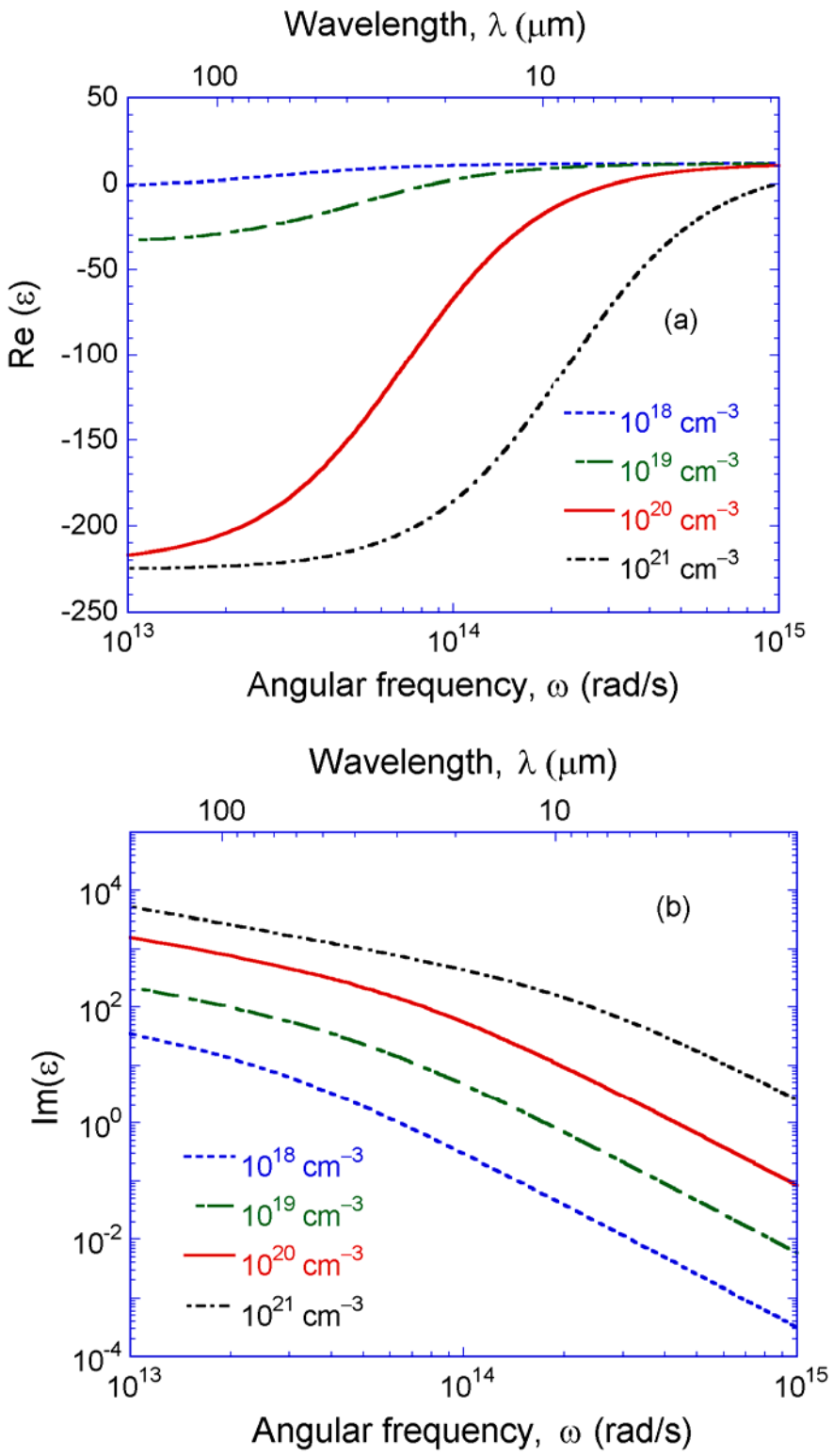

Figure 4.1 Predicted dielectric function of *n*-type silicon for different doping concentrations at 400 K: (a) real part; (b) imaginary part.

there will be negligible energy transfer at $\beta > 400\omega/c$ for a given ω and at $\omega > 4\times10^{14}$ rad/s for any β. Note that the contribution of propagating waves ($\beta < \omega/c$) is also negligible. The resonance energy transfer in the near field is a result of surface plasmon polaritons (SPPs), which can greatly enhance the radiative transfer. Following the work of Lee and Zhang (2008), the dispersion relation is calculated between doped Si plates and plotted as dashed curves in Fig. 4.2. Notice that at SPP resonance, a large number of models or channels of heat transfer can be excited which increases the total energy transfer. The dispersion curves match well with the peak in $s(\omega,\beta)$.

The vacuum gap width d has a significant effect on near-field heat transfer. This can be understood by plotting $s(\omega,\beta)$ at ω_m as a function of β for different d values, as shown in Fig. 4.3 where β is normalized with respect to ω_m/c. Note that ω_m changes little for $d < 100$ nm. As the gap width decreases, the peak of $s(\omega,\beta)$ increases and shifts toward larger β values. The area underneath is proportional to the spectral energy flux, and the volume under the curved surface of $s(\omega,\beta)$ in Fig. 4.3 is proportional to total energy flux that tends to be inversely proportional to d^2 as noted in previous studies (Fu and Zhang, 2006; Joulain *et al*., 2005). An alternative view would be to consider the ratio s/β, which was called transfer function according to Fu and Zhang (2006). As d decreases, the peak value of $s(\omega,\beta)/\beta$ remains nearly unchanged, but its location will shift towards larger β values. As a consequence, there will be a significant increase in the number of modes for energy transfer, because the integration of s/β over $2\pi\beta d\beta$, i.e., the area in the x-y plane of wavevector-space, is directly proportional to the energy transfer. The transfer function can thus be viewed as the contribution per unit area in the parallel plane of the wavevector.

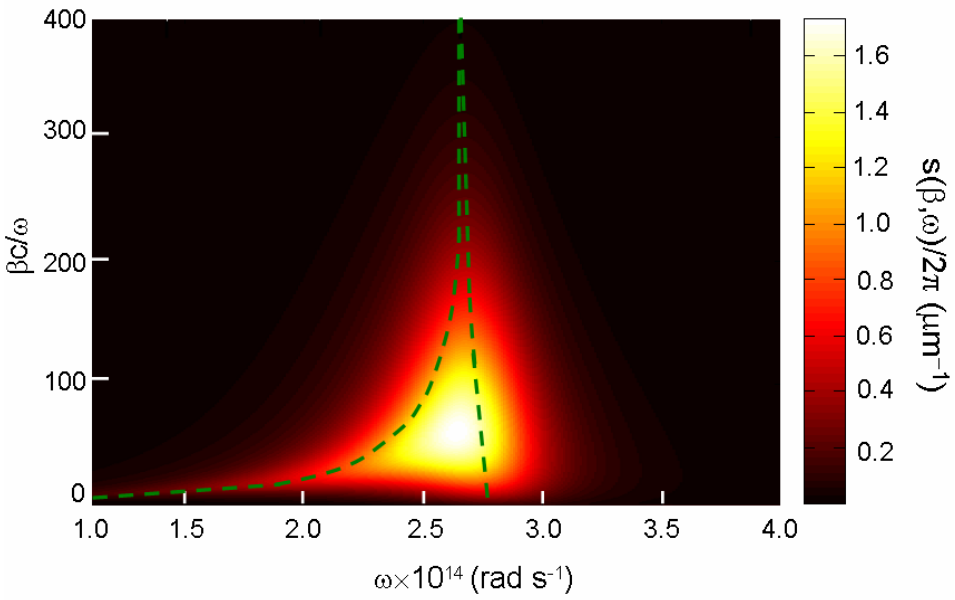

Figure 4.2 Contour plot of $s(\omega,\beta)$ for doping concentration of 10^{20} cm^{-3} in both the emitter (at 400 K) and receiver (at 300 K), when the vacuum gap width d = 10 nm. Note that the angular frequency is shown in the range from 10^{14} to 4 × 10^{14} rad/s, and the parallel wavevector component is normalized to the frequency. The dashed curves represent the two branches of the surface-polariton dispersion.

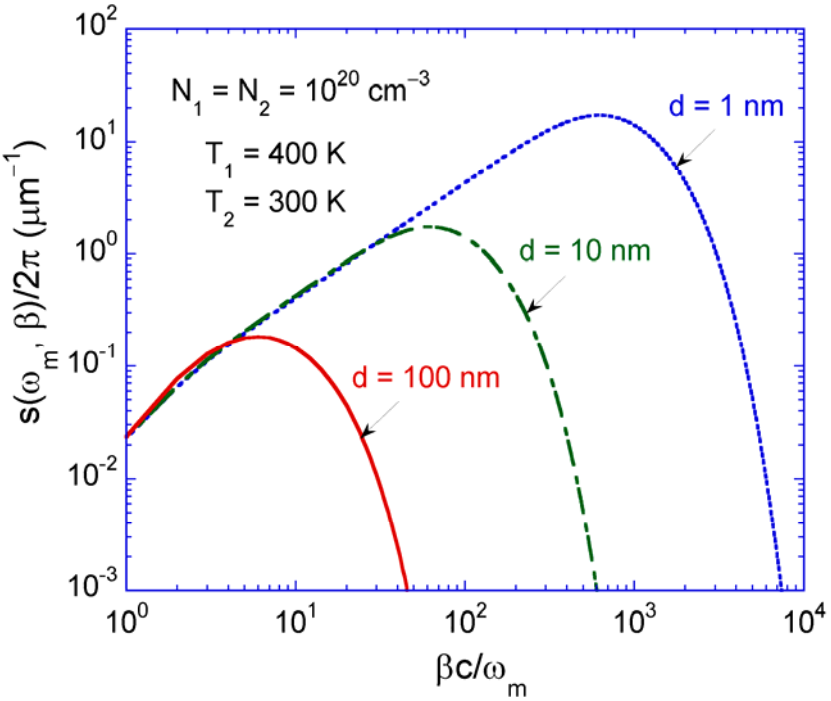

Figure 4.3 Graph of $s(\omega_m,\beta)$ as a function of β for different vacuum gap widths.

4.2 Effect of Doping Level

When different doping levels are considered, the location of the peak in $s(\omega,\beta)$ shifts towards higher frequencies with increased doping level. For example, $\omega_{\mathrm{m}} = 2.67\times10^{13}$, 8.5×10^{13}, and 2.67×10^{14} rad/s for doping concentrations of 10^{18}, 10^{19}, and 10^{20} cm^{-3}, respectively. The integration of $s(\omega,\beta)$ over β gives a weighted function to modify the Planck blackbody distribution function. The spectral energy transfer per unit area q''_{ω} can be obtained as

$$q''_{\omega} = \frac{1}{\pi^2}\left[\Theta(\omega,T_1)-\Theta(\omega,T_2)\right]\int_0^{\infty} s(\omega,\beta)\,\mathrm{d}\beta \tag{4.1}$$

so that $q''_{net} = \int_0^{\infty} q''_{\omega}\,\mathrm{d}\omega$. This function is plotted against ω for different doping concentrations in Fig. 4.4 for T_1 = 400 K and T_2 = 300 K. It can be seen from Fig. 4.4(a) that, for d = 100 nm, a strong spectral peak occurs near the SPP resonance frequency for each doping level. The peaks for doped silicon, however, are much broader than that for SiC and for metals because of the large losses. In addition to the peaks caused by SPPs, there exists a broadband spectral distribution due to thermal fluctuation as described by the Planck's oscillator model. As discussed by Francoeur and Menguc (2008), Wien's displacement law no longer holds for near-field radiative transfer. There may be two or more peaks in the spectral radiative flux. When the vacuum gap width is reduced to 10 nm, the spectral energy flux is increased by two orders of magnitude around the SPP resonance frequencies, as shown in Fig. 4.4(b). In the regions far away from resonance frequencies, the spectral energy flux does not increase further as the d decreases. This is why some traces (away from the peaks) in Fig. 4.4(a) do not show up in Fig. 4.4(b). It is

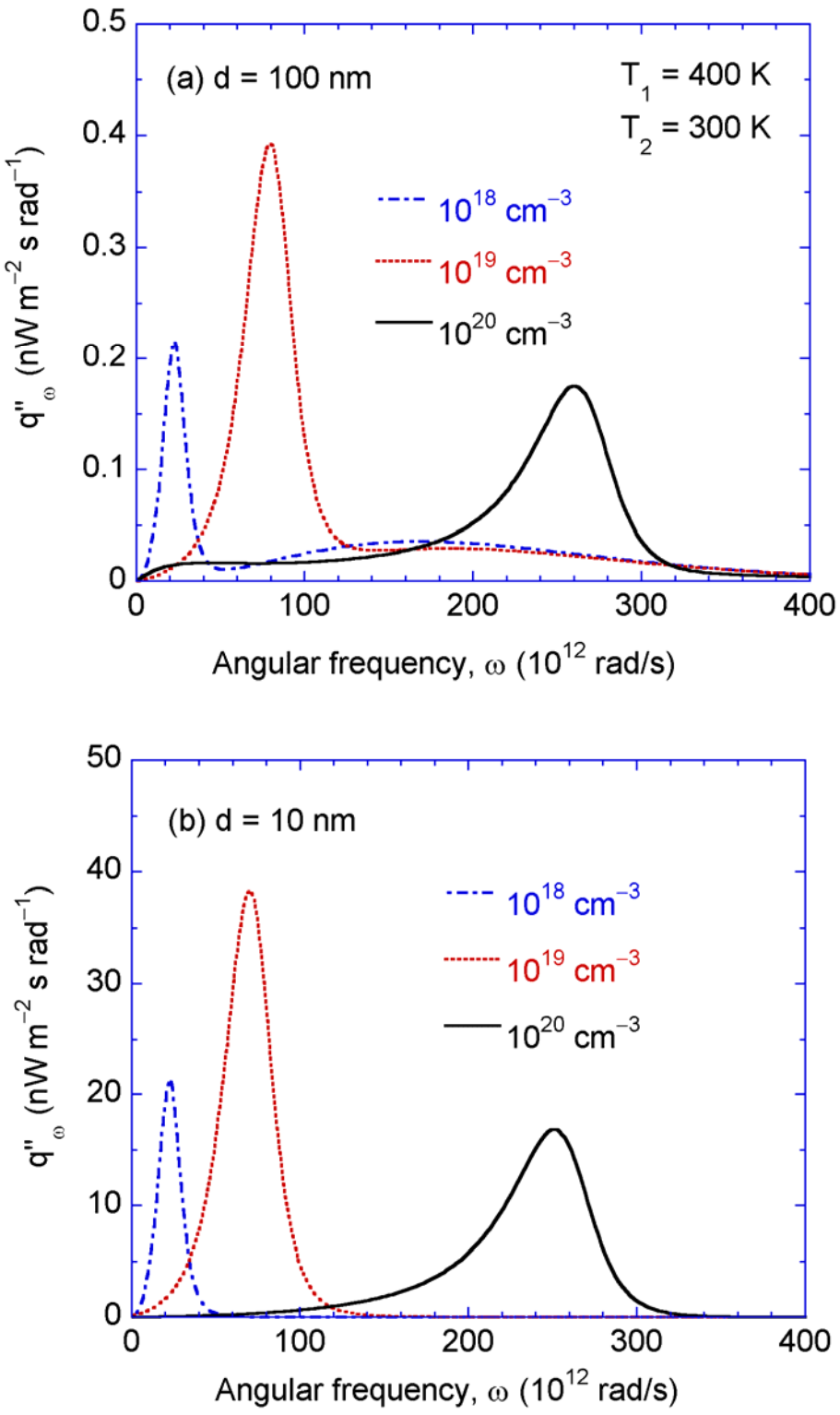

Figure 4.4 Spectral energy flux for different doping levels at (a) d = 100 nm, and (b) d = 10 nm.

the area under these curves that determines the total energy transfer. The predicted radiative heat transfer between two doped Si plates is plotted in Fig. 4.5 as a function of the vacuum gap width. Both plates are maintained at the same doping level, which is varied from 10^{18} to 10^{21} cm^{-3}. The dotted line with circles is the radiation heat flux between two blackbodies given by $\sigma\left(T_1^4 - T_2^4\right)$. At d = 1 nm, the net heat flux between 10^{19} or 10^{20} cm^{-3} doped Si plates can exceed five orders of magnitude that between two blackbodies because of photon tunneling and surface waves. It is interesting to note that, while the energy flux spectra are different between doping concentration of 10^{19} or 10^{20} cm^{-3}, the total energy is about the same when d < 30 nm. As can be seen from Fig. 4.4, the peak is sharper and narrower for doping concentration of 10^{19} cm^{-3} than that for 10^{20} cm^{-3}. This explains why the nanoscale radiation between doped Si plates can be enhanced to the same order of magnitude as that between SiC plates; the latter case has an extremely high peak in a very narrow spectral band (Mulet *et al*., 2002; Lee and Zhang, 2008). It should be noted that near room temperature, increase in the doping level of Si does not always enhance the energy transfer. In fact, the radiative heat transfer is smallest for 10^{21} cm^{-3} doped Si plates as compared with other doping levels as shown in Fig. 4.5. The main reason for this is that at the doping concentration of 10^{21} cm^{-3}, ω_m is too high and due to the exponential term in the denominator of the mean energy of Planck's oscillator, the spectral energy flux is not significantly enhanced as compared with other doping levels. Another way to view it is that at smaller d, the spectral heat flux is proportional to product of $\mathrm{Im}\left[\left(\varepsilon_1 - 1\right)/\left(\varepsilon_1 + 1\right)\right]$ and $\mathrm{Im}\left[\left(\varepsilon_2 - 1\right)/\left(\varepsilon_2 + 1\right)\right]$(Joulain *et al*., 2005). Hence, very large values of ε'', as for 10^{21} cm^{-3} doped Si, will significantly

reduce the energy transfer. This is also the case for good metals in the infrared region such as Al and Cu. At $d > 200$ nm, doping concentrations between 10^{18} or 10^{19} cm^{-3} yield the largest radiative heat transfer. Note that surface wave coupling becomes weaker as d increases to beyond 100 nm. The above calculations assumed that the doping concentrations are the same for both media.

Figure 4.6 illustrates the effect of doping concentration on nanoscale radiation when the vacuum gap width is fixed at $d = 1$ nm. The doping level of medium 1 is represented as N_1 while that for medium 2 is represented by N_2. Generally speaking, surface waves are better coupled when the two media have similar dielectric functions. The result is that there exist peaks when $N_1 \approx N_2$, at doping levels up to 10^{20} cm^{-3}. A decrease in the energy transfer is seen when the doping level of one or both of the silicon plates exceeds 10^{20} cm^{-3}. Generally speaking, the model used by Fu and Zhang (2006) does not correctly predict the net radiative transfer near room temperature for doping levels greater than 10^{18} cm^{-3}, because it was assumed that a large portion of the doping sites are not ionized to free carriers. It should be noted that the dielectric function model used in the present study did not consider band gap absorption and cannot be used at wavelengths shorter than 1.3 μm. Furthermore, the Drude model proposed in this study is not applicable at temperatures much higher than 400 K.

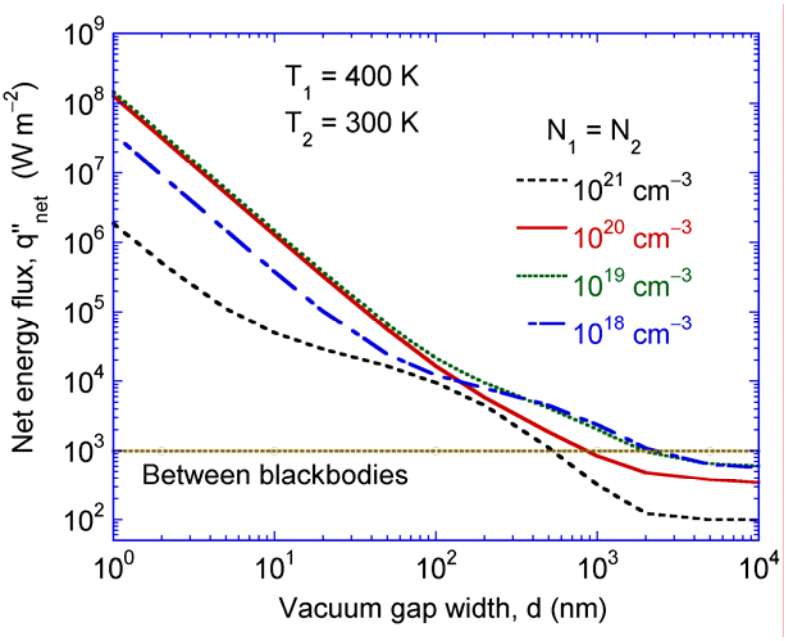

Figure 4.5 Net energy flux between medium 1 at 400 K and medium 2 at 300 K at different doping levels versus gap width. The dash-dotted line refers to the net energy transfer between two blackbodies maintained at 400 and 300 K, respectively.

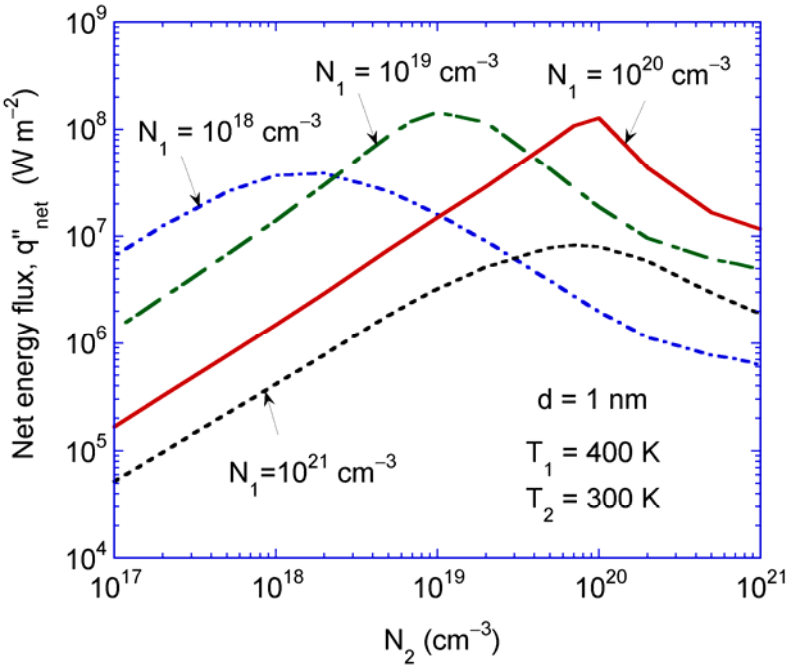

Figure 4.6 Effect of doping on the net energy transfer between two doped Si plates separated by 1 nm vacuum gap.

4.3 Effect of Polarization

So far, all the discussions are for TM waves, because the contribution by TE waves are negligible in most cases, except for doping concentration of 10^{21} cm^{-3} in the region $d > 5$ nm. As can be seen from Fig. 4.5 that the curve for the net energy transfer (calculated for both polarizations) for $N_1 = N_2 = 10^{21}$ cm^{-3} exhibits different trend as the other curves. Figure 4.7 shows the contribution of different polarization states to the net energy transfer for two doping levels. It is seen from Fig. 4.7(a) that TM wave contribution dominates the net energy transfer for 10^{20} cm^{-3} doped Si, although the TE wave contribution increases as d increases to beyond 100 nm. This is expected since surface waves are strongly coupled at the nanometer scales as discussed earlier. On the other hand, there is a significant TE wave contribution for 10^{21} cm^{-3} doped Si at vacuum gap $d > 10$ nm. The TE wave contribution does not increase when the gap is reduced further from about $d = 50$ nm or so. Most of the TE wave contributions are limited to smaller β values, because $\mathrm{Im}\left(r_{01}^{\mathrm{s}}\right)$ and $\mathrm{Im}\left(r_{02}^{\mathrm{s}}\right)$ decreases quickly as β increases and become negligible when $\beta > 5\omega/c$. When $\beta < 5\omega/c$ and d < 50 nm, the term $\exp[-2\,\mathrm{Im}(\gamma_0)d] \approx 1$ in Eq. (2.9). Hence, $s(\omega,\beta)$ becomes independent of d, resulting in the nearly constant total energy flux for the TE wave. Similar results have been seen between two metallic surfaces (Chapuis *et al*., 2008).

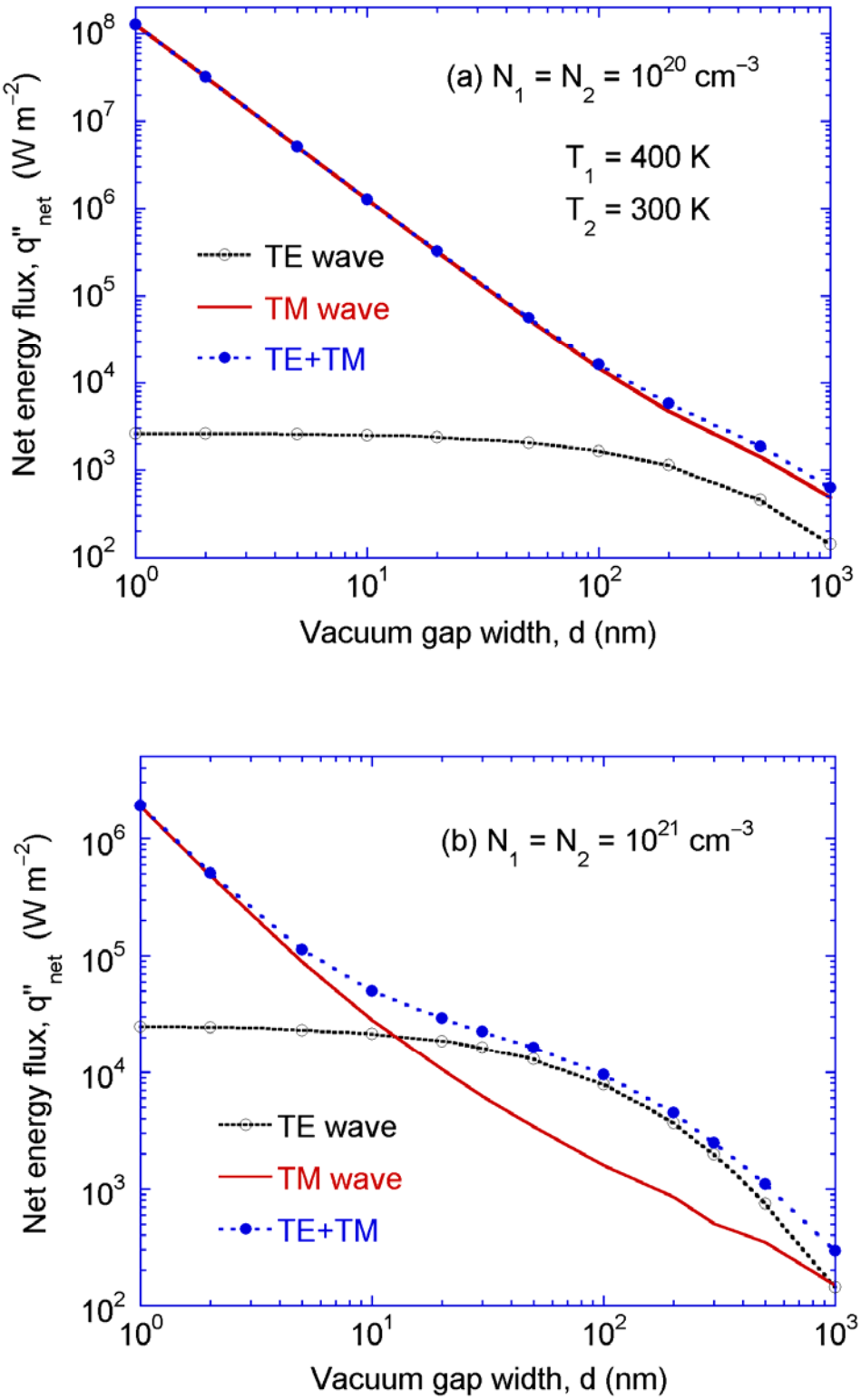

Figure 4.7 Contribution of TE and TM waves to the net energy transfer for (a) 10^{20} cm^{-3}, and (b) 10^{21} cm^{-3} doped Si at different gap widths.

4.4 Local Density of States

The local density of states is calculated when both media are doped silicon with the same doping concentration of 10^{20} cm^{-3}. Only the LDOS for TM waves is considered since the contribution of TE waves is negligibly small. The LDOS is calculated in the vacuum gap for the case when the emitter is at 400 K and the receiver is at 0 K. Emission from the receiver is not considered in this analysis. If the receiver is not at 0 K, the LDOS must be separately considered by assuming that the other medium is at 0 K. Since the electromagnetic fields from the emitter and the receiver are not correlated, the LDOS from each surface can be separately calculated, however, they cannot be added as the sum does not have any physical meaning. In terms of energy density, the local energy density will be sum of the energy densities from the emitter and the receiver and hence can be added together. Other than the temperature dependence of the dielectric function, LDOS is not a function of temperature. Figure 4.8(a) plots the spectral variation of LDOS at three different locations inside the vacuum gap when d = 10 nm. When $\omega = \omega_m$, LDOS is strongly amplified and displays a peak in the spectra. Figure 4.8(b) compares the spatial variation of LDOS in the gap with and without the receiver at $\omega = \omega_m$. It can be seen from Fig. 4.8 that the receiver has little influence on the LDOS close to the emitter, e.g., $z < 0.5d$, where LDOS is almost the same as that of free emission from medium 1 into vacuum. As $z \to 0$, LDOS diverges as z^{-3}, which has been noticed by others without the receiver. On the other hand, the presence of the receiver starts to modify the LDOS when $z > 0.5d$. At $z = d$, LDOS calculated considering the receiver is nearly twice of the LDOS without the receiver. Multiple reflections of the evanescent waves result in a strong coupling that enhances the density of states near the receiver surface.

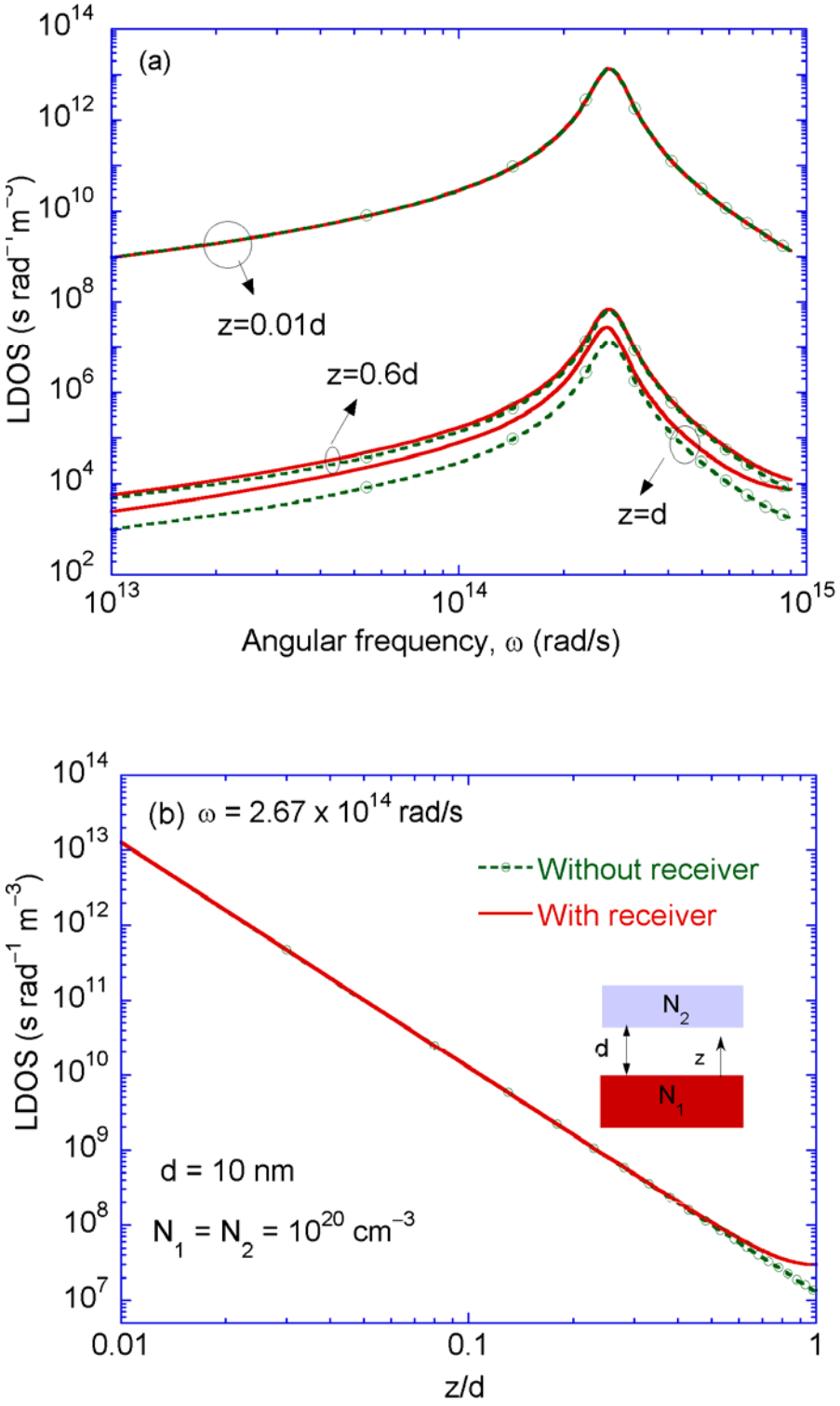

Figure 4.8 Local density of states for 10^{20} cm^{-3} doped Si plates separated by a 10 nm vacuum gap: (a) Spectral variation of LDOS at $z = 0.01d$, $z = 0.6d$, and $z = d$ (b) spatial variation of LDOS at $\omega_m = 2.67\times10^{14}$ rad/s.

In summary, a theoretical investigation is performed on the near-field radiative energy transfer between heavily doped Si (10^{18} to 10^{21} cm^{-3}) plates near room temperature, using an improved dielectric function model. The effect of surface wave is examined, and the ranges of ω and β that dominate the heat transfer are identified for different doping levels. Increasing the doping level for Si does not necessarily increase the energy transfer. The effect of the receiver on the local density of states in the vacuum gap is negligibly small except near the surface of the receiver.

CHAPTER 5

MAXIMUM ENERGY TRANSFER IN NEAR-FIELD THERMAL RADIATION AT NANOMETER DISTANCES

From the previous chapter, we see that when the vacuum gap d separating the two surfaces becomes very small, the near-field heat transfer varies as d^{-2}. This means that the heat flux will diverge as $d \rightarrow 0$ and its physical significance has been debated among researchers (Mulet *et al*., 2001; Pan, 2000). As the vacuum gap decreases, the energy transfer shifts to large values of the parallel wavevector component. The imposed cutoff limits the number of modes for photon tunneling. Chapuis *et al*. (2008a) used a nonlocal dielectric function of metals and showed that the d^{-2} dependence would disappear at $d <$ 0.1 nm and the heat flux for p polarization would asymptotically reach a constant. It should be noted that some time back the maximum near-field radiative transfer was discussed by Pendry (1999) who assessed the allowable modes or channels in near-field interactions. A relation between the real and the imaginary parts of the reflection coefficient was derived for achieving maximum heat transfer between two flat plates separated by vacuum. This relation was also used by Volokitin and Persson (2004) in calculating the maximum possible near-field energy transfer. However, the expression for maximum heat flux obtained in these studies is achievable only when $d \rightarrow 0$ and cannot be looked upon as the maximum near-field heat transfer at finite separation distances. According to Pendry (1999), the material of choice that maximizes the near-field heat flux would be a good conductor with $\varepsilon'' >> \varepsilon'$. On the contrary, it has been calculated that good conductors do not result in significant enhancement in radiative transfer at the nanometer length scales (Loomis and Maris, 1994).

This chapter investigates the maximum achievable radiative heat flux between two parallel plates separated by a vacuum gap from 0.1 to 100 nm. Starting from the general expression for near-field heat transfer between two semi-infinite media, simplified relations are derived for the energy transfer at very small vacuum gaps in terms of the cutoff wavevector. By assuming a frequency-independent dielectric function and introducing a cutoff parallel wavevector component, the ideal dielectric function for the two media which will maximize the near-field radiative transfer is identified. Subsequently, the influence of cutoff wavevector on the net energy transfer is investigated at different vacuum gaps.

Theoretical Formulation

The total heat flux between the two media is given by,

$$q''_{\text{net}} = \int_0^\infty q''_\omega(\omega)d\omega = \frac{1}{\pi^2}\int_0^\infty \left[\Theta(\omega,T_1)-\Theta(\omega,T_2)\right]X(\omega)d\omega \tag{5.1}$$

where $X(\omega)$ is a weighting function given by

$$X(\omega) = \int_0^{\beta_c} Z(\omega,\beta)\beta d\beta \tag{5.2}$$

In most studies, the upper limit in Eq. (5.2) is set to infinity. Electrons in solids move in a periodic potential characterized by the Bloch wave, with a maximum wavevector of π/d_c at the edge of the first Brillouin zone (Ashcroft and Mermin, 1976). Here, d_c is the lattice constant, which is on the order of interatomic distance. This posts a limit on the smallest surface wavelength or cutoff wavevector parallel to the surface $\beta_c = \pi / d_c$ (Volokitin and Persson, 2004). If identical dielectric function is assumed for both media in the form of $\varepsilon = \varepsilon' + i\varepsilon''$, the following approximation can be obtained for $\beta >> \omega/c$:

$$Z(\omega,\beta)=\frac{4\varepsilon''^2 e^{-2\beta d}}{\left|(\varepsilon+1)^2-(\varepsilon-1)^2 e^{-2\beta d}\right|^2} \tag{5.3}$$

which is based solely on the contribution from *p*-polarized waves. It can be shown that Eq. (5.3) has a maximum of $Z_{\max}=0.25$ when

$$\frac{(\varepsilon'-1)^2+\varepsilon''^2}{(\varepsilon'+1)^2+\varepsilon''^2}=e^{2\beta d} \tag{5.4}$$

For materials with $\varepsilon''>>\varepsilon'$ such as metals in the long wavelength, it can be seen that when $d=0$, Eq. (5.4) will be satisfied and Eq. (5.3) will approach $Z_{\max}=0.25$ for sufficiently large $\varepsilon''/\varepsilon'$. Taking $Z=Z_{\max}$, one obtains from Eq. (5.2) that $X_{\max}=\beta_c^2/8$. With $\int_0^\infty \frac{xdx}{e^x-1}=\frac{\pi^2}{6}$, it can be shown that the maximum near-field heat flux becomes

$$q''_{\max}=X_{\max}\frac{k_B^2}{6\hbar}(T_1^2-T_2^2)=\frac{k_B^2\beta_c^2}{48\hbar}(T_1^2-T_2^2) \tag{5.5}$$

which is the T^2 dependence obtained by Volokitin and Persson (2004). It should be noted that Eq. (5.5) differs by a factor of 2 from the expression of maximum heat flux in Volokitin and Persson (2004), since the contribution from *s* polarization is not included in Eq. (5.5). The expression given in Eq. (5.5) is the ultimate maximum heat flux and is only achievable when $d\to 0$. Even at $d=1$ nm, the condition given in Eq. (5.4) cannot be satisfied in a large range when β is near β_c. Subsequently, the achievable heat flux at finite separation distances is much smaller than that provided in Eq. (5.5) when $\varepsilon''/\varepsilon'>>1$. Furthermore, it has been noted that a good conductor generally does not

provide the greatest enhancement. In order to determine the maximum radiative heat flux in the near field, it is convenient to rewrite Eq. (5.2) as

$$X(\omega) = \frac{4}{d^2}\int_0^{\xi_c} \frac{\varepsilon''^2 e^{-2\xi}\xi d\xi}{\left|(\varepsilon+1)^2 - (\varepsilon-1)^2 e^{-2\xi}\right|^2} \tag{5.6}$$

Where $\xi = \beta d$ and $\xi_c = \beta_c d$. If the upper bound is set to infinity, it can be seen that $X \propto d^{-2}$, which results in divergence of the heat flux as the distance approaches zero.

Maximum Radiative Energy Transfer

A frequency-independent permittivity is used to study the limit of near-field heat flux for arbitrary materials considering finite separation distances. This will help identify the suitable combinations of real and imaginary parts of the dielectric function in order to obtain maximum energy transfer at different vacuum gaps. For simplicity, both the emitter and receiver are assumed to have the same dielectric function. The key for maximizing heat flux is to optimize X in Eq. (5.1) since it is a weighted function that modifies the spectral distribution. The approximation in Eq. (5.3), which is valid for p polarization at short distances, is used to evaluate Eq. (5.2). Figure 5.1 shows a contour plot of X with respect to ε' and ε'', for different gap thicknesses by setting d_c = 0.5 nm or $\beta_c = \pi / d_c = 2\pi$ nm^{-1}. The value of X is normalized by $\beta_c^2 / 8$ so that the maximum of $X^* = 8X / \beta_c^2$ is 1. In the plots, ε' varies from −5 to 5 while ε'' varies from 10^{-3} to 10. The color bar on the right shows the value for X^* (in logarithmic scale for d = 10 nm) with the brightest color representing the peak value. When $d \to 0$ as shown in Fig. 5.1(a),

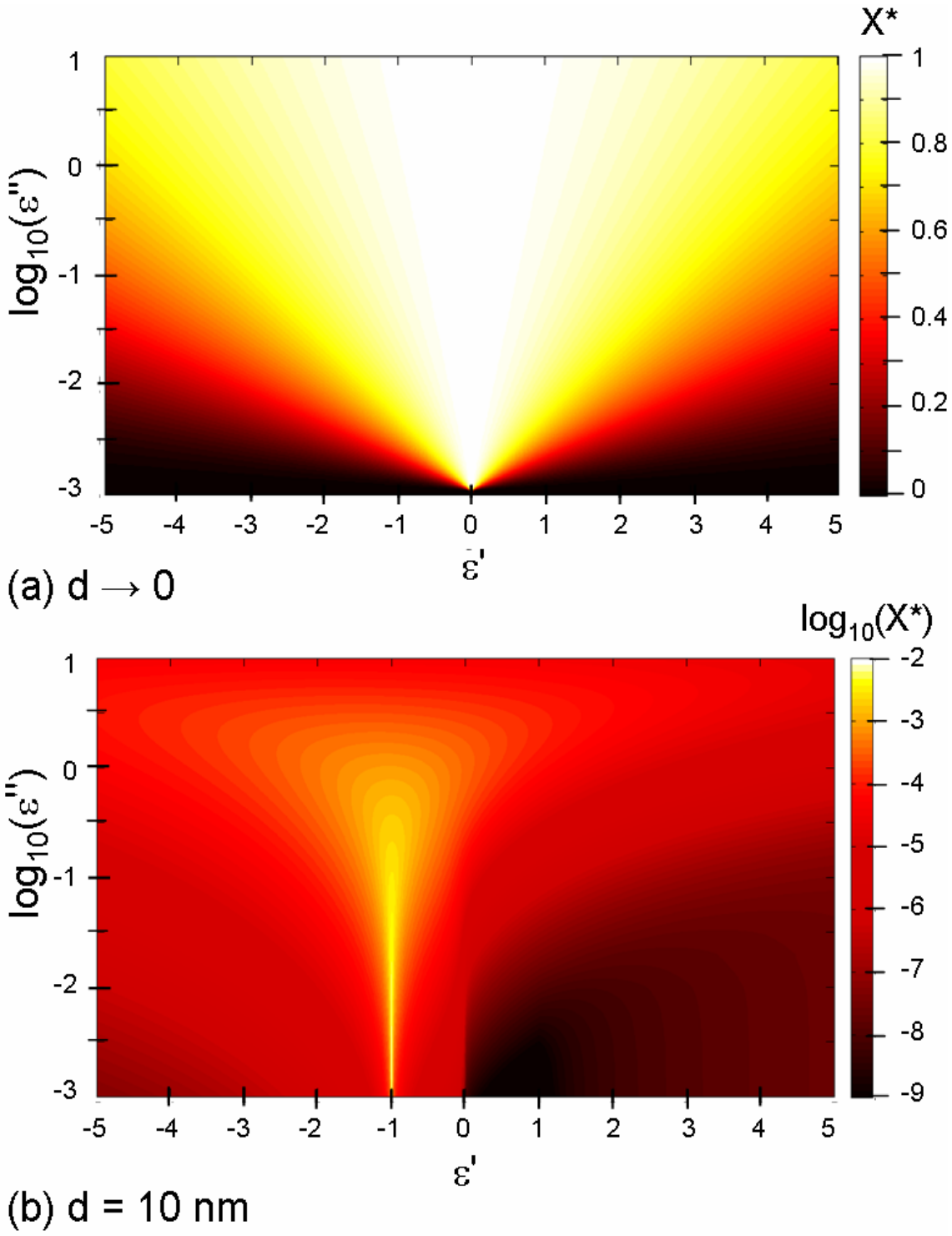

Figure 5.1 Contour plot of X^* as a function of ε' and ε'' at $d = 0$ (a) and d = 10 nm. The magnitude of X^* is denoted by the colored contours and is plotted in linear scale for $d = 0$ and in logarithmic scale for d = 10 nm.

$X^* = 1$ can be achieved in a large region when $\varepsilon'' / |\varepsilon'| >> 1$ and the plot is symmetric with respect to $\varepsilon' = 0$. At a finite distance, d = 10 nm as shown in Fig. 5.1(b), the peak of X^* is located at $\varepsilon' = -1$ as long as ε'' is not so large. Furthermore, due to the dependence of Z with respect to βd, the maximum of X^* is less than 0.01 when d = 10 nm. From Eqs. (5.3) and (5.4), $\varepsilon' = -1$ corresponds to a resonance-like condition, which has been discussed in Volokitin and Persson (2004). For $\varepsilon' > 0$ and $\varepsilon'' << \varepsilon'$, the two media behave as lossless dielectrics and contribution is negligible for large β values. In such cases, the enhancement in near-field radiation is very limited and will saturate as $d \to 0$.

In order to further explore the dependence of X upon ε', ε'', and d, Fig. 5.2 plots X^* as a function of ε' (or ε'') at different distances with fixed ε'' (or ε') for d_c = 0.5 nm. When $\varepsilon'' = 0.1$ as shown in Fig. 5.2(a), X^* is the largest at $\varepsilon' = -1$ for $d \geq 1$ nm. However, at d = 0.1 nm, there exists a dip in X^* for $-3.3 < \varepsilon' < -0.3$ and the value of X^* at $\varepsilon' = -1$ is even less than that at d = 1 nm. This is caused by the imposed cutoff β_c in the upper integrand of Eq. (5.2) as will be discussed later. When $d \to 0$, the peak shifts to $\varepsilon' = 0$ at which X^* = 1. When ε' is kept at −1 as shown in Fig. 5.2(b), at d = 100 nm and 10 nm, reducing the vacuum gap results in an increase in X^* for $0.001 < \varepsilon'' < 10$. However, at d = 1 nm and 0.1 nm, there exists a maximum in X^* and further reduction of d will result in a decrease in X^*. The peak shifts towards larger ε'' as d decreases. Furthermore, as $d \to 0$, X^* reaches its maximum (unity) when $\varepsilon'' >> 1$. The existence of a peak is again attributed to the imposed cutoff in β.

When $\varepsilon' = -1$ and $\varepsilon'' << 1$, the function $Z(\omega, \beta)$ given in Eq. (5.3) has a peak located at $e^{\beta d} = 2 / \varepsilon''$, which can be deduced from Eq. (5.4). Figure 5.4 plots $Z(\omega, \beta)$ in

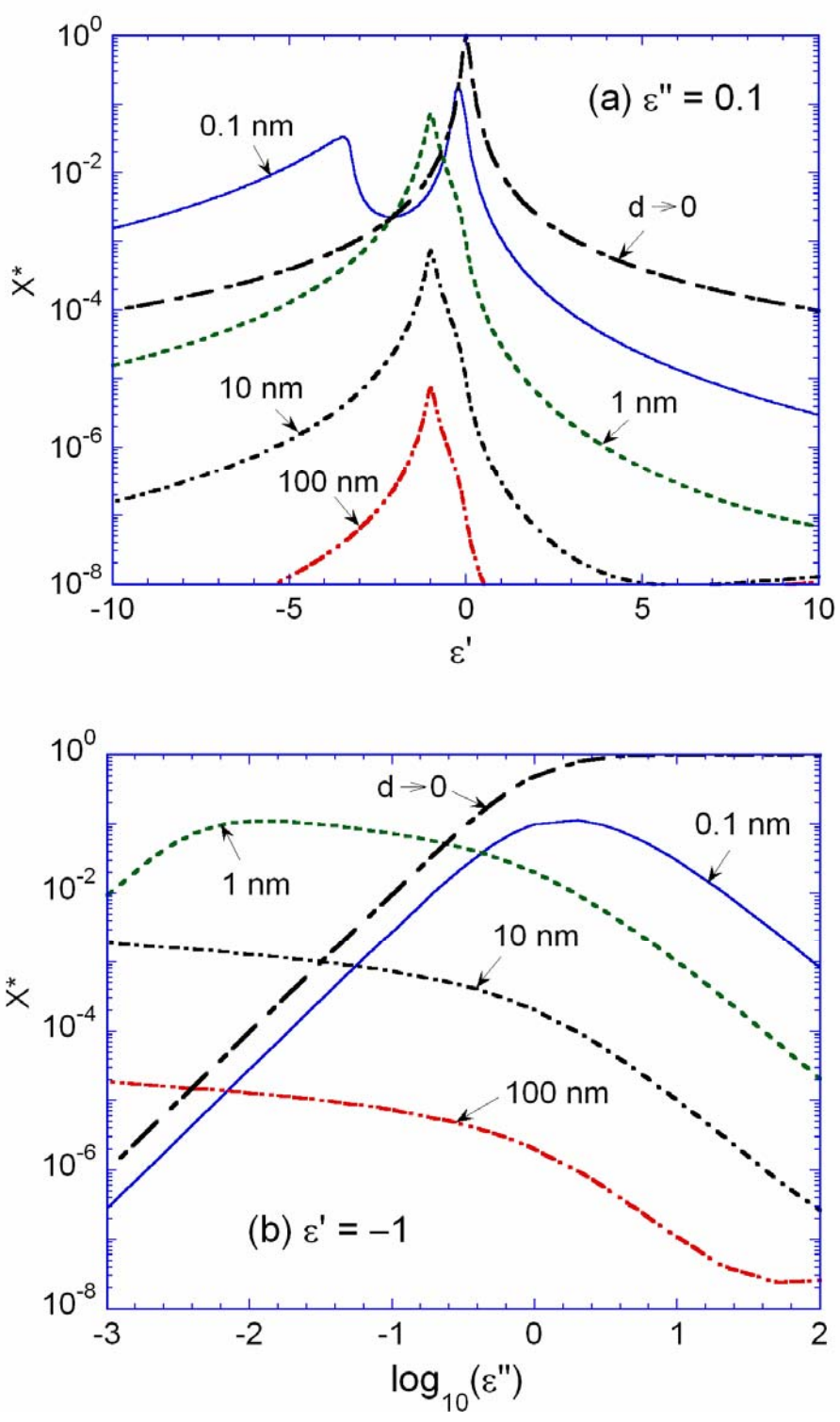

Figure 5.2 Graphs of Z as a function of ε' when $\varepsilon'' = 0.1$ (a) and ε'' when $\varepsilon' = -1$ (b) at different vacuum gaps.

terms of $\xi = \beta d$ for several ε' and ε'' values. As d decreases, the peak shifts towards larger β, and most near-field energy transfer is through modes around this peak. The product of Xd^2 can be obtained as the integration of $Z(\omega,\xi)\xi$ over ξ using Eq. (5.6). Due to the imposed cutoff in β, a significant amount of energy is excluded in calculating the heat flux from the emitter to receiver at very small vacuum gaps. With d = 0.1 nm and d_c = 0.5 nm, $\xi_c = \beta_c d = 0.2\pi \approx 0.628$. This results in a decrease in X when d is reduced from 1 nm to 0.1 nm for $\varepsilon = -1 + i0.1$ and other cases. On the other hand, setting the

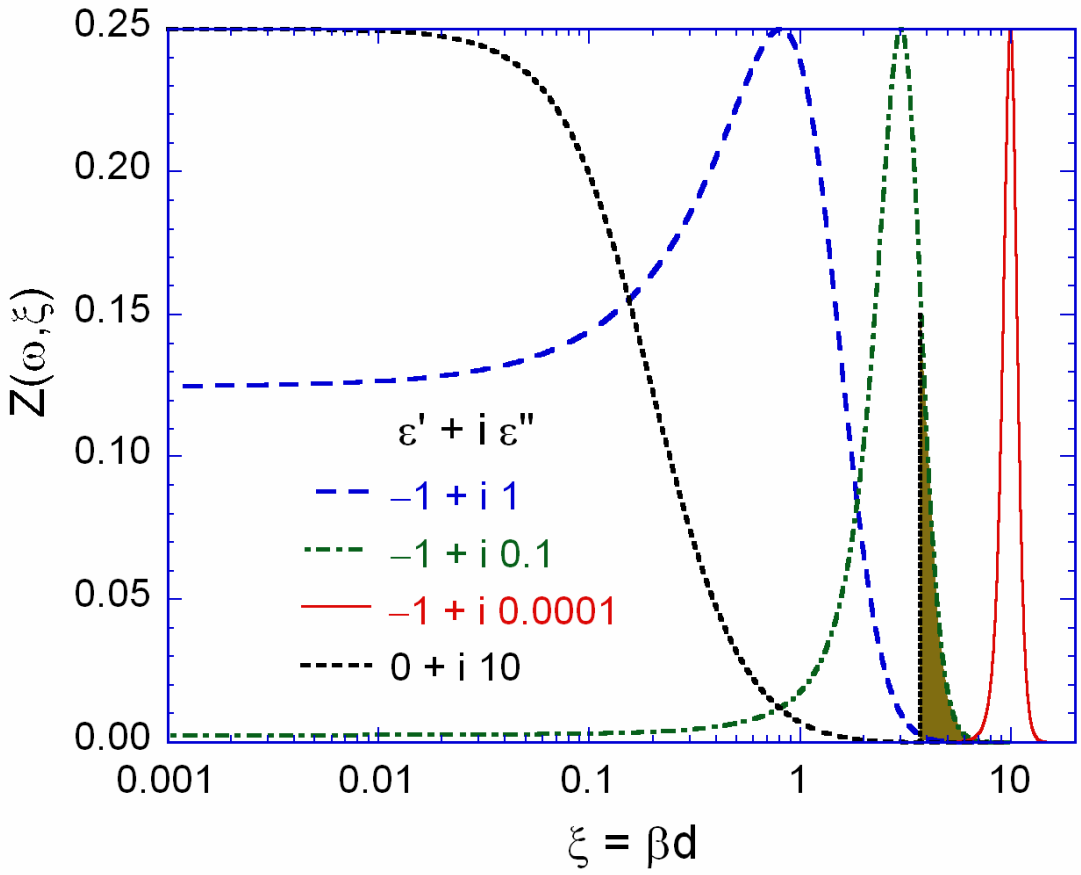

Plot of Z as a function of βd for different ε' and ε'' values. The shaded area shows the reduction of energy transfer modes due to the cutoff imposed in β for $\varepsilon = -1 + i0.1$ with $d_m = 0.6$ nm.

upper limit of β to β_c does not affect the energy transfer at relatively large vacuum gaps. For example, when d = 3 nm, $\xi_c = 6\pi$. Even for $\varepsilon = -1 + i0.0001$, the peak is located near $\beta d = 10$ and the cutoff of $\xi_c = 6\pi$ has little impact on the integration. Hence, most of the energy in these evanescent modes can still contribute to near-field radiation despite the cutoff in β. There exists an optimal distance d_m when X will be maximized. For $\varepsilon = -1 + i0.1$, it can be shown that $d_m = 0.6$ nm and $\beta_m d = 3.77$. When $d = d_m$, the shaded area under the curve $Z(\omega, \xi)$ in the figure represents the reduction of energy transfer due to the cutoff in β for $\varepsilon = -1 + i0.1$. If $d < d_m$, additional reduction of the energy transfer can occur that will reduce the near-field heat flux. At relatively large separation distances, $\varepsilon = 0 + i10$ gives very small Z values for ξ near ξ_c and should result in a relatively small heat flux. However, for very small d values when $d < 0.003$ nm (i.e., $\xi_c < 0.02$), it can be seen from the figure that $Z \approx 0.25$ for $\varepsilon = 0 + i10$ when $\xi < 0.02$. As a result, the integration of Eq. (5.6) gives $X^* = 1$. It can be expected that the maximum heat flux will not only depend on the choice of the dielectric function but also on the distance of separation, i.e., the vacuum gap width.

Figure 5.4 shows the calculated radiative heat flux between the two media ($T_1 = 300$ K and $T_2 = 0$ K) as a function of the vacuum gap for different values of ε' and ε'' when d_c is taken as 0.5 nm. In most cases, ε' is fixed at −1. For the sake of comparison, the energy transfer between two SiC plates is also shown in the figure using a frequency-dependent dielectric function of SiC. By setting the temperature of medium 2 to absolute zero, only the energy transfer from the emitter to the receiver is considered, but not vice versa. It should be mentioned that the use of the approximation in Eq. (5.3)

has been validated by comparison with the original formula based on Fresnel's coefficients, which depend on ω even though the dielectric function itself is independent of ω. The comparison verifies that the calculated near-field heat flux is almost the same with the largest relative difference within 0.1% at d = 100 nm. At 300 K, the maximum achievable near-field heat flux calculated from Eq. (5.5) is 1.4×10^{11} W/m^2, which is represented as the dashed horizontal line in Fig. 5.4. The radiation flux between two

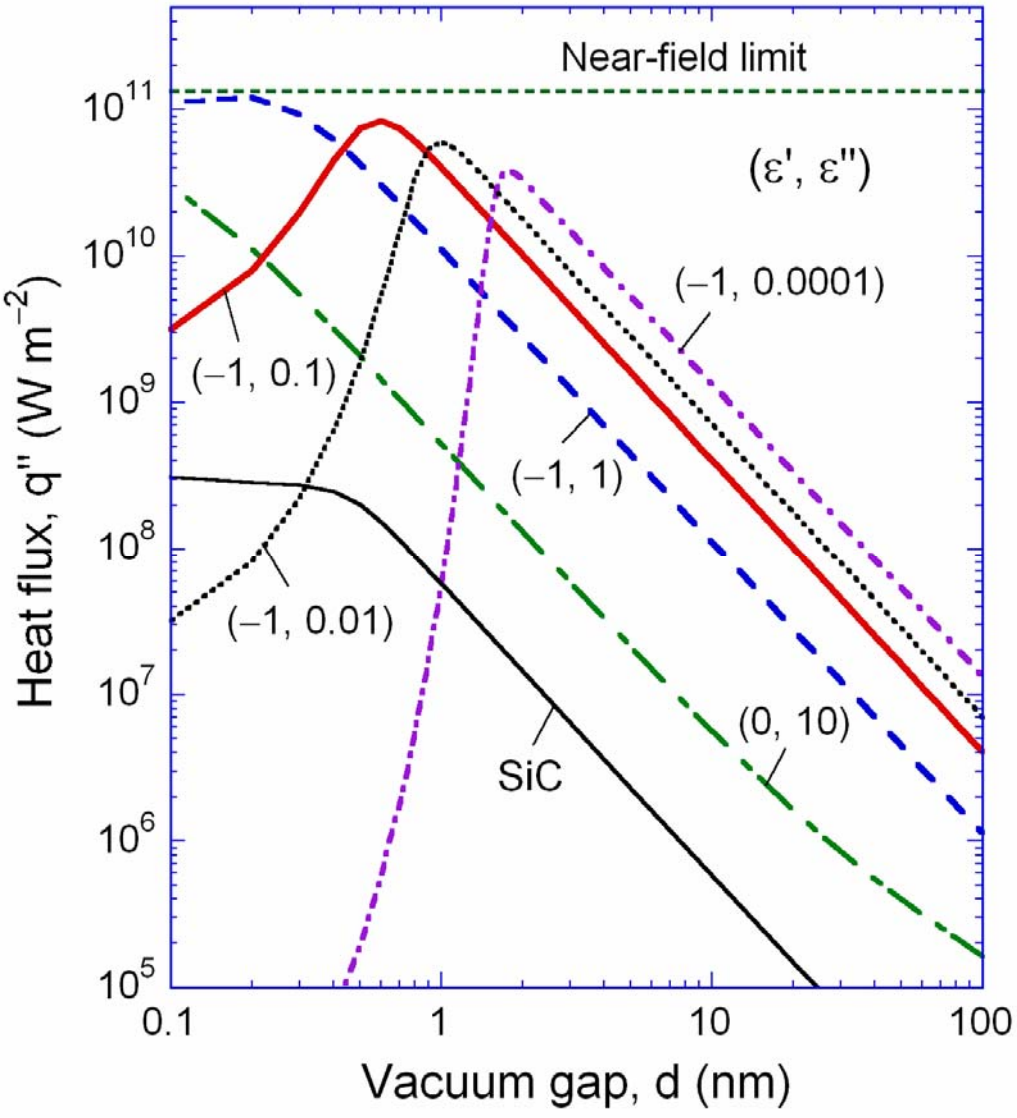

Figure 5.4 Radiative heat flux versus gap width for different dielectric functions. The temperatures of the two media are set to be 300 K and 0 K.

blackbodies maintained at 300 K and 0 K is 459 W/m^2, several orders of magnitude smaller than near-field radiative transfer.

The cutoff in β sets an upper limit on the maximum energy transfer between the two media. Hence, for each of the dielectric functions, there exists an optimal vacuum gap width (d_m) for maximum energy transfer. For $\varepsilon = -1 + i0.1$, it can be seen from Fig. 5.4 that $d_m = 0.6$ nm, which also maximizes X as explained previously. The value of d_m decreases with increasing ε'', implying that the reduction in the energy transfer begins to take place at smaller vacuum gaps. This is consistent with the Z functions shown in Fig. 5.3. Furthermore, the d^{-2} dependence in the energy transfer exists only when $d > d_m$. At $d > 2$ nm, increasing ε'' results in a decrease of the heat flux. When $\varepsilon = 0 + i10$, the radiative heat flux is generally much smaller than those with $\varepsilon' = -1$ but will keep increasing towards the maximum as d unrealistically approaches zero. For the selected dielectric functions with $\varepsilon' = -1$ and $\varepsilon'' << 1$, the energy transfer can be orders of magnitude greater than that between SiC plates. This is because of the excitement of surface waves at almost every frequency since the dielectric function is assumed to be independent of frequency. While no such materials exist and a frequency-independent dielectric function is nonphysical, the calculated results provide a limit of near-field heat flux at finite distances and may help in the selection of appropriate dielectric functions that will result in optimal heat flux at different vacuum gaps. By introducing the cutoff in β, even for SiC, the d^{-2} trend ceases to exist at d < 0.6 nm. Instead, the near-field radiative transfer reaches a plateau below d = 0.5 nm.

The effect of β_c on the heat flux is studied by setting d_c = 0.25, 0.5, and 1 nm. The result for $\varepsilon = -1 + i0.0001$ is shown in Fig. 5.5. Increase in d_c will decrease β_c and

hence will reduce the number of modes for heat transfer. As mentioned earlier, the maximum heat flux at $d \to 0$ is proportional to d_c^{-2}. When d_c = 1 nm, the cutoff in β starts to affect the heat transfer at d < 4 nm and the peak is at d_m = 3.6 nm. It can be seen that d_m is proportional to d_c; this is also true for $\varepsilon = -1 + i0.1$, although not shown in the graph. The peak heat flux varies as β_c^2; that is to say, the ratio of the peak heat flux to the limiting near-field heat flux at $d \to 0$ remains the same.

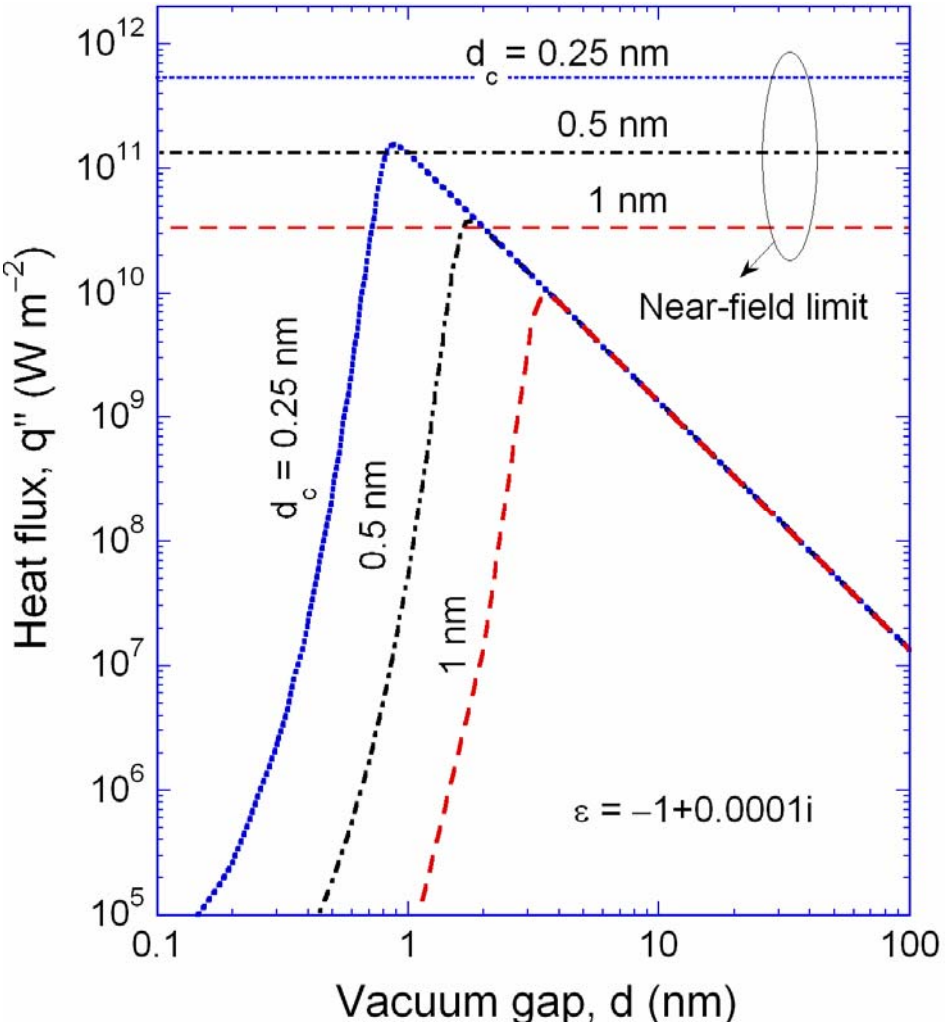

Figure 5.5 Influence of cutoff wavevector β_c on the heat transfer between two media at 300 K and 0 K, respectively, when $\varepsilon = -1 + i0.0001$ for both media.

This chapter describes an investigation of the maximum energy flux between two parallel plates separated by a vacuum gap from 0.1 to 100 nm. An upper bound is imposed to the parallel wavevector component in the analysis based on fluctuation-dissipation theory. Due to the cutoff in the wavevector, the energy transfer deviates from the d^{-2} dependence at sub-nanometer distances. The maximum enhancement occurs when ε' is around −1. Furthermore, the maximum heat flux depends on the vacuum gap and ε'' value when ε' is set to −1. The effect of dispersion on the maximum achievable hat flux will be further examined in the subsequent chapter.

CHAPTER 6

PARAMETRIC OPTIMIZATION OF DIELECTRIC FUNCTIONS FOR MAXIMIZING NANOSCALE RADIATIVE TRANSFER

In Chapter 5, the maximum achievable radiative heat flux between two parallel plates was investigated using a frequency-independent dielectric function for both plates. By introducing a cutoff on the parallel wavevector component, we notice that the ideal (complex) dielectric function $\varepsilon = \varepsilon' + i\varepsilon''$ that would maximize the near-field radiative transfer should be $\varepsilon' = 1$ and $\varepsilon'' << 1$. Such a dielectric function can excite surface polaritons at every frequency. However, real materials can approximate such a behavior only in a relatively narrow spectral interval due to dispersion. Hence, an intriguing question always exists about what kind of real materials will maximize the energy transfer during near-field thermal radiation.

As discussed in Chapter 2, the dielectric function of many materials can be described by either the Drude model or the Lorentz model. The Drude model is commonly used for metals and doped semiconductors, while the Lorentz model is often employed for the dielectric function of polar materials. Generally speaking, good conductors are not ideal for near-field energy transfer since their plasma frequencies are in the ultraviolet region. Heavily doped Si, however, is a good candidate since the plasma frequency can be tuned by changing the doping concentration. For a 1-nm separation (vacuum gap) and near room temperature, radiative transfer between two Si plates with a doping concentration of 10^{19} cm^{-3} is around five orders of magnitude greater than that between two blackbodies as seen in Chapter 4. Nanoscale radiation in polar materials such as SiC is on the same order as that in doped Si since surface phonon polaritons can

be excited, resulting in nearly monochromatic heat transfer. It will be very useful to know how each parameter in the dielectric function models affects the near-field radiation and, moreover, whether there exist optimal set(s) of parameters that will maximize near-field heat transfer under certain constraints. In this Chapter, a parametric study is performed to investigate the effect of different parameters in the dielectric function models on near-field heat transfer by using fluctuational electrodynamics. Optimal values of these parameters are obtained that maximize nanoscale radiative transfer between two plates. In addition, the effect of temperature on the adjustable parameters is also investigated.

6.1 Objective Function and Adjustable Parameters

The total radiative heat flux between two parallel plates at temperatures T_1 and T_2, separated by a vacuum gap d, is given by

$$q'' = \frac{1}{\pi^2}\int_0^\infty d\omega\left[\Theta(\omega,T_1)-\Theta(\omega,T_2)\right]\int_0^{\beta_c} s(\omega,\beta)\,d\beta \tag{6.1}$$

As mentioned before, the upper integration limit β_c is related to the crystalline lattice constant and it prevents the divergence in heat transfer as $d \to 0$. This Chapter aims at maximizing the near-field radiative heat transfer between two plates and thus Eq. (6.1) is the objective function. Near-field energy transfer is dominated by evanescent waves $(\beta > \omega/c)$ and the contribution from propagating waves can be neglected. For real materials, β_c affects the heat transfer only for d < 1 nm. Since this Chapter only deals with cases with d > 1 nm, β_c is set to infinity for all calculations. On simplification of Eq. (2.10), $s(\omega,\beta)$ for $\beta >> \omega/c$ can be expressed as:

$$s(\omega,\beta)=\frac{4\beta\varepsilon''^{2}e^{-2\beta d}}{\left|\left(\varepsilon+1\right)^{2}-\left(\varepsilon-1\right)^{2}e^{-2\beta d}\right|^{2}} \tag{6.2}$$

which is a function of the dielectric function of the media. From the objective function defined by Eq. (6.1), the calculation of overall radiative heat flux involves integration over both ω space and β space. Near the resonance frequency, the peak location of the integral of $s(\omega,\beta)$ shifts towards larger β values as d decreases; while the peak location of the integral of $\Theta(\omega,T)$ moves to higher ω (to be discussed later) when temperature increases. Therefore, the key for maximizing the near-field heat transfer at certain temperature is to determine the value of ω and corresponding dielectric function so that the peak locations of $\Theta(\omega,T)$ and the integral of $s(\omega,\beta)$ match each other. As seen in Chapter 5, the maximum value of $s(\omega,\beta)$ is $\beta/4$, which can be achieved only when $d\to 0$ and $\varepsilon''>>\varepsilon'$. At finite vacuum gaps and for real materials, the value of $s(\omega,\beta)/\beta$ is always less than 0.25. In order to implement the optimization, the influence of dielectric function of materials on the near-field heat transfer needs to be examined. It should be noted that Eq. (5.2) was introduced to illustrate how the dielectric function may be optimized to maximize the heat flux. All the calculations presented below use the more complicated form of $s(\omega,\beta)$.

In terms of plasma frequency and scattering rate, the Drude model can be expressed as

$$\varepsilon(\omega)=\left[n(\omega)+i\kappa(\omega)\right]^{2}=\varepsilon_{\infty}-\frac{\omega_{\mathrm{p}}^{2}}{\omega^{2}+i\omega\gamma} \tag{6.3}$$

Here, ε_0, ω_p, and γ are treated as adjustable parameters to maximize the near-field heat flux. For Si, ε_∞ is approximately 11.7, while for metals it is on the order of 1. The minimum of ε_∞ is 1, since the refractive index for any material cannot be less than that for vacuum at high frequencies. The plasma frequency for most metals lies in the UV region and is much higher than the characteristic frequencies of thermal sources (ω_T). When $\omega < \omega_\mathrm{p}$, ε' becomes negative and the extinction coefficient κ is much greater than the refractive index n. On the other hand, the scattering rate indicates loss due to collisions of electrons and affects the width of the spectral heat flux. Hence, appropriate selection of these parameters is important for the optimization of near-field heat transfer.

On the other hand, the Lorentz model in terms of plasma frequency is given by,

$$\varepsilon(\omega) = \varepsilon_\infty + \frac{\omega_\mathrm{p}^2}{\omega_0^2 - i\gamma\omega - \omega^2} \tag{6.4}$$

where $\omega_\mathrm{p}^2 = \varepsilon_\infty \left(\omega_\mathrm{LO}^2 - \omega_0^2 \right)$, and ω_LO and ω_0 are frequencies corresponding to the longitudinal and transverse phonons, respectively. The high-frequency term ε_∞ for some common dielectrics are 2.2 for SiO_2, 6.7 for SiC, and 3.01 for MgO. When $\omega_0 < \omega < \omega_\mathrm{LO}$, ε' is negative and this spectral region is of particular interest for near-field radiation enhancement. Note that ω_p determines the strength of the oscillators in the Lorentz model. Furthermore, when $\omega_0 = 0$, Eq. (6.4) reduces to Eq. (6.3). Hence, the Lorentz model provides an additional adjustable parameter (ω_0) compared to the Drude model.

6.2 Results and Discussion

In this section, the influence of different adjustable parameters in both the Drude and the Lorentz models on the near-field heat flux is investigated. The effect of temperature on different parameters in the Drude model is also studied.

6.2.1 **The Drude Model**

Rearranging Eq. (6.3), the real and imaginary parts of the dielectric function given by the Drude model can be expressed as

$$\varepsilon'(\omega) = \varepsilon_\infty - \frac{\omega_p^2}{\omega^2 + \gamma^2} \tag{6.5a}$$

and

$$\varepsilon''(\omega) = \frac{\gamma\omega_p^2}{\omega^3 + \omega\gamma^2} \tag{6.5b}$$

It can be seen that increasing either ε_∞ or γ will increase ε', while increasing ω_p will decrease ε'. However, ε'' is independent of ε_∞ and its dependence on γ and ω_p is opposite to that of ε'. Figure 6.1 shows the spectral variation of the real and imaginary parts of the dielectric function calculated using the Drude model with different scattering rates when $\varepsilon_\infty = 1$ and $\omega_p = 10^{14}$ rad/s. At smaller values of γ (γ = $0.001\,\omega_p$, $0.01\,\omega_p$, and $0.1\,\omega_p$), ε' is almost independent of γ over the calculated spectral range. Also, when $\omega \geq 2\times10^{14}$ rad/s, ε' approaches to ε_∞. As a result, the material starts to behave as a dielectric and there is no significant near-field enhancement. On the other hand, ε'' is proportional to γ for small γ values.

Figure 6.2 shows the spectral heat flux at d = 10 nm calculated according to the

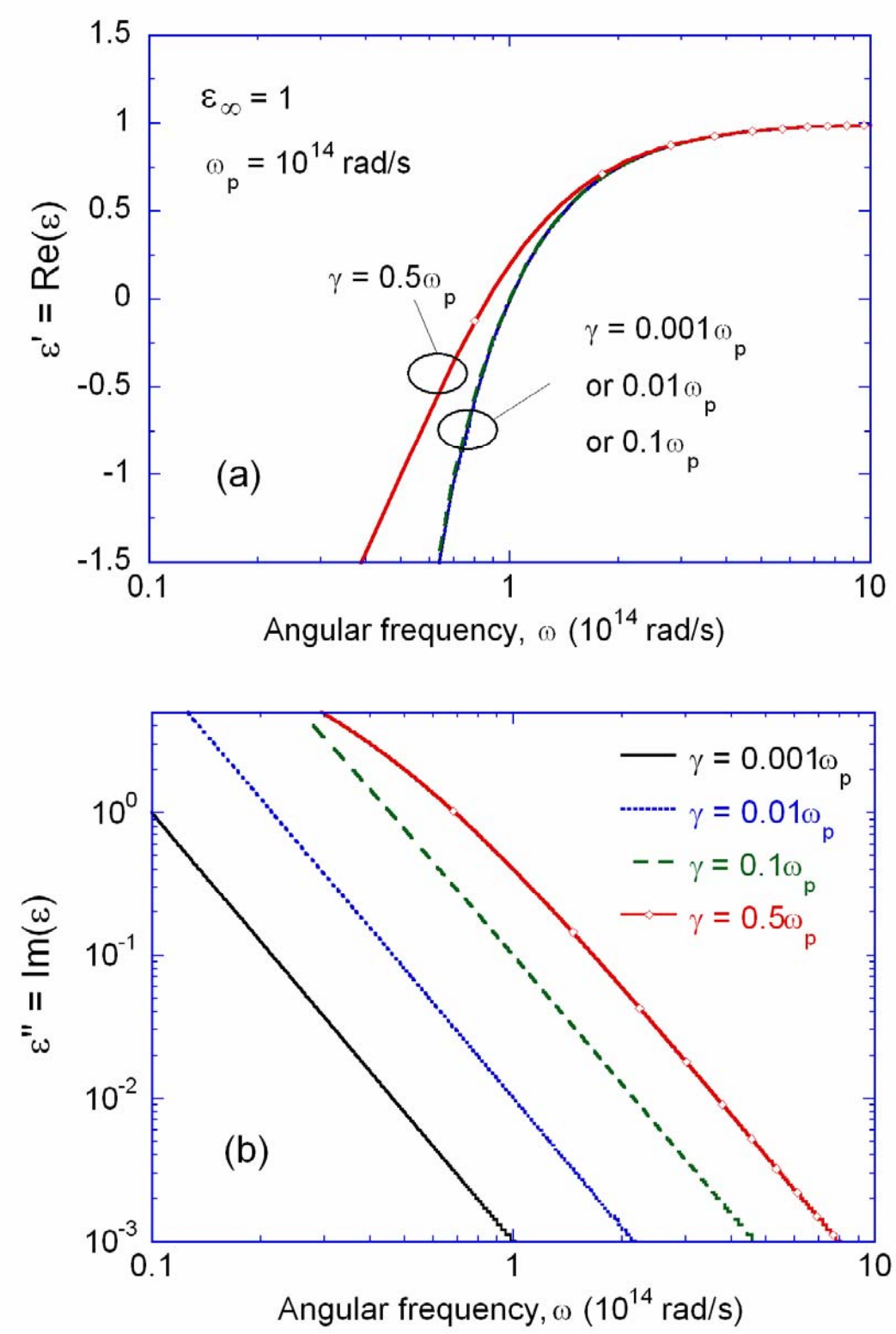

Figure 6.1 (a) Real and (b) imaginary parts of the dielectric function calculated from the Drude model for varying scattering rates with $\varepsilon_\infty = 1$ and $\omega_p = 10^{14}$ rad/s.

Drude model with $\varepsilon_\infty = 1$ and $\omega_p = 10^{14}$ rad/s for different γ values. In the calculation, the temperatures of the media are set to T_1 = 300 K and T_2 = 0 K and the frequency corresponding to the heat flux peak is denoted by ω_{max}. It can be seen that $\omega_m \approx 7.0\times10^{13}$ rad/s for the three smaller γ values and $\omega_{max} \approx 6.0\times10^{13}$ rad/s for $\gamma = 0.5\omega_p$. The peak frequencies in the spectral heat flux are at the same location as that where $\varepsilon' \approx -1$ shown in Fig. 6.1(a). The large energy transfer near ω_{max} is due to the excitation of surface plasmon polaritons, although the polariton resonance frequency may be slightly different from ω_{max}. At very large frequencies, the energy transfer is reduced due to the dielectric behavior of the materials as mentioned before. At very low frequencies, $\varepsilon'' >> \varepsilon'$ but this does not result in a large heat flux at $d \geq 1$ nm. Notice that the scattering rate determines the width of the spectral heat flux curve. From Fig. 6.2, for smaller scattering rates, the spectral heat flux has a sharper peak but narrower width. Considering that it is the area under the spectral heat flux curve that represents the total heat flux, an optimal value of γ should be obtained in order to maximize the energy transfer. Note that the spectral plots of ε' and ε'' predict the location of the peak and the shape of the spectral heat flux curve, respectively. It should be noted that the trend discussed above based on $d = 10$ nm is generally applicable to the situations when $1 \text{ nm} \leq d \leq 100$ nm.

Figure 6.3 is a flow chart showing the methodology adopted in this study in order to determine the optimum plasma frequency and scattering rate. The optimization technique adopted in this study can be further understood from Fig. 6.4 which is a contour plot of heat flux with γ/ω_p and ω_p when $\varepsilon_\infty = 1$. The emitter and the receiver

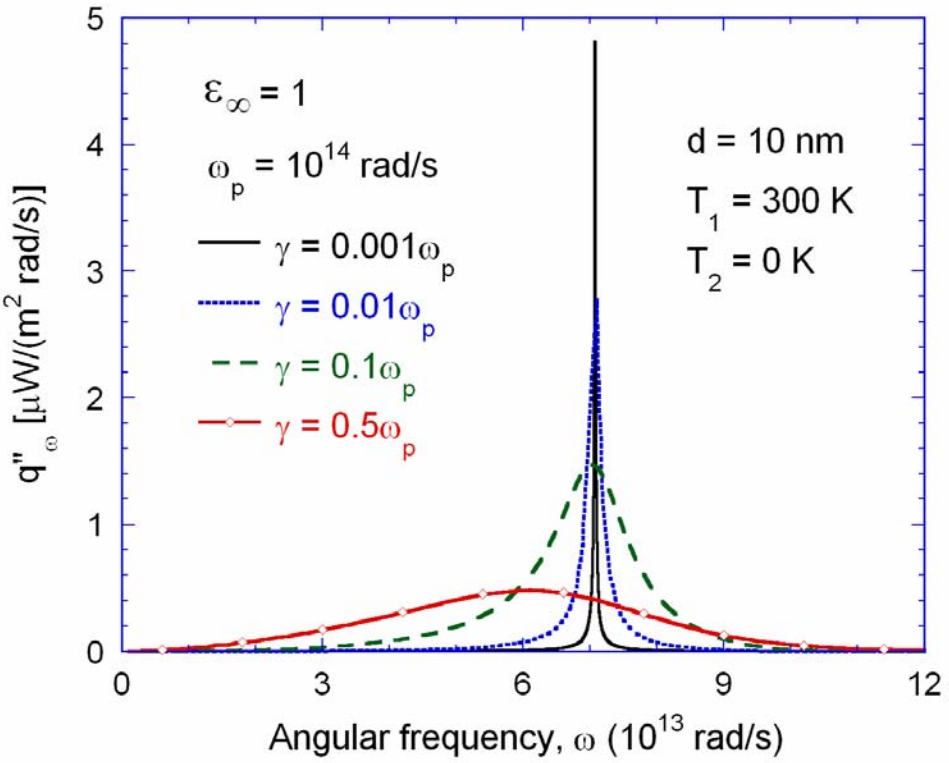

Figure 6.2 Spectral heat flux for different γ at d = 10 nm, with $\varepsilon_\infty = 1$ and $\omega_p = 10^{14}$ rad/s. The temperatures are T_1 = 300 K and T_2 = 0 K.

are maintained at 300 K and 0 K respectively and the vacuum gap is set at 10 nm. Figure 6.4(a) is the plot of heat flux over a large range of γ/ω_p and ω_p values. From Fig. 6.4(a), it is seen that the heat flux is optimum when $0.15 < \gamma/\omega_p < 0.2$ and $8.5\times10^{13} < \omega_p < 10^{14}$ where the unit of ω_p is rad/s. Within this range of scattering rate and plasma frequency, the heat flux varies within 2.5% of the maximum. The heat flux is then calculated for the selected range of scattering rate and plasma frequency at smaller resolution which is shown in Fig. 6.4(b). From Fig. 6.4(b), it is seen that the heat flux is maximum when $\omega_p \approx 9.5\times10^{13}$ rad/s and the scattering rate is around 1.6×10^{13} rad/s. Similar optimization procedure is adopted for all other cases considered in this study.

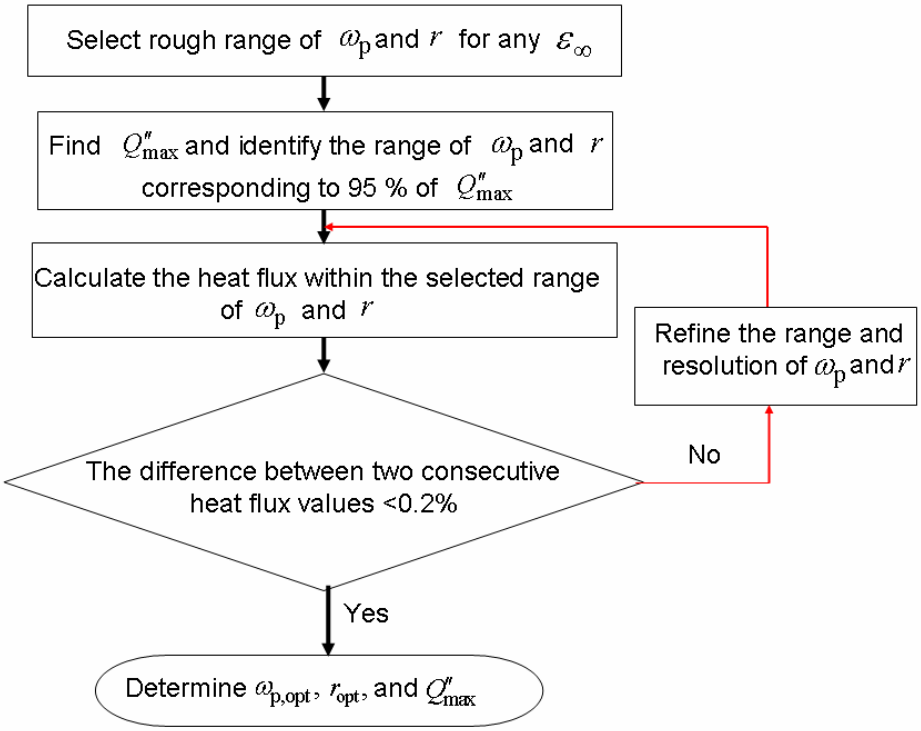

Figure 6.3 Flowchart showing the optimization methodology adopted in this study where r is the ratio of scattering rate to the plasma frequency.

Figure 6.5 plots the overall heat transfer as a function of γ/ω_p for several values of ω_p when d = 10 nm and $\varepsilon_\infty = 1$. Here again, T_1 = 300 K and T_2 = 0 K. For comparison, the overall heat flux is normalized with respect to that between two blackbodies at T_1 and T_2, respectively. The overall energy transfer is maximum when ω_p is from 8×10^{13} rad/s to 10^{14} rad/s and γ/ω_p is from 0.1 to 0.2. While a maximum heat flux exists for a given ε_∞, it can be seen that the peak is not very sharp, and hence, γ and ω_p may be varied in

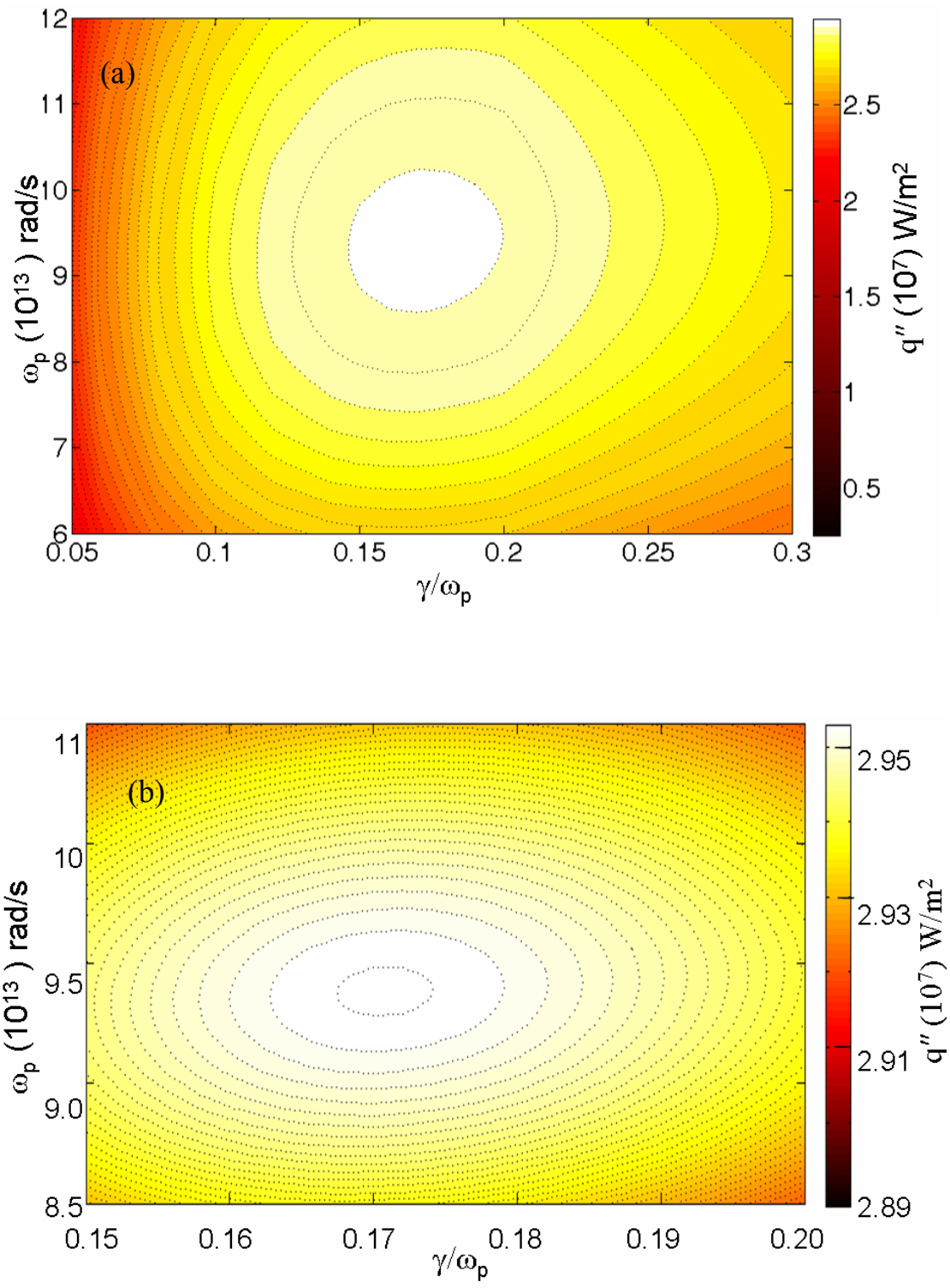

Figure 6.4 Contour plot of heat flux with respect to γ/ω_p and ω_p. In Fig. 6.4(b) the resolution in γ/ω_p and ω_p is increased in order to obtain the maximum heat flux.

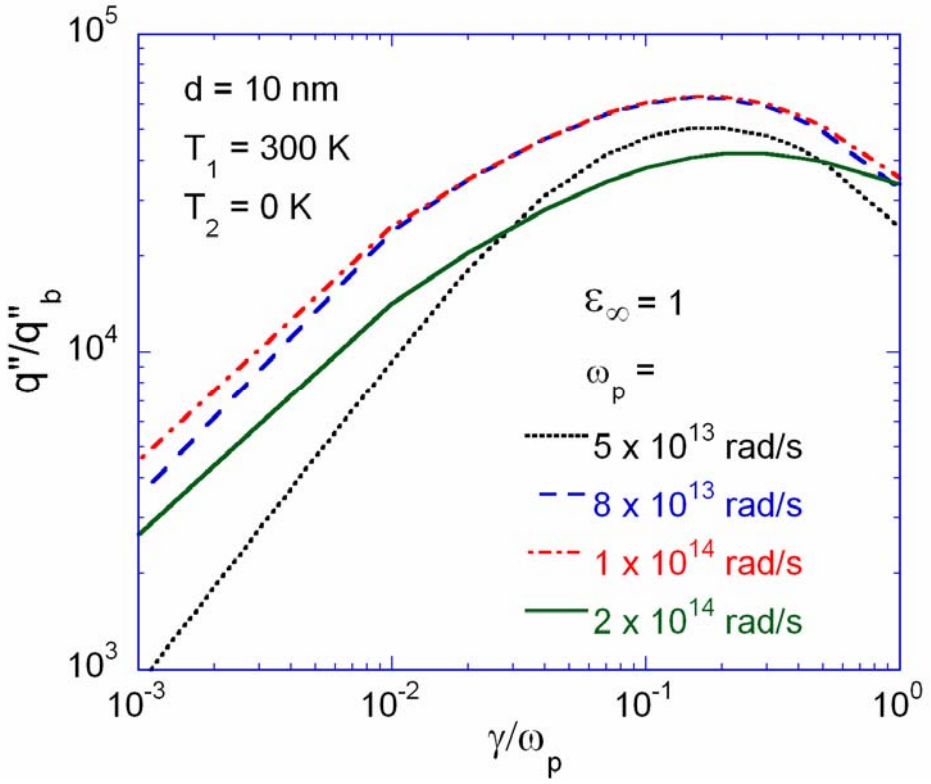

Figure 6.5 Overall heat flux between two semi-infinite media at T_1 = 300 K and T_2 = 0 K as a function of r at different ω_p when d = 10 nm and $\varepsilon_\infty = 1$. The calculated heat flux is normalized with respect to the heat transfer between two blackbodies maintained at T_1 and T_2, respectively.

a large range and can still result in large near-field radiation enhancement. Good conductors do not result in large near-field enhancement at room temperature since their $\omega_p > 4\times10^{15}$ rad/s. Notice that the overall heat flux at γ/ω_p = 0.1 is more than one order of magnitude greater than that at γ/ω_p = 0.001, though the latter has a higher peak in the spectral heat flux. This shows that a higher but narrower peak does not necessarily result in large energy transfer. Thus, a very small scattering rate is not good for heat-transfer enhancement in the near field. A very large scattering rate will also reduce the

overall heat flux because of the low peak spectral heat flux as well as the reduction in $\omega_{\max}$.

Figure 6.5 provides a range in which the optimal values of ω_p and γ exist for $\varepsilon_\infty = 1$. Within this range, the heat flux is calculated with different combinations of ω_p and γ using small intervals to determine their optimal values. The process is then repeated for $\varepsilon_\infty = 5$ and 10. Here onwards, optima of ω_p and γ are referred to as $\omega_{p,opt}$ and γ_{opt}, respectively. The heat flux calculated for different ε_∞ at the corresponding $\omega_{p,opt}$ is shown in Fig. 6.6 as a function of γ/ω_p. Each curve has a maximum q''_{max} corresponding to γ_{opt} and these maxima are marked as A, B, and C sets, whose parameters are summarized in Table 6.1. It can be seen that a larger ε_∞ always results in a smaller heat flux. When ε_∞ increases, $\omega_{p,opt}$ increases but γ_{opt} decreases. The heat flux exhibits a plateau around $\omega_{p,opt}$ and γ_{opt}. The uncertainty of q'' is estimated to be 1%. The sensitivity of q'' to the change of ω_p or γ is investigated by varying these parameters individually. It is found that a 10% change in ω_p or a 20% change in γ away from the corresponding optimal value will result in about 1% reduction in the heat flux. However, the effect is not linear and, generally speaking, if one wishes to achieve a heat flux that exceeds $0.95\, q''_{max}$, then ω_p can be varied within 20% of $\omega_{p,opt}$ and γ can be varied within 40% of γ_{opt}, since q'' is less sensitive to γ than ω_p.

A better understanding of the maximum heat transfer in terms of the optimized parameters in the Drude model can be obtained by examining the spectral dependence of

dielectric function and energy flux. Figures 6.7(a) and (b) plot ε' and q''_ω for sets A, B,

Table 6.1. List of parameters for different materials or sets

Material or Set	ε_∞	ω_0 (rad/s)	ω_p (rad/s)	γ (rad/s)
A	1	—	9.4×10^{13}	1.6×10^{13}
B	5	—	1.6×10^{14}	5.76×10^{12}
C	10	—	2.1×10^{14}	3.15×10^{12}
D	3.01	7.56×10^{13}	2.0×10^{14}	1.06×10^{13}
E	1	7.56×10^{13}	1.45×10^{14}	2.15×10^{13}
GaAs	11	5.05×10^{13}	7.21×10^{13}	3.77×10^{11}
MgO	3.01	7.56×10^{13}	1.96×10^{14}	1.44×10^{12}
SiC	6.7	1.49×10^{14}	2.71×10^{14}	9.0×10^{11}
Si-19	11.7	—	8.92×10^{13}	6.12×10^{13}
Si-20	11.7	—	2.82×10^{14}	9.34×10^{13}

and C with ε_∞ = 1, 5, and 10, respectively. Note that the values of $\omega_{\max}$ (i.e., the frequency corresponding to the peak of q''_ω in Fig. 6.7(b) are very close for different ε_∞ values. However, as plotted in Fig. 6.7(a), the slope of the $\varepsilon'(\omega)$ curve near $\omega_{\max}$ is higher with larger ε_∞, resulting in a narrower q''_ω. When $\varepsilon_\infty = 1$, there exists a negative ε' over a broad spectral range and this leads to the greatest enhancement in the total heat flux. In fact, $\omega_{\max}$ can be approximately obtained by setting $\varepsilon' = -1$ in Eq. (6.5a), that is,

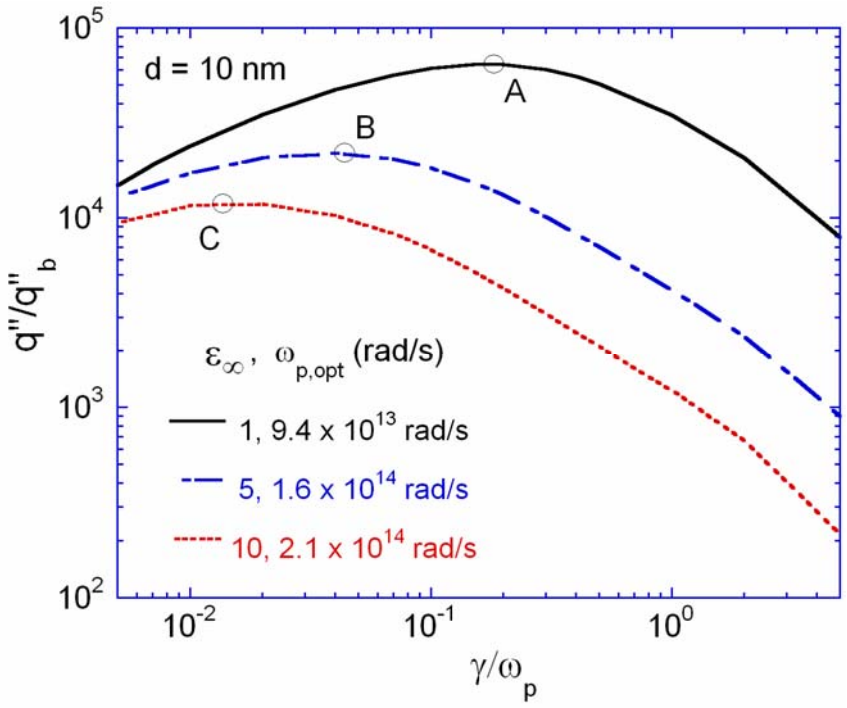

Figure 6.6 Normalized overall heat flux as a function of γ/ω_p calculated at $\omega_{p,opt}$

$$\omega_{max} = \sqrt{\frac{\omega_p^2}{\varepsilon_\infty + 1} - \gamma^2} \tag{6.6}$$

It is clear that as ε_∞ becomes larger, $\omega_{p,opt}$ has to increase but γ_{opt} has to decrease in order to keep ω_{max} nearly the same to match with the Planck oscillator function $\Theta(\omega, T)$. The decrease in γ_{opt} with increasing ε_∞ results in a narrower peak in the spectral energy flux as shown in Fig. 6.7(b). Consequently, the maximum heat flux decreases as ε_∞ increases.

6.2.2 Effect of Temperature

All the cases discussed before in this Chapter are calculated at $T_1 = 300$ K. When the temperature changes, the distribution of the mean energy of the Planck's oscillator

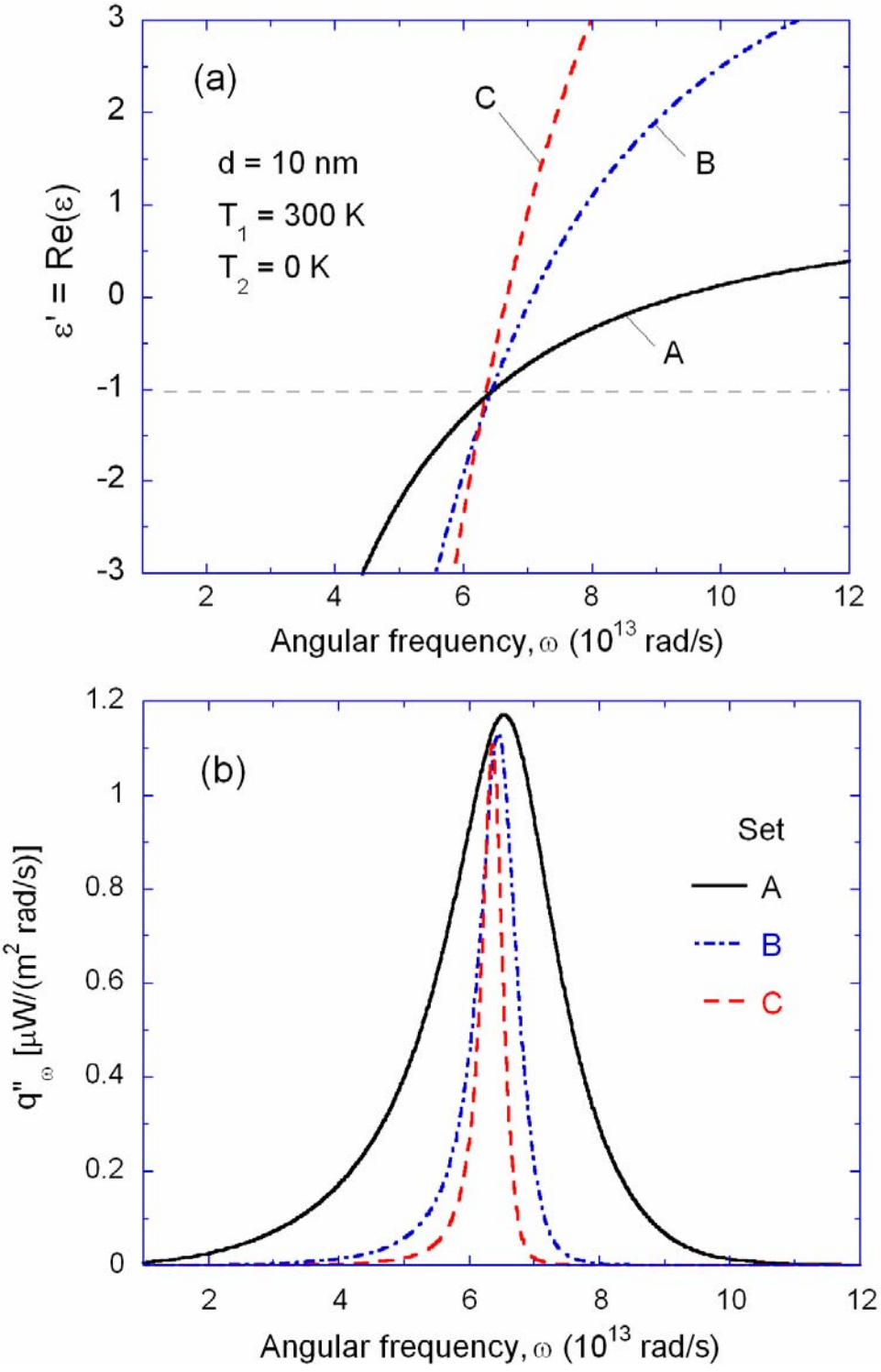

Figure 6.7 Spectral plot of dielectric function and energy flux calculated at $\omega_{p,opt}$ and γ_{opt} for sets A, B, or C as listed in Table 6.1: (a) the real part of dielectric function, and (b) spectral energy flux.

$\Theta(\omega,T)$, will also change. The maximum of $\Theta(\omega,T)$ when plotted against ω is located at $\omega=0$ since $\Theta(\omega,T)$ is a decreasing function of ω. A recent study proposed the use of logarithmic frequency, $\log_{10}(\omega)$, or wavelength, $\log_{10}(\lambda)$, for the Planck blackbody distribution, so that Wien's displacement law is consistent in both the wavelength and the frequency domain (Zhang and Wang, 2009). Similarly, when the near-field heat transfer is considered, by converting $\Theta(\omega,T)$ in terms of the logarithmic frequency, the distribution function becomes $\Theta(\omega,T)\omega$, which has a peak located at ω_{T} (corresponding to a λ_{T}) as shown in Fig. 6.8. Let $X(\omega)=\int_0^\infty s(\omega,\beta)d\beta$ with a peak at $\omega=\omega_{\mathrm{m}}$ and is independent of temperature for given parameters in the dielectric function, the heat transfer can be enhanced by tuning ω_{p} to make ω_{m} approach ω_{T}. Here, the parameters in the Drude model are treated as adjustable in order to find the optimal set, therefore, $X(\omega)$ is independent of temperature although for real materials, these parameters depend on temperature. In Fig. 6.8, three curves of $X(\omega)$ were calculated based on the parameters of dielectric functions corresponding to $\omega_{\mathrm{p,opt}}$ at different temperatures. Notice that when the temperature becomes higher, ω_{T} shifts to higher ω. This indicates that at higher temperatures, ω_{m} should increase for the two peaks to almost overlap, resulting in maximum q''_{ω} at $\omega_{\max}\approx\omega_{\mathrm{m}}\approx\omega_{\mathrm{T}}$. The relationship between $\omega_{\max}$ and $\omega_{\mathrm{p,opt}}$ can be approximated by rearranging Eq. (6.6) as

$$\frac{\omega_{\max}}{\omega_{\mathrm{p,opt}}}=\sqrt{\frac{1}{\varepsilon_\infty+1}-\left(\frac{\gamma_{\mathrm{opt}}}{\omega_{\mathrm{p,opt}}}\right)^2} \tag{6.7}$$

where $\gamma_{\text{opt}} / \omega_{\text{p,opt}}$ does not change when temperature increases indicating that $\omega_{\text{max}} / \omega_{\text{p,opt}}$ is independent of temperature for a given ε_∞. If the heat flux is optimized at $\omega_{\text{max}} \approx \omega_{\text{T}}$, then ω_{max} / T should remain constant; subsequently, $\omega_{\text{p,opt}} / T$ should stay the same. This suggests that $\omega_{\text{p,opt}}(T)$ should be proportional to temperature and can be calculated based on the value at 300 K using $\omega_{\text{p,opt}}(T) = \omega_{\text{p,opt}}(300\ \text{K})T / 300$. From Zhang and Wang (2009), the peak wavelength of $\Theta(\omega, T)\omega$ can be calculated from $\lambda_{\text{T}} T = 9034.6\ \mu\text{m}\cdot\text{K}$. Therefore, for T_1 = 300, 1000, and 2000 K, ω_{T} should be around 6.25×10^{13}, 2.08×10^{14}, and 4.17×10^{14} rad/s, respectively. The values of ω_{max} calculated from Eq. (6.7) are 6.43×10^{13}, 2.13×10^{14}, and 4.18×10^{14}, which are 3% higher. Because of the scaling, here, it is interesting to point out that at T = 300 K, λ_{T} is around 30 μm, which is nearly three times longer than that predicted by the conventional displacement law.

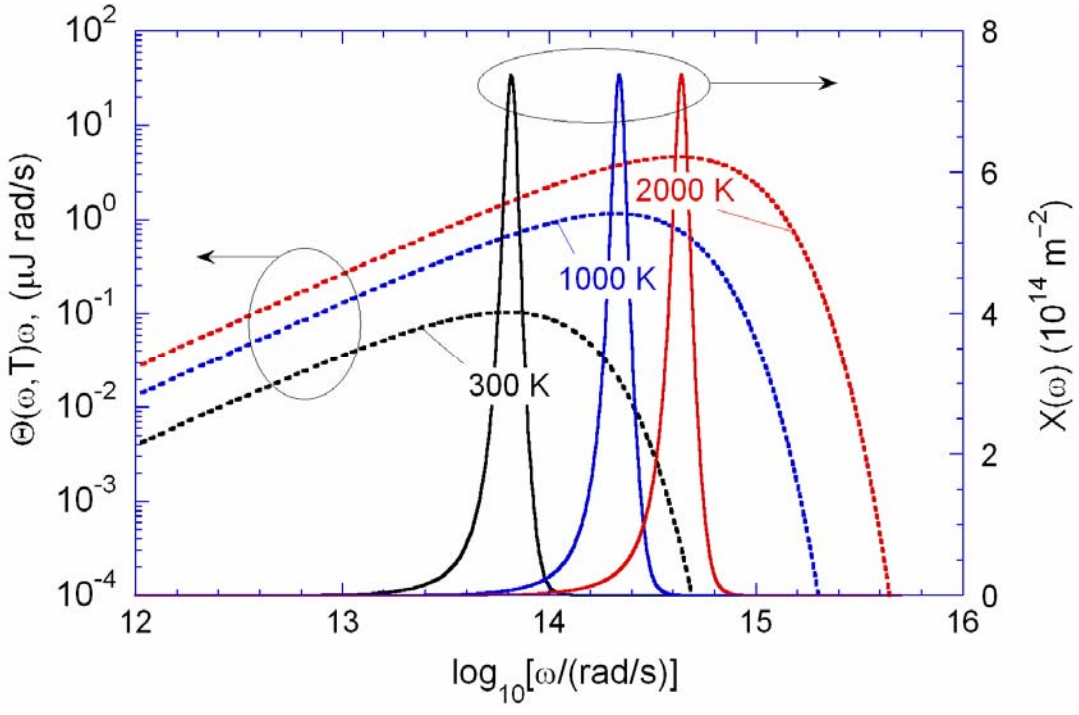

Figure 6.6 Plot of $\Theta(\omega, T)\omega$ and $X(\omega)$ versus $\log_{10}(\omega)$ at T = 300, 1000, and 2000 K.

6.2.3 The Lorentz Model

Consider the near-field heat transfer between two MgO plates as an example. Note that MgO is a polar material whose dielectric function can be approximated by the Lorentz model given in Eq. (6.4) with $\varepsilon_\infty = 3.01$, $\gamma = 7.62$ cm^{-1}, $\omega_\mathrm{p} = 1040$ cm^{-1}, and $\omega_0 = 401$ cm^{-1} (Palik, 1985). Here, only a single oscillator is included, by neglecting the weaker phonon oscillator in MgO. The calculated radiative flux between two plates is shown in Fig. 6.7 for MgO along with a few sets of parameters. When ε_∞ and ω_0 are fixed to those of MgO, the near-field heat transfer is maximized at $\omega_\mathrm{p} = 1056$ cm^{-1} and $\gamma = 56$ cm^{-1}. This set of parameters is referred to as set D. When $\varepsilon_\infty = 1$ and $\omega_0 = 401$ cm^{-1}, the optimal values of ω_p and γ are 770 and 114 cm^{-1}, respectively. In this case, the near-field heat transfer is about three times greater than that between MgO. This set is denoted by E, and the parameters of sets D and E are also listed in Table 6.1. For comparison, the near-field heat transfer for set A, which gives the largest enhancement for the Drude model is also plotted in Fig. 6.9.

In order to understand the influence of different parameters in the Lorentz model on the total heat transfer, $\omega_\mathrm{p,opt}$ and γ_opt are determined using the above-mentioned procedure for the Drude model and tabulated in Table 6.2 for fixed ω_0 and ε_∞. The heat fluxes corresponding to $\omega_\mathrm{p,opt}$ and γ_opt are plotted in Fig. 6.10 as a function of ω_0. For each ε_∞, the radiative heat transfer is maximum when $\omega_0 = 0$ suggesting that the Drude model, when optimized, offers the greatest near-field enhancement for a given ε_∞. Similar to the Drude model, the maximum heat flux for fixed ω_0 decreases with an

Table 2. Values of $\omega_{\mathrm{p,opt}}$ and γ_{opt} with different ω_0 values for $\varepsilon_\infty = 1$, 5, and 10.

	ω_0 (cm^{-1})	$\omega_{\mathrm{p,opt}}$ (cm^{-1})	γ_{opt} (cm^{-1})
$\varepsilon_\infty = 1$	0	500	86
	100	540	90
	200	615	98
	400	770	114
	600	895	124
	800	1020	138
$\varepsilon_\infty = 5$	0	840	30
	100	900	30
	200	1030	34
	400	1300	40
	600	1480	40
	800	1655	40
$\varepsilon_\infty = 10$	0	1120	17
	100	1220	18
	200	1390	19
	400	1710	21
	600	2000	22
	800	2110	22

increase in ε_∞ due to a reduction of γ_{opt} that narrows the spectral width. Both $\omega_{\mathrm{p,opt}}$ and γ_{opt} increase as ω_0 becomes larger. The calculation of $X(\omega)$ shows that ω_{m} also increases with ω_0, resulting in a further shift of ω_{m} away from ω_{T} and consequently a decrease in the total heat flux.

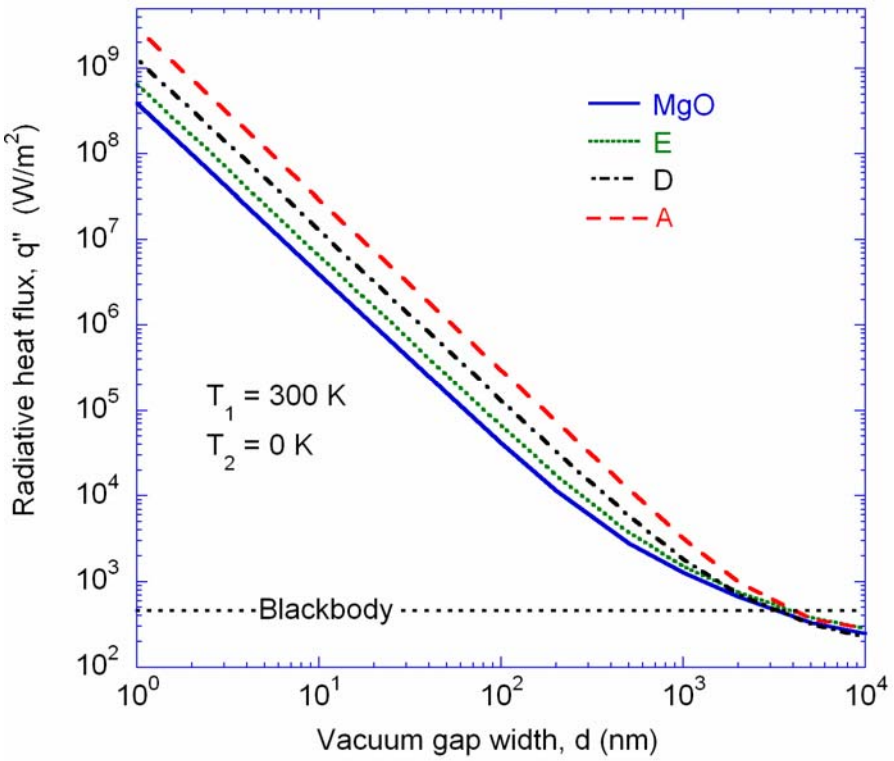

Figure 6.9 Near-field heat flux calculated between two dielectrics using the Lorentz model for MgO and sets A, D, and E.

There are trade-offs among the peak location or resonance frequency, peak magnitude, and peak width. Compared to the Drude model, it is more complicated to optimize the Lorentz model at different temperatures due to restrictions imposed by the finite value of ω_0. Hence, the previous conclusion regarding the temperature dependence of the optimized parameters in the Drude model does not apply to optimization of the Lorentz model. The properties of some common materials whose dielectric functions can be described by the Drude or Lorentz model are listed in Table 6.1. The near-field heat flux between these materials is illustrated in Fig. 6.11. Set A provides the greatest near-field enhancement and the heat flux is nearly an order of magnitude larger than that for any of the real materials listed in Table 6.1. At room temperature, λ_m = 10.5, 15.2, and

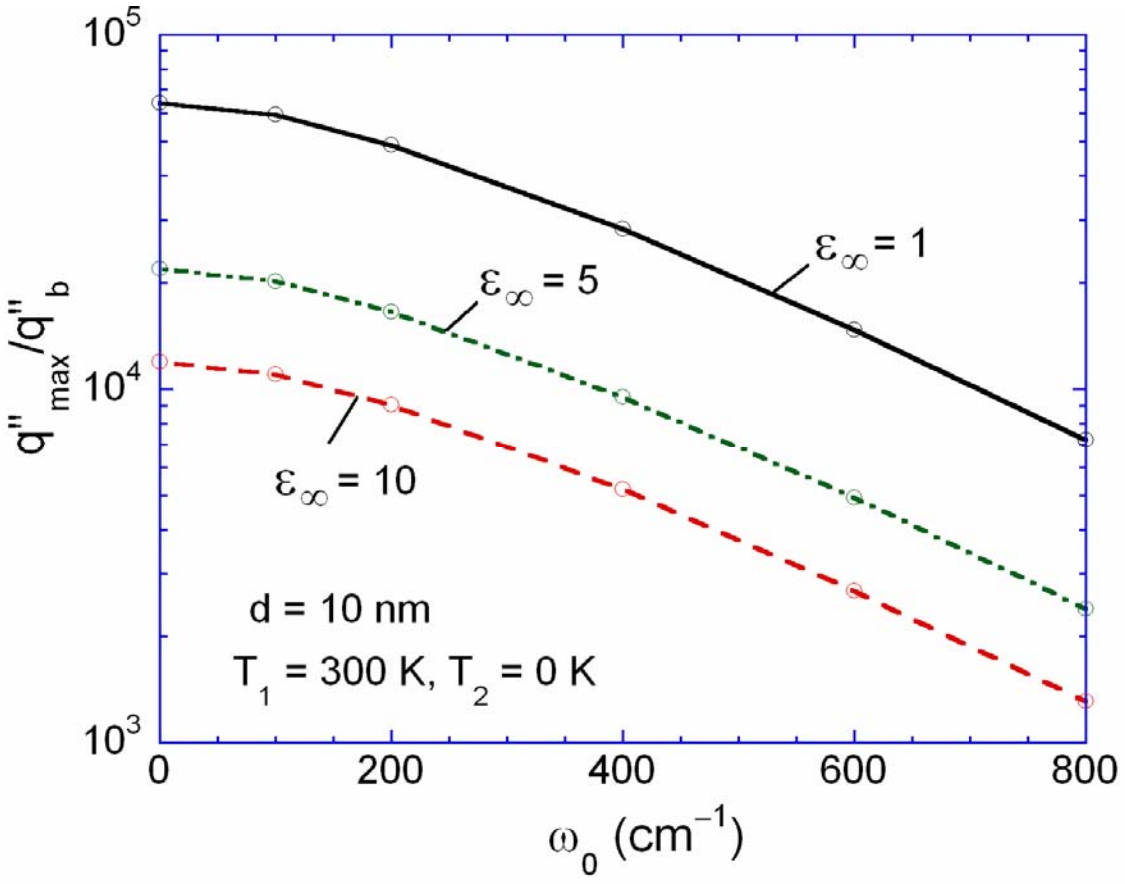

Figure 6.10 Plot of $q''_{\max}/q''_b$ calculated using the Lorentz model, as a function of ω_0 for different ε_∞ values. The optimal parameters are listed in Table 6.2.

34.5 μm for SiC, MgO, and GaAs, respectively. Note that λ_m for GaAs is closest to λ_T, however, MgO gives the greatest near-field enhancement because it has the smallest ε_∞ and the largest γ that yields the broadest peak in the spectral heat flux (Wang *et al.*, 2009). For doped Si, the large plasma frequency is balanced by the large scattering rate which makes the heat transfer comparable to polar materials. However, proper tuning of the plasma frequency is necessary to achieve large radiative transfer. In addition, the relatively large ε_∞ limits the near-field enhancement for doped Si.

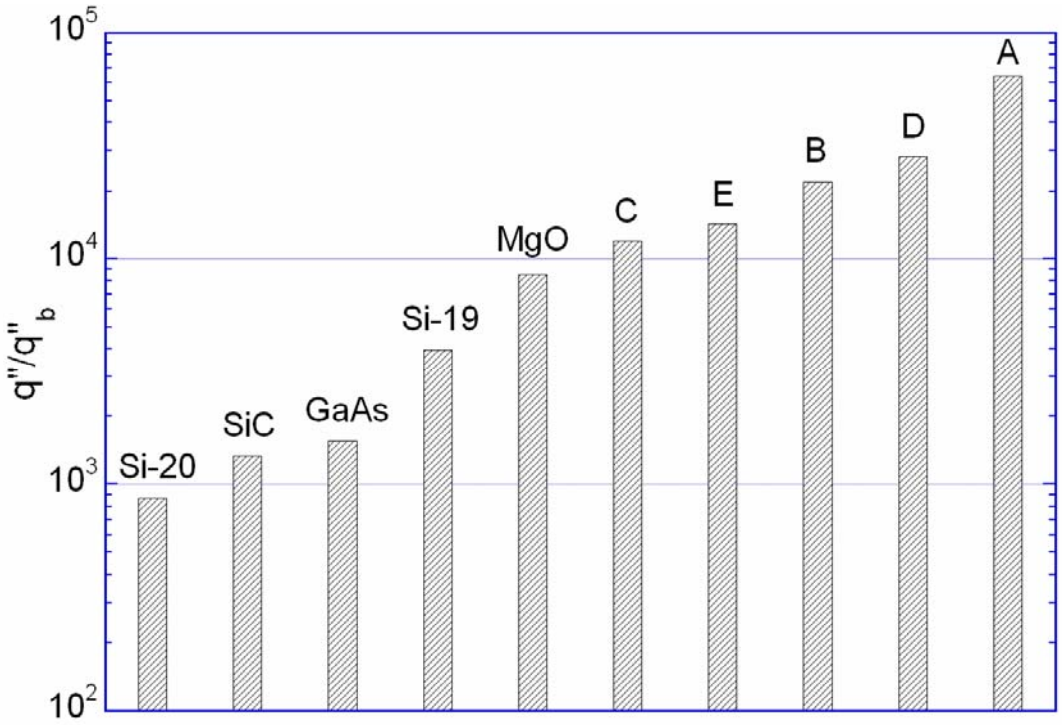

Figure 6.11 Comparison of the near-field radiative transfer between different materials or sets at d = 10 nm with T_1 = 300 K and T_2 = 0 K.

An optimization of near-field radiation between two parallel plates is conducted using fluctuational electrodynamics by tailoring the parameters in the Drude and Lorentz model. The effect of different adjustable parameters on the radiative heat transfer is investigated and optimal sets of parameters that maximize the near-field heat transfer are determined. It is seen that the real and imaginary parts of the dielectric function determine the location and width of the spectral heat flux peak, respectively. A smaller ε_∞ will result in an ε' close to -1 over a larger spectral region and is desired for near-field enhancement. For the Drude model, with increasing temperature, $\omega_{\mathrm{p,opt}}$ increases while $\gamma_{\mathrm{opt}}/\omega_{\mathrm{p,opt}}$ remains constant for maximum radiative transfer. For the Lorentz

model, the maximum near-field heat flux monotonically decreases with increasing ω_0 for a given ε_∞. In other words, the Drude model $(\omega_0 = 0)$ when optimized provides the greatest near-field enhancement for any given ε_∞. The results from this study will facilitate material selections for measurements of near-field radiative transfer and for future applications in imaging, energy conversion, and nanofabrication.

CHAPTER 7

ULTRASMALL PENETRATION DEPTH AND ENERGY STREAMLINES IN NANOSCALE RADIATIVE TRANSFER

Following the discussion on the fundamentals of nanoscale thermal radiation in Chapter 4 and maximum achievable near-field heat transfer in Chapters 5 and 6, the unusual penetration depth and energy streamlines are analyzed in this chapter. In the first half of the chapter, the ultrasmall penetration depth is investigated for near-field thermal radiation. It is seen that in the near-field, the penetration depth can be of the same order as the vacuum gap which may result in a 10 nm thick SiC behaving as semi-infinite at 10 nm vacuum gap. In the second half of this chapter, energy streamlines in near-field radiation are revisited. Accurate analytical expressions are derived for streamlines in the emitter, vacuum gap, and the receiver. It is seen that the lateral shift of streamlines inside the emitter can be greater than the vacuum gap which disproves previous understanding of lateral shift based on the lateral displacement suffered by the streamline as it crosses the vacuum gap. Based on the ultrasmall penetration depth and the lateral shift of streamlines, it is possible to define the dimensions of the emitter and receiver required for the accurate measurement of near-field thermal radiation between two parallel plates.

7.1 Ultrasmall Penetration Depth

Traditionally, radiation penetration depth in a solid, also called skin depth or photon mean free path, is defined as (Siegel and Howell, 2002).

$$\delta_\lambda = \lambda / \left(4\pi\kappa\right) \tag{7.1}$$

It is a measure of how deep the incident radiation can penetrate into the medium. A film whose thickness is 5-10 times the skin depth can be treated as opaque in most applications. Throughout the ultraviolet to infrared region, δ_λ of a good conductor (such as Ag or Au) is usually small, in the order of 10 nm at room temperature. For an evanescent wave, such as that induced under the total internal reflectance setup when light is incident from an optically denser medium to a rarer medium, the skin depth may be defined according to the $1/e$ attenuation of the field as

$$\delta = 1/\mathrm{Im}(\gamma) \tag{7.2}$$

The electric and magnetic fields will decay exponentially and become negligible at a distance greater than about one wavelength. Hence, the skin depth is several tenths of a wavelength (Zhang, 2007).

Recently, some studies have shown that even with a thickness much smaller than the conventional penetration depth, a thin coating can effectively enhance near-field radiative transfer (Biehs, 2007; Francoeur *et al*., 2008; Fu and Tan, 2009). Biehs (2007) demonstrated that putting a thin metallic film on a dielectric substrate will improve the near-field heat transfer between two dielectrics due to excitation of surface plasmon polaritons in the metallic film. Francoeur *et al*. (2008) analyzed the near-field heat transfer between bulk SiC and another bulk dielectric, coated with a thin SiC film. The calculated energy transfer is enhanced by three times compared with that without the SiC film, due to surface phonon polaritons coupling inside the thin film. Recently, Fu and Tan (2009) studied the near-field heat transfer between two plane surfaces when one of the surfaces is coated with a dielectric film that supports surface phonon polaritons. They found that adding the dielectric coating can either diminish or enhance the energy transfer

depending on the radiative properties of the emitter and the receiver. In fact, in the near-field, the skin depth not only depends on the frequency, materials, and geometric arrangement, but also depends on the separation distance between the two media, in which thermal radiation is emitted and received. The underlying physics of such phenomenon is explained in this chapter by observing the influence of surface waves on the skin depth associated with nanoscale radiation.

Let us consider near-field heat transfer between two parallel plates as shown in Fig. 2.1. Here also, the emitter is maintained at 300 K while the receiver is at 0 K. As observed in Chapter 5, at very small vacuum gaps, photon tunneling is mainly through the region where $\beta >> \omega/c$ and $Z(\omega,\beta)$ can be approximated as

$$Z(\omega,\beta)=\frac{4\varepsilon''^2 e^{-2\beta d}}{\left|(\varepsilon+1)^2-(\varepsilon-1)^2 e^{-2\beta d}\right|^2} \tag{7.3}$$

Figure 7.1 plots $Z(\omega,\beta)$ versus the product of β and d at the corresponding ω_{m} for SiC and n-type doped Si with doping concentrations of 10^{19} cm^{-3} and 10^{20} cm^{-3}. There exists a sharp peak at large βd for SiC, while a broader peak exists for heavily doped Si; this is due to the large scattering rate as well as the resulting large values of ε'' about ω_{m} in the doped Si. A larger ε'' yields a broader peak in $Z(\omega,\beta)$ and a smaller value of $\beta_{\mathrm{m}} d$ (Basu and Zhang, 2009a). For very small gap, while ω_{m} remains constant as d decreases, the energy transfer is shifted towards larger β values, leading to greater near-field enhancement. For $\beta >> \sqrt{\varepsilon_j}\,\omega/c$, $\gamma \approx i\beta$ or $\mathrm{Im}(\gamma)\approx\beta$ in all the three media. This suggests that there exists an evanescent wave (in medium 3) whose amplitude decays according to $e^{-\beta(z-d)}$. Hence, the skin depth of the field becomes $\delta_{\mathrm{F}} \approx 1/\beta$ and the

power penetration depth becomes $\delta_P \approx 1/(2\beta)$. The parameters corresponding to Fig. 7.1 are tabulated in Table 7.1, where δ_P is calculated at β_m and normalized with respect to d. The classical penetration depth δ_λ is on the order of 1 μm, which has previously been thought as the skin depth in near-field radiation (Francoeur *et al*., 2008; Fu and Tan, 2009). If δ_P is used instead, as suggested by Park *et al*. (2008) the penetration depth for SiC with a 10 nm gap is less than 2 nm. For 10^{19} cm^{-3} doped Si, δ_P is around 170 nm when d = 10 nm.

One of the objectives of this study is to determine the minimum thickness of a film so that it can be considered opaque for nanoscale thermal radiation. Two questions still remain. (1) What is the skin depth in the emitter? Intuitively, since both forward and backward waves have to be considered, the skip depth in the emitter would be different

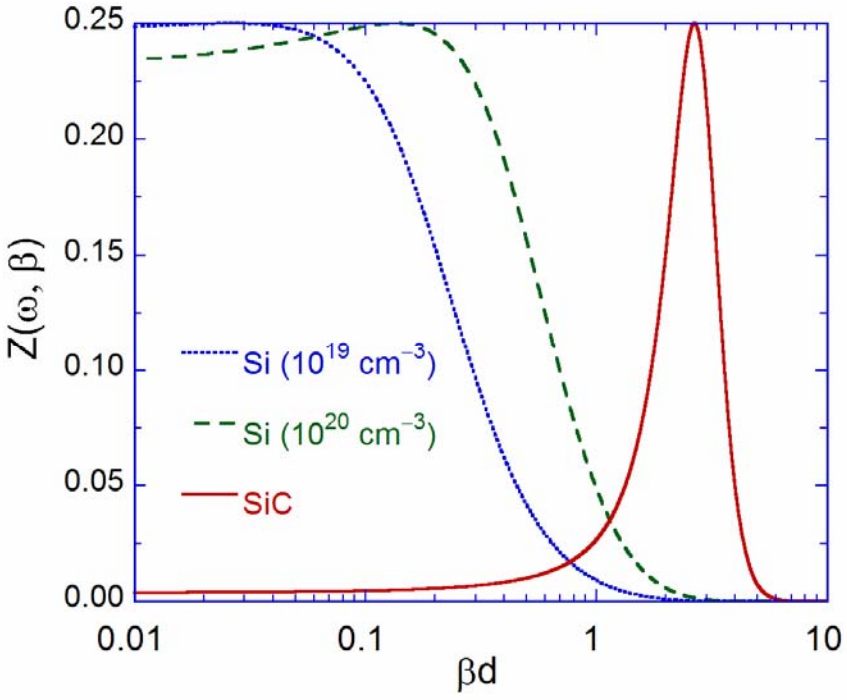

Figure 7.1 Graph of $Z(\omega,\beta)$ as a function of the product βd at the SPP resonance frequency (given in Table 1) for SiC and *n*-type Si

from that in the absorber. (2) What will be the penetration depth (or 1/*e* decay length) for the total heat flux? To answer these questions, the multilayer Green's function discussed by Park *et al*. (2008) is modified to allow the calculation of the *z*-component of the Poynting vector, which is proportional to the heat flux, both inside the emitter and the receiver. Following the approach adopted by Park *et al* (2008), the dyadic Green's function is

$$\bar{\bar{\mathbf{G}}}_{\mathrm{e}}(\mathbf{x},\mathbf{x}',\omega)=\frac{i}{4\pi}\int_0^{\infty}\frac{\beta d\beta}{\gamma_1}F(\beta,z,z')e^{i\beta(r-r')} \tag{7.3}$$

When $z>0$ (outside the emitter), the expression of F is straightforward since the integration over the source can be carried out over $-\infty<z'<0$. However, at a given depth z inside the emitter ($z<0$), different expressions must be used for the semi-infinite source below z ($-\infty<z'<z$) and for the finite layer source above z ($z<z'<0$). In other words, even though the source is homogeneous, one cannot use the conventional thin-film optics formulation with a forward and a backward wave to describe the electromagnetic field inside the emitter.

The spectral and total Poynting vector distributions are plotted in Fig. 7.2 for SiC and doped Si (10^{19} cm^{-3}). The ordinate is normalized to the Poynting vector inside the vacuum gap, which is a constant (no absorption). The energy flux increases in the emitter towards the surface, as more and more energy is emitted, and decreases in the receiver away from the surface. When the abscissa is z/d, the results are nearly the same for $1\text{ nm}<d<100\text{ nm}$. Surprisingly, the distributions are "symmetric" in the emitter and the receiver. It can be shown that the distribution function inside the receiver can be characterized by an exponential decay function $e^{-2\beta(z-d)}$. However, the distribution

function inside the emitter cannot be expressed as simply proportional to $e^{2\beta z}$ because of the complicated coefficients and number of terms involved.

The 1/*e* decay line is shown as the horizontal dashed line so that the penetration depth can be easily assessed from these curves. Note that the calculated Poynting vector is integrated over all β values. As mentioned earlier, when SPP is excited, the energy transfer is pushed towards large β values; hence, the spectral penetration depth has a minimum near ω_{m}. The actual minimum depends on the integration of $Z(\omega,\beta)\beta$. It should be mentioned that δ_{P} cannot be arbitrarily small. Therefore, when d is comparable to or less than the interatomic distance, the radiative transfer cannot be explained by the local electromagnetic theory.

For SiC as shown in Fig. 7.2 (a), the penetration depth is approximately 0.19*d* at 10.54 μm, where SPP is excited. The actual minimum penetration depth is located at 10.47 μm, corresponding to the maximum of $X(\omega)$. The penetration depth increases towards longer or shorter wavelengths, and the overall penetration depth based on the total energy flux is 0.25*d*, which is about 30% greater than δ_{P} evaluated at ω_{m} and β_{m} as shown in Table 1. For a thin vacuum gap, the SSP dispersion is shifted to large β values, resulting in a shorter penetration depth. Hence, a 10-nm coating of SiC can act as an optically thick medium when d = 10 nm as predicted by previous researchers (Biehs, 2007; Francoeur *et al*., 2008; Fu and Tan, 2009). When d < 1 nm, the penetration depth is less than a monolayer, implying that the SiC emitter is completely a 2D solid. Obviously, in such case, one cannot use its bulk dielectric function and also cannot set β_c as infinity.

From Fig. 7.2(b), the penetration depth for doped Si at SPP resonance frequency

is 0.9d, which is much less than the corresponding δ_{P} in Table 4. This can be explained with the help of Fig. 7.1 by observing that a significant portion of $Z(\omega,\beta)$ lies beyond β_{m}. Furthermore, for energy transfer, the integrand in Eq. (5.2) is not $Z(\omega,\beta)$ but $Z(\omega,\beta)\beta$. The spectral penetration depth is the smallest at $\lambda = 25.0\ \mu\mathrm{m}$ with a value of 0.85d. The overall penetration depth is 1.1d, which is 4.4 times that of SiC. As mentioned earlier, this is due to the large scattering rate (of doped Si), which causes a broad peak in the spectral heat flux q''_{ω}. Based on the total energy flux, a 5-nm doped-Si coating can be treated as essentially opaque for near-field thermal radiation with d = 1 nm (Basu and Zhang, 2009b). It should also be noted that nanoscale radiation is mostly enhanced when the emitter and the receiver are of same material, because this allows the excitation of SPPs at the same frequency. As mentioned before, the near-field heat transfer between SiC plates is on the same order as that between doped Si. Based on Fig. 7.2 it can be inferred that compared to doped Si, a smaller volume of SiC material can be used as the emitter due to the smaller penetration depth in the later.

Table 7.1 Parameters at the SPP resonance frequency and the corresponding penetration depths. Note that $\delta_{\lambda} = \lambda/(4\pi\kappa)$ and $\delta_{\mathrm{P}} = 1/(2\beta_{\mathrm{m}})$.

Material	ω_{m} (rad/s)	ε'	ε''	δ_{λ} (μm)	$\beta_{\mathrm{m}}d$	δ_{P}/d
Si (10^{19} cm^{-3})	7.15×10^{13}	−1.08	8.84	0.94	0.03	16.67
Si (10^{20} cm^{-3})	2.61×10^{14}	−1.01	3.61	0.36	0.14	3.57
SiC	1.79×10^{14}	−1.06	0.13	0.80	2.67	0.19

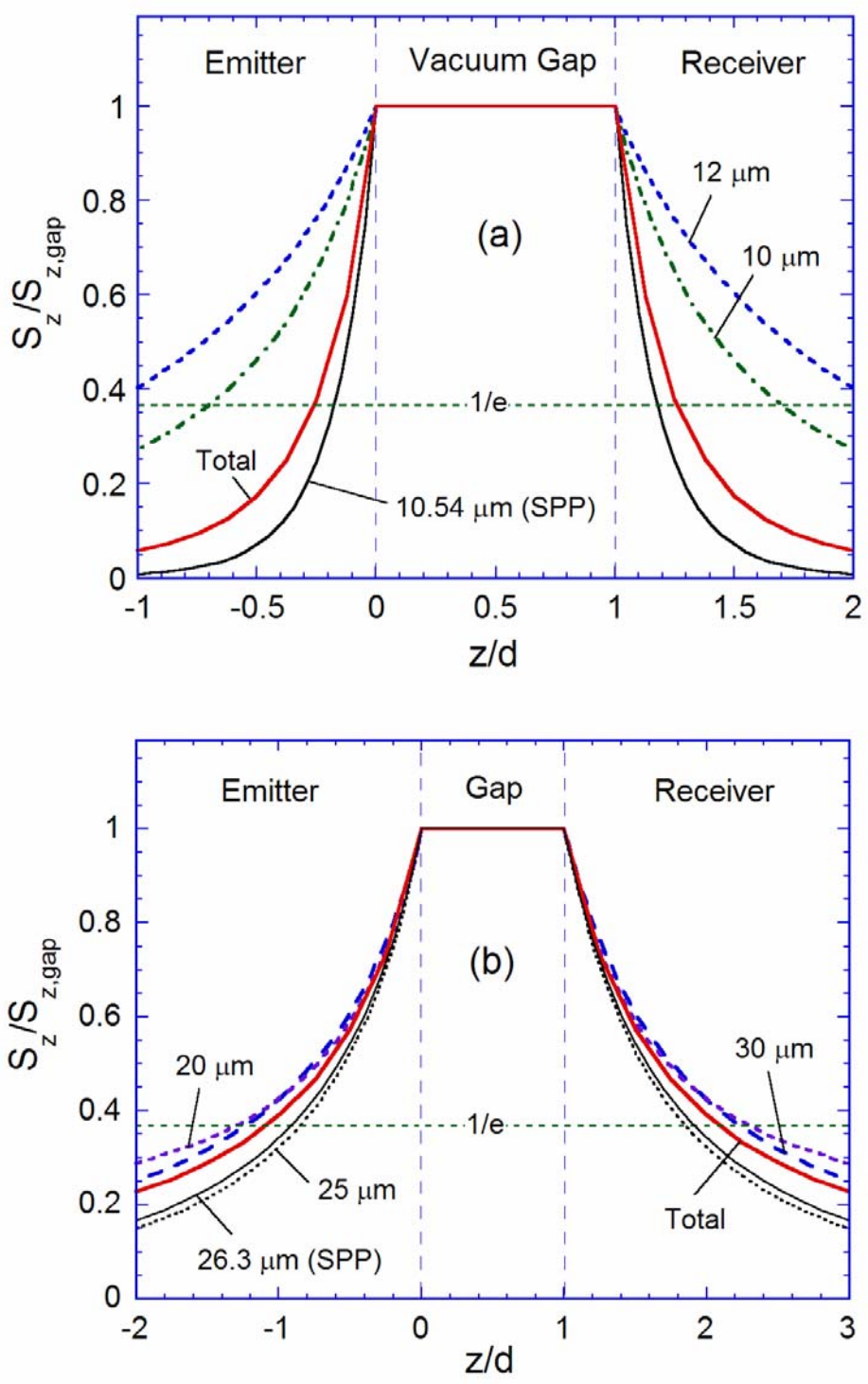

Figure 7.2 The distributions of the spectral and total Poynting vector (z component) near the surfaces of the emitter and receiver normalized to that in the vacuum: (a) SiC; (b) 10^{19} cm^{-3} doped Si. The wavelength corresponding to the resonance frequency listed in Table 4 is also indicated.

7.2 Energy Streamlines in Near-field Radiation

In addition to the calculation of near-field energy transfer between the two media, it is important to understand the direction of energy flow between them in order to facilitate the different applications of near-field radiation. Unlike classical radiative heat transfer, the direction of energy propagation in nanoscale radiation cannot be determined using ray optics since the refraction angle is not defined in real space during photon tunneling (Lee *et al.,* 2007). While the near-field energy transfer between two surfaces has been calculated as well as measured by researchers, there have been only a few studies which have investigated the energy propagation direction as well as the associated lateral shifts.

Zhang and Lee (2006) determined the direction of energy propagation during photon tunneling by tracing the Poynting vector at fixed β values. Lee *et al* (2007) demonstrated that the Poynting vector is decoupled between different parallel wavevector components due to the randomness of thermal radiation. This finding enables one to calculate the energy streamlines (ESL) by tracing the Poynting vector at different β values. The concept of ESL is analogous to streamlines in fluid flow and was used by Lee *et al* (2007) to determine energy pathways in near-field radiation for the first time. Recently, Lee and Zhang (2008) calculated the energy streamlines as well as lateral shift for various β values between two SiC plates when SPP are excited.

However, all the previous studies used simple thin-film optics to calculate the energy pathways without considering the fundamentals of thermal emission inside the emitter. Besides, in these studies (Lee *et al*., 2007; Lee and Zhang, 2008) the lateral shift has been defined as the lateral displacement suffered by the energy streamlines as they

reach the receiver surface after crossing the vacuum gap. Such a definition of lateral shift is questionable since the streamlines were not traced inside the emitter and the receiver.

In this section, the issue of energy streamlines in near-field is revisited. Analytical expressions for streamlines inside the emitter, receiver and the vacuum gap are derived based on fluctutation electrodynamics. Differences in the streamlines calculated by adopting the thin-film approach employed by Lee *et al* (2007) and fluctuation electrodynamics are presented. The influence of surface waves on ESL is also investigated. For convenience, the receiver is maintained at 0 K implying that thermal emission takes place only from the emitter. In order to calculate the energy stream lines it is important to calculate the r and z components of the Poynting vector in the three media.

7.2.1 Theoretical Formulation

In order to plot the streamlines in the emitter, receiver, the vacuum gap we need to find the Poynting vectors in the different media which requires obtaining the Green's functions inside the three media. As mentioned in Chapter 2, the Green's function is a spatial transfer function which provides the field due to a point source.

In order to accurately determine the Green's function inside the emitter we need to correctly account for the direction of the emitted and reflected waves. Figure 7.3 shows a schematic of near-field heat transfer between two parallel plates separated by vacuum gap along with the different energy flow directions inside the emitter. Inside the emitter, at a given depth z, there are contributions from (i) upward waves from all planes $z' < z$, (ii) directly generated downward waves from planes $z' > z$, and (iii) downward wave

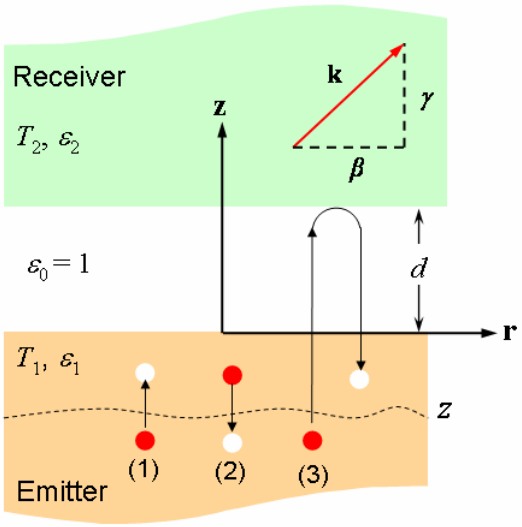

Figure 7.3 Schematic of near-field heat transfer between two parallel plates (1 and 2) showing the different modes of energy propagation inside the emitter. Note that the white dots refer to the detector and red dot refers to the source. The different energy propagation modes have been indicated as numbers in the figure.

from all the upward waves suffering reflection at the interfaces of media 1 and 2 and vacuum gap. These are indicated in Fig. 7.3. Accordingly, the electric Green's function inside the emitter can be expressed as

$$\bar{\bar{\mathbf{G}}}_{\mathrm{e}}(\mathbf{x},\mathbf{x}',\omega) = \bar{\bar{\mathbf{G}}}_{\mathrm{e,p}}(\mathbf{x},\mathbf{x}',\omega) + \bar{\bar{\mathbf{G}}}_{\mathrm{e,r}}(\mathbf{x},\mathbf{x}',\omega) \tag{7.5}$$

where $\bar{\bar{\mathbf{G}}}_{\mathrm{e,p}}(\mathbf{x},\mathbf{x}',\omega)$ is for the wave propagation in an isotropic, homogenous, unbounded media with delta source at $\mathbf{x}'$ and $\bar{\bar{\mathbf{G}}}_{\mathrm{e,r}}(\mathbf{x},\mathbf{x}',\omega)$ is the response due to the layered media above the emitter. In other words, $\bar{\bar{\mathbf{G}}}_{\mathrm{e,p}}(\mathbf{x},\mathbf{x}',\omega)$ accounts for the energy propagation due to modes (1) and (2) in Fig. 7.3 while $\bar{\bar{\mathbf{G}}}_{\mathrm{e,r}}(\mathbf{x},\mathbf{x}',\omega)$ accounts for (3). The two different Green's functions are given by Sipe (1987) and Tsang *et al* (2000)

$$\bar{\bar{\mathbf{G}}}_{\mathrm{e,p}}(\mathbf{x},\mathbf{x}',\omega) = \frac{\mathrm{i}}{4\pi}\int_0^{\infty} \frac{\beta \mathrm{d}\beta}{\gamma_1} \times F(\beta) e^{\mathrm{i}\beta(r-r')} \tag{7.6}$$

where
$$F(\beta)=\begin{cases}\left(\hat{\mathbf{e}}_{\mathrm{s}}^{+}\hat{\mathbf{e}}_{\mathrm{s}}^{+}+\hat{\mathbf{h}}_{\mathrm{s}}^{+}\hat{\mathbf{h}}_{\mathrm{s}}^{+}\right)\mathrm{e}^{\mathrm{i}\gamma_1(z-z')}, & z>z'\\ \left(\hat{\mathbf{e}}_{\mathrm{s}}^{-}\hat{\mathbf{e}}_{\mathrm{s}}^{-}+\hat{\mathbf{h}}_{\mathrm{s}}^{-}\hat{\mathbf{h}}_{\mathrm{s}}^{-}\right)\mathrm{e}^{-\mathrm{i}\gamma_1(z-z')}, & z<z'\end{cases} \tag{7.7}$$

and
$$\bar{\bar{\mathbf{G}}}_{\mathrm{e,r}}(\mathbf{x},\mathbf{x}',\omega)=\frac{\mathrm{i}}{4\pi}\int_0^{\infty}\frac{\beta\mathrm{d}\beta}{\gamma_1}\left(\hat{\mathbf{e}}_{\mathrm{s}}^{-}r^{\mathrm{s}}\hat{\mathbf{e}}_{\mathrm{s}}^{+}+\hat{\mathbf{h}}_{\mathrm{s}}^{-}r^{\mathrm{p}}\hat{\mathbf{h}}_{\mathrm{s}}^{+}\right)\mathrm{e}^{-\mathrm{i}\gamma_1(z+z')}e^{\mathrm{i}\beta(r-r')} \tag{7.8}$$

Here, the unit vectors for the polarization states are defined by $\hat{\mathbf{e}}_{\mathrm{s}}^{+}=\hat{\mathbf{e}}_{\mathrm{s}}^{-}=\hat{\mathbf{r}}\times\hat{\mathbf{z}}$ and $\hat{\mathbf{h}}_{\mathrm{s}}^{\pm}=(\beta\hat{\mathbf{z}}\mp\gamma_1\hat{\mathbf{r}})/k_1$ with $k_1=\varepsilon_1\omega/c$. Notice that z' and z denote the location of the source and the detector respectively. For Eq. (7.8), note that $\hat{\mathbf{h}}^{+}$ and $\hat{\mathbf{e}}^{+}$ change to $\hat{\mathbf{h}}^{-}$ and $\hat{\mathbf{e}}^{-}$ on reflection, and $\mathrm{e}^{-\mathrm{i}\gamma_1(z+z')}=\mathrm{e}^{-\mathrm{i}\gamma_1(z-0)}\cdot\mathrm{e}^{\mathrm{i}\gamma_1(0-z')}$. r^{s} and r^{p} refer to reflection coefficients for TE and TM waves respectively including multiple reflections in the vacuum gap and are obtained using Fresnel coefficients (Zhang, 2007). From Maxwell's equation, the magnetic Green's function can be expressed as,

$$\bar{\bar{\mathbf{G}}}_{\mathrm{m}}(\mathbf{x},\mathbf{x}',\omega)=\nabla\times\bar{\bar{\mathbf{G}}}_{\mathrm{e}}(\mathbf{x},\mathbf{x}',\omega) \tag{7.9}$$

Similar to the electric Green's function, the magnetic Green's function can also be split in to two parts based on the different modes of energy propagation. Hence,

$$\bar{\bar{\mathbf{G}}}_{\mathrm{m,p}}(\mathbf{x},\mathbf{x}',\omega)=\frac{\mathrm{i}}{4\pi}\int_0^{\infty}\frac{\beta\mathrm{d}\beta}{\gamma_1}\times F_1(\beta)e^{\mathrm{i}\beta(r-r')} \tag{7.10}$$

where
$$F_1(\beta)=\begin{cases}\left[\left(\gamma_1\hat{\mathbf{r}}-\beta\hat{\mathbf{z}}\right)\hat{\mathbf{s}}+\hat{\mathbf{s}}\left(\beta\hat{\mathbf{z}}-\gamma_1\hat{\mathbf{r}}\right)\right]\mathrm{e}^{\mathrm{i}\gamma_1(z-z')}, & z>z'\\ \left[\left(\gamma_1\hat{\mathbf{r}}-\beta\hat{\mathbf{z}}\right)\hat{\mathbf{s}}+\hat{\mathbf{s}}\left(\beta\hat{\mathbf{z}}-\gamma_1\hat{\mathbf{r}}\right)\right]\mathrm{e}^{-\mathrm{i}\gamma_1(z-z')}, & z<z'\end{cases} \tag{7.11}$$

$$\bar{\bar{\mathbf{G}}}_{\mathrm{m,r}}(\mathbf{x},\mathbf{x}',\omega)=\frac{\mathrm{i}}{4\pi}\int_0^{\infty}\frac{\left(\beta\hat{\mathbf{r}}-\gamma_1\hat{\mathbf{z}}\right)}{\gamma_1}\left[r^{\mathrm{s}}\hat{\mathbf{s}}\hat{\mathbf{s}}+\left(\frac{\beta\hat{\mathbf{z}}+\gamma_{\mathrm{s}}\hat{\mathbf{r}}}{k_1}\right).\left(\frac{\beta\hat{\mathbf{z}}-\gamma_{\mathrm{s}}\hat{\mathbf{r}}}{k_1}\right)r^{\mathrm{p}}\right]\mathrm{e}^{-\mathrm{i}\gamma_1(z+z')}e^{\mathrm{i}\beta(r-r')}\beta\mathrm{d}\beta \tag{7.12}$$

Once the electric and magnetic Green's functions are obtained, the corresponding electric and magnetic fields are given by the following,

$$\mathbf{E}(\mathbf{x},\omega) = i\omega\mu_0 \int_{V'} \overline{\overline{\mathbf{G}}}_{\mathrm{e}}(\mathbf{x},\mathbf{x}',\omega)\mathbf{j}(\mathbf{x}',\omega)\, d^3\mathbf{x}' \tag{7.13}$$

and

$$\mathbf{H}(\mathbf{x},\omega) = \int_{V'} \overline{\overline{\mathbf{G}}}_{\mathrm{m}}(\mathbf{x},\mathbf{x}',\omega)\mathbf{j}(\mathbf{x}',\omega)\, d^3\mathbf{x}' \tag{7.14}$$

The electric and magnetic fields in the vacuum gap and the receiver can be obtained using the Green's functions reported by Lee and Zhang (2008) and Fu and Zhang (2006) respectively. The Poynting vectors in *r*- and *z*- directions can then be calculated by using Eq. (2.3) and invoking the fluctuation dissipation theorem. Note that for convenience, cylindrical coordinate system is used for calculation of the Poynting vector. After simplification, the Poynting vectors in *r* and *z*- directions can be expressed as

$$S_r\left(z,\omega\right) = \frac{\Theta(\omega,T_1)}{4\pi^2}\int_0^\infty A\left(z,\omega,\beta\right)\beta \mathrm{d}\beta \tag{7.15}$$

and

$$S_z\left(z,\omega\right) = \frac{\Theta(\omega,T_1)}{4\pi^2}\int_0^\infty B\left(z,\omega,\beta\right)\beta \mathrm{d}\beta \tag{7.16}$$

where the functions $A\left(z,\omega,\beta\right)$ and $B\left(z,\omega,\beta\right)$ take different forms in the different media. If both the emitter and the receiver are made of the same material then the expression for $B\left(z,\omega,\beta\right)$ in the emitter is same as that in the receiver which results in $S_z\left(z,\omega\right)$ inside the emitter being identical to that in the receiver as seen in Fig. 7.2. Since the Poynting vector is decoupled for each β, it is possible to plot the streamlines at different β values. Once, S_z and S_r can be defined, the energy propagation angle can be obtained as

$$\theta\left(\omega,\beta,z\right) = \tan^{-1}\left(\frac{S_z(\omega,\beta,z)}{S_r(\omega,\beta,z)}\right) \tag{7.17}$$

In the next subsection, ESL are plotted for SiC and doped Si.

7.2.2 Results and Discussions

To start with, ESL computed with the help fluctuation electrodynamics is compared with that calculated using the thin film optics used by Lee *et al* (2007). Figure 7.4 plots the energy streamlines using the two different approaches inside the emitter, vacuum gap, and the receiver when the material of both the emitter and the receiver is taken to be SiC. The streamlines are plotted at ω_{m} for propagating waves $\left(\beta = 0.5\omega/c\right)$ in Fig. 7.4(a) and for evanescent waves $\left(\beta = 50\omega/c\right)$ in 7.4(b). In both cases the vacuum gap is set to 100 nm and the streamlines are plotted for TM waves only. Inside the emitter, the streamlines calculated using thin film optics and FE are identical for propagating waves. However, for evanescent waves, the streamline calculated using FE decays much faster as compared to thin film optics.

While using thin film optics to calculate the streamlines, Lee *et al* (2007) have neglected the emission from the source when it is located above the detector. In other words, they have neglected the energy propagation mode denoted by (2) in Fig. 7.3. For propagating waves, the penetration depth is very large, on the order of few microns and very little energy is absorbed close to the surface of the emitter. Hence, contribution to the total emission from source when it is above the detector is negligible at a depth of 100 nm. Consequently, streamlines calculated using thin film optics and FE are very similar for propagating waves. On the other hand, for evanescent waves the skin depth of thermal radiation is inversely proportional to β and is of the same order as the vacuum gaps for very large β as seen from section 7.1. This implies that thermally emitted waves from sources located deeper than the ultrasmall skin depth cannot reach the surface. Therefore, for evanescent waves, the source contributes predominantly to the thermal emission when

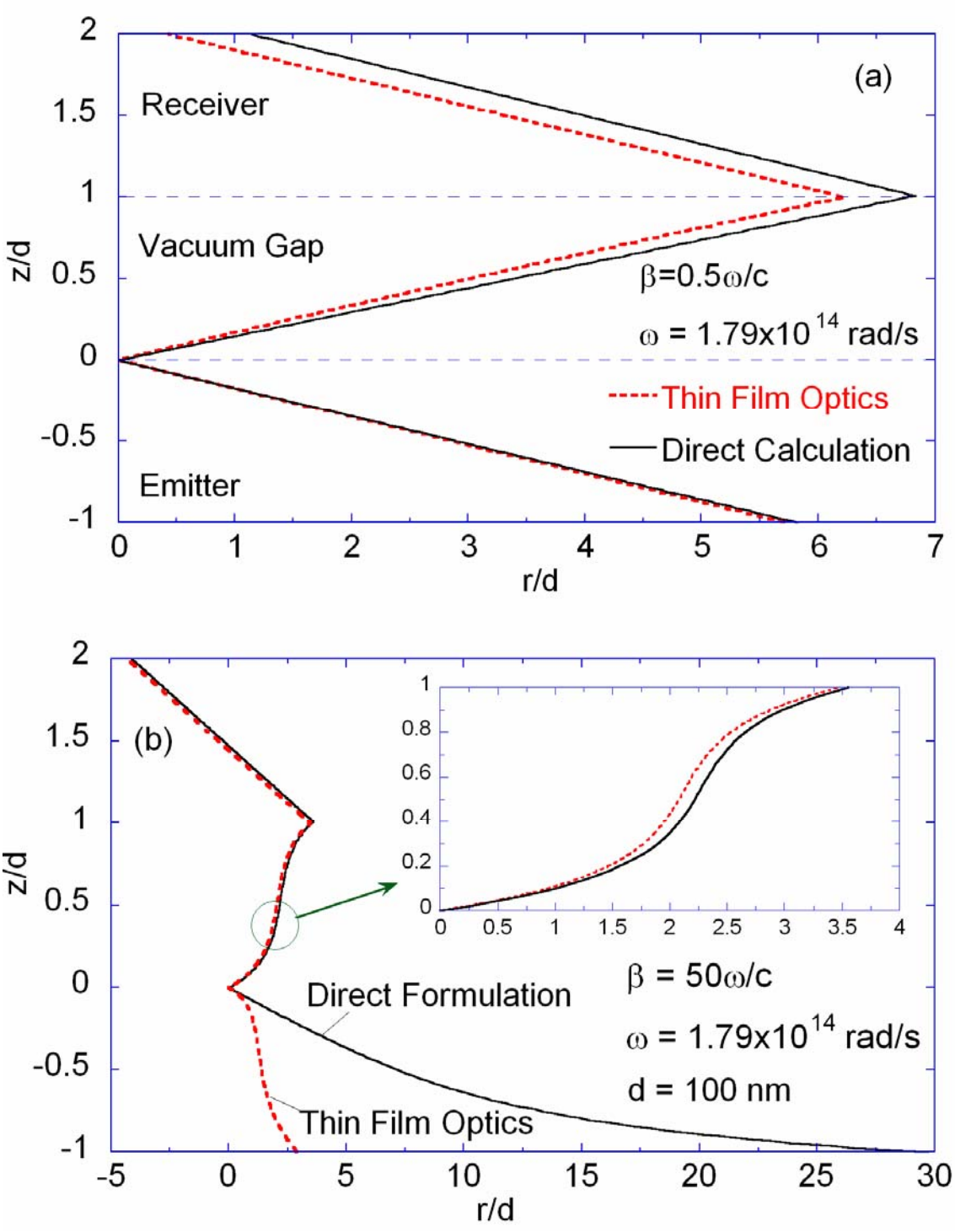

Figure 7.4 Comparison of energy streamlines calculated using thin film optics and fluctuational electrodynamics in SiC for (a) propagating waves and (b) evanescent waves.

it is located above the detector. The simple thin film optics formulation fails to capture this phenomenon and incorrectly predicts the streamlines inside the emitter. Since only medium 1 is emitting, the streamlines calculated using FE and thin film optics are almost identical inside the vacuum gap and the receiver. The small difference is due to the wrong calculation of coefficients for the electric and magnetic field inside the vacuum gap and the receiver while using thin film optics.

Figure 7.5 shows the energy streamlines calculated for different β^* values when the emitter and the receiver are considered to be of SiC. The streamlines are plotted at ω_{m} of SiC for propagating and evanescent waves in Figs 7.5(a) and (b) respectively and $\beta^* = \beta c/\omega_{\mathrm{m}}$. Both the vertical and horizontal axes are normalized with respect to the vacuum gap which is set to 10 nm and all the streamlines pass through the origin. Notice that for propagating waves, the energy streamlines in the vacuum gap are not exactly straight lines due to interference. As discussed by Lee *et al* (2007), for propagating waves all the streamlines are bounded within the conical surfaces bounded by the ESL at $\beta = \omega/c$. It can be seen that negative refraction occurs at both the interfaces of SiC and vacuum gap due to opposite sign of their dielectric functions when surface waves are excited.

Compared to propagating waves, the streamlines inside the emitter and the vacuum gap are much more curved for evanescent waves due to stronger coupling of evanescent waves. The streamlines in the receiver are straight lines since it is assumed to be semi-infinite and no backward waves exist. Besides, the receiver is considered to be non-emitting. It must be mentioned that and Lee and Zhang (2008) calculated the streamlines only inside the vacuum gap and hence considered the lateral shift suffered by

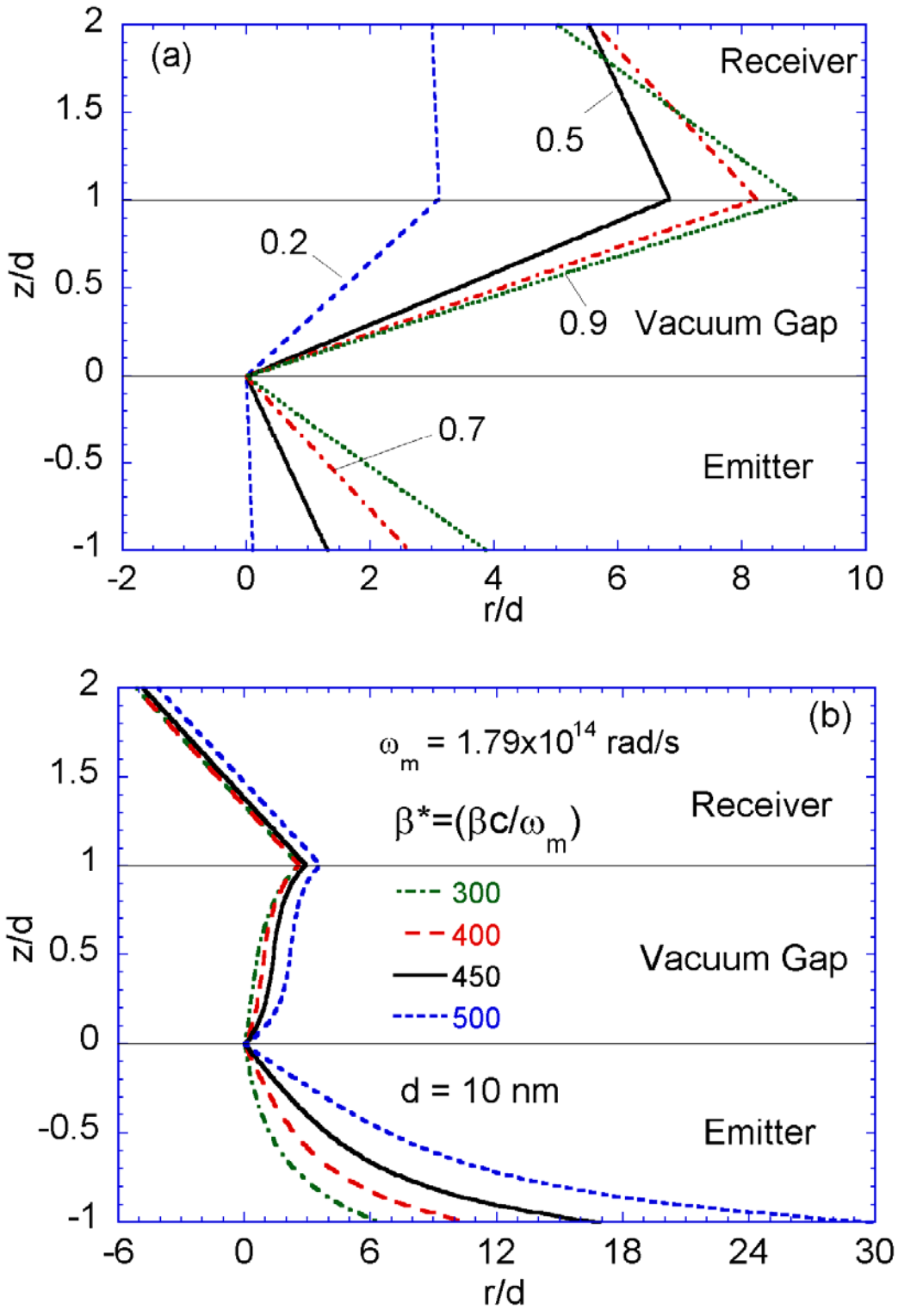

Figure 7.5 The calculated energy streamlines inside the emitter, receiver, and the vacuum gap for SiC at SPP resonance when d = 10 nm for (a) propagating waves and (b) evanescent waves.

the ESL in the vacuum gap as the only guiding parameter for the design of energy conversion devices. Based on Fig. 7.5(b), it can be seen that such type of assumption is incorrect since the lateral shift of the streamlines is largest inside the emitter. Besides, compared to the vacuum gap the lateral shift inside the emitter is a stronger function of β^*. This will be discussed in greater details later. Notice that $\beta^* = 450$ corresponds to the maximum of $Z(\omega_{\mathrm{m}}, \beta)$ curve and will be referred to as β^*_{m}.

In Figure 7.6 the energy streamlines are plotted for 10^{19} cm^{-3} doped Si at corresponding ω_{m} values. For evanescent waves, when SPP are excited, the slope of the streamlines in the receiver is equal to $(\varepsilon'/\varepsilon'')$. Hence the slope of the streamlines in the receiver for evanescent waves in case of doped Si is much smaller as compared to that for SiC. It can be seen from Fig. 7.6(a) that the ESL inside the emitter for different β^* are nearly identical. Note that the amplitude of the waves inside the emitter decays as $e^{-2\,\mathrm{Im}(\gamma_1)z}$. For doped Si, at SPP resonance $\varepsilon = -1.08 + 8.84\mathrm{i}$. As a result for $\beta^* < 1$, $\mathrm{Im}(\gamma_1)$ does not change much which results in the streamlines being identical. As seen from Fig. 7.6(b), the lateral shift of the streamline inside the emitter is smaller than that in the vacuum gap. This is opposite to that observed in case of SiC. While the lateral shift in the vacuum gap for both SiC and doped Si are comparable, the ESL inside the emitter decays much faster inside the emitter for SiC resulting in a larger lateral spread. $Z(\omega_{\mathrm{m}}, \beta)$ for doped Si is maximum at $\beta^* = 11.2$. As seen from Fig. 7.1, a large scattering rate of doped Si results in a broader peak of $Z(\omega_{\mathrm{m}}, \beta)$ than that for SiC which causes the maximum value of β^* to be much smaller for the former.

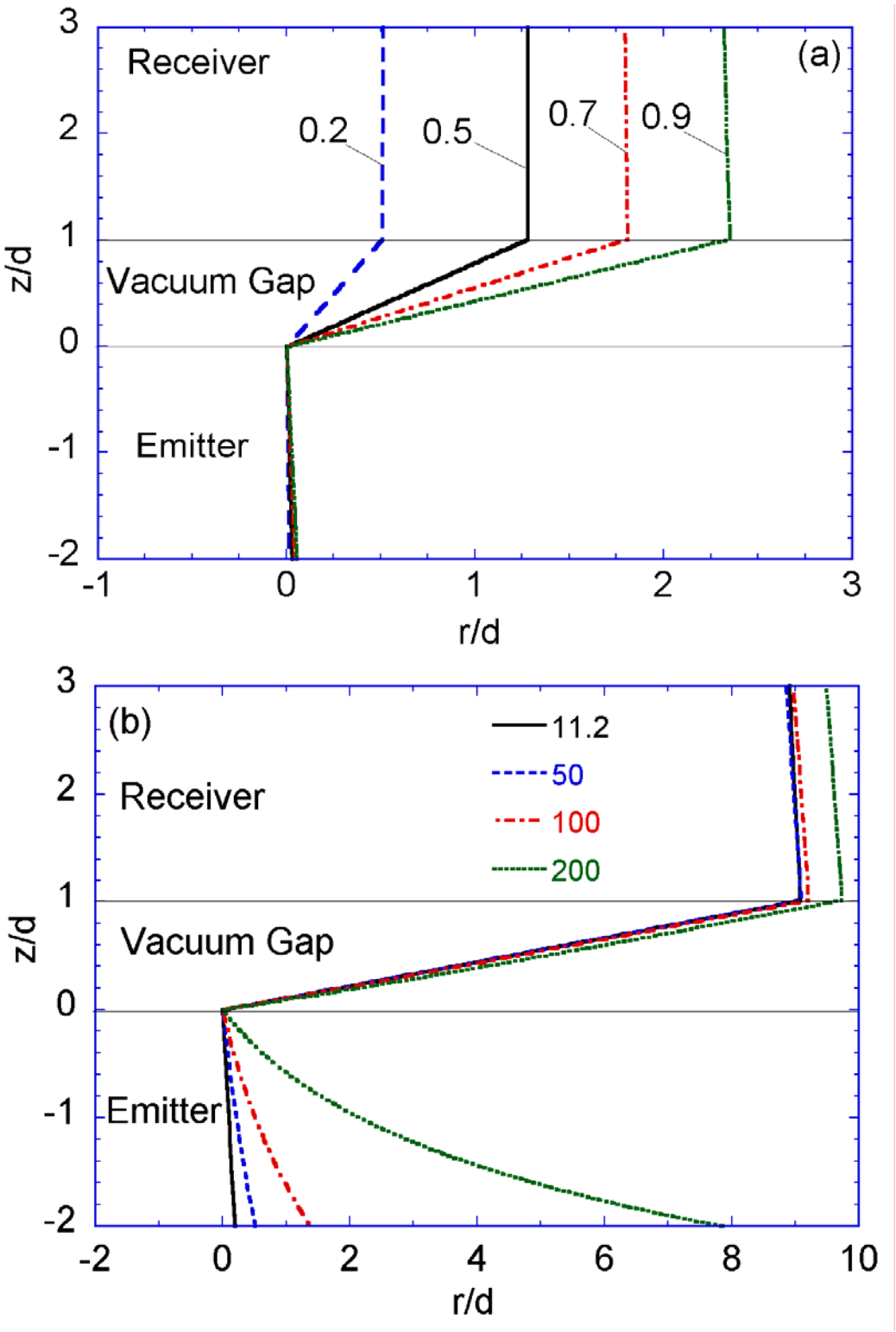

Figure 7.6 Plot of energy streamlines for 10^{19} cm^{-3} *n*-type Si for (a) propagating waves and (b) evanescent waves when *d*=10 nm.

Figures 7.7 (a) and (b) plot the *z*- component of the spectral Poynting vector inside the emitter, receiver, and the vacuum gap for SiC and 10^{19} cm^{-3} doped Si respectively at different β^*. As in Fig. 7.3, the ordinate is normalized with respect to the Poynting vector inside the vacuum gap and the 1/*e* decay line is shown to indicate the penetration depth. Note that the spectral Poynting vector obtained after integration over all the β values is also plotted and is indicated as "*total*" in the figures. For SiC, the field obtained after integration over all the β is identical with that at β_{m}^*. However, for doped Si, the two fields are very different. Due to a smaller scattering rate, $Z(\omega_{\mathrm{m}}, \beta)$ has a very sharp peak at β_{m}^* which results in the two fields being identical. For doped Si, a significant portion of $Z(\omega_{\mathrm{m}}, \beta)$ lies beyond β_{m}^* causing the two fields to be different. Also, from Fig. 7.2, $Z(\omega_{\mathrm{m}}, \beta)$ for doped Si peaks at a much smaller β_{m}^* value compared to that for SiC. As a result, the field decays much faster for SiC.

Interestingly, the shape of ESLs inside the emitter for both doped Si and SiC can be explained with the help of Fig. 7.7. The field decreases faster as β^* increases and the decay is much faster for evanescent waves. This is expected since the amplitude of the field is proportional to $e^{-2\beta z}$ for evanescent waves and most of the energy is absorbed close to the surface of the emitter. As a result, from Eq. (7.15), the slope of the streamlines decreases as β^* increases. The thin film optics approach which does not correctly account for emission inside the emitter cannot predict the exponential decay of the Poynting vector. Furthermore, for SiC, if we consider the total energy to be absorbed within $4\delta_{\mathrm{P}}$, the lateral dimension of the emitter should be around 9*d*.

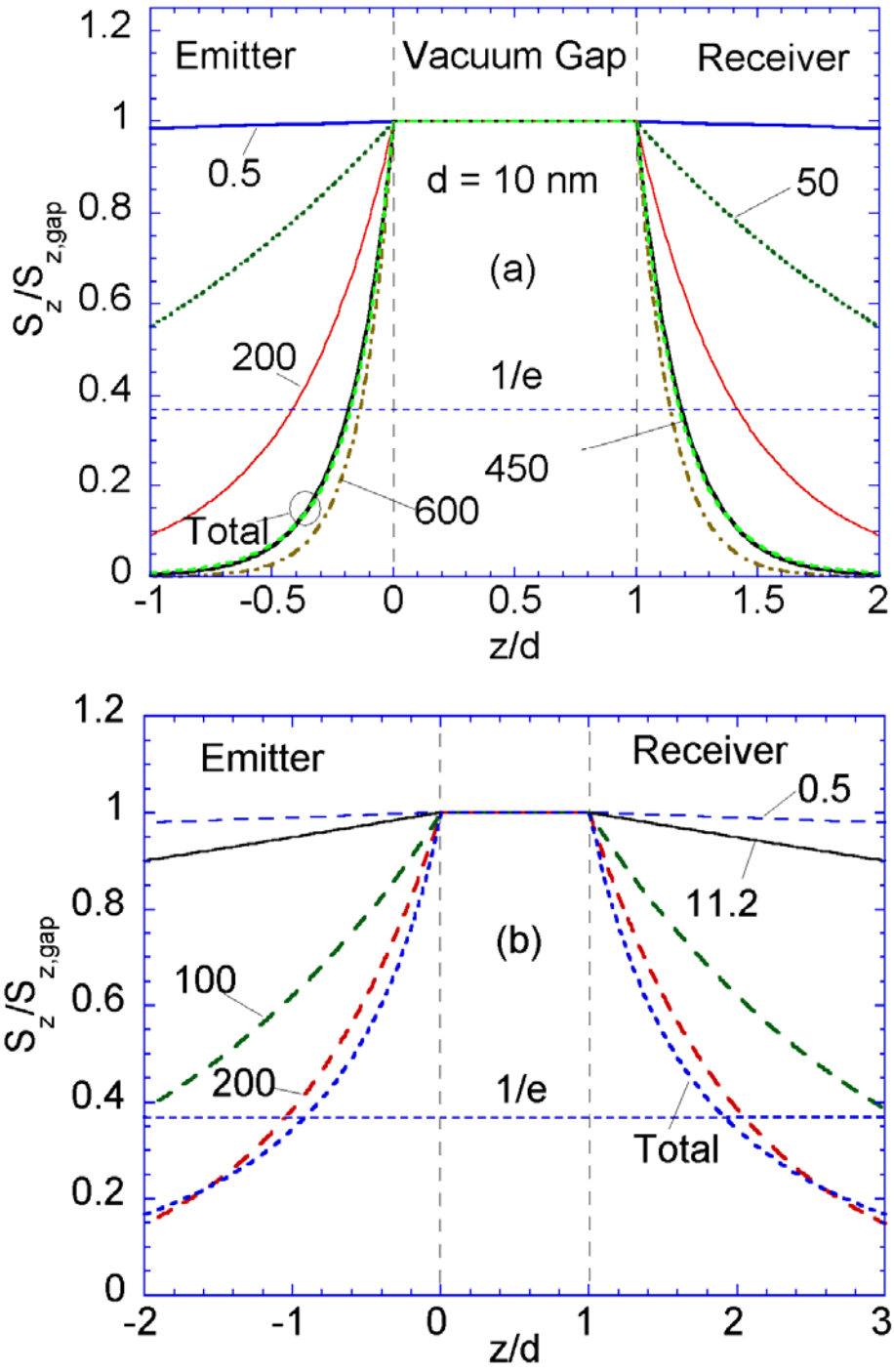

Figure 7.7 Distributions of the spectral Poynting vector (z component) near the surfaces of emitter, receiver and the vacuum gap for (a) SiC and (b) 10^{19} cm^{-3} doped Si for different β^*. The Poynting vector calculated after integration over all β values is indicated as "*total*" in the figures.

In summary, the unusual penetration depth and the energy streamlines in near-field thermal radiation are investigated in this chapter. The skin depth in near-field thermal radiation is a function of the vacuum gap as well as material properties. Even a 1-nm-thick SiC film or a 5-nm-thick doped Si can act as an opaque layer if the gap width is at 1 nm. This unusual feature associated with nanoscale radiation arises from the excitation of surface waves. On the other hand, it is shown in this study that the thin film optics cannot be used to correctly predict the streamlines in near-field radiation. The emission as well as the direction of propagation of the waves inside the different media must be correctly accounted for in calculating the streamlines. Using fluctuation electrodynamics, analytical expressions are obtained for the field as well as the streamlines inside the emitter, vacuum gap, and the receiver. The lateral shift of streamlines in the emitter can be much greater than that in the vacuum gap for SiC. Based on the lateral shift and the penetration depth it is possible to correctly estimate the size of the emitter for it to be considered semi-infinite during near-field heat transfer. The insight obtained from this study can facilitate the selection of coating materials and thicknesses for scanning-tunneling near-field thermal imaging and nanofabrication.

CHAPTER 8

CONCLUSION AND RECOMMENDATIONS

This dissertation investigates the near-field heat transfer between two parallel plates at nanometer distances. Initially, an improved dielectric function of doped Si is developed after a careful review of different carrier ionization and mobility models. Drude model is employed for modeling the dielectric function of doped Si based on the selected carrier mobility and ionization models. The doped Si samples were modeled as multilayer structure of heavily doped Si thin films deposited on a thick lightly doped Si substrate and the radiative properties were calculated using thin film optics. The ion-implanted doped Si samples were annealed in the RTA. The transmittance and reflectance of the annealed samples was measured up to a doping concentration of 10^{21} cm^{-3} in the wavelength region from 2 to 20 μm. The calculated results are in good agreement with the measurement, suggesting that the Drude model developed is appropriate in predicting the radiative properties of heavily doped Si near room temperature.

In the next step, the near-field heat transfer between doped Si plates with different doping levels using the improved dielectric function is studied. The influence of surface waves, doping level, vacuum gap, and different polarizations on the total and spectral heat transfer is investigated. By varying the doping level, the radiative properties of doped Si can be changed which results in different near-field effects at different doping levels. Interestingly, the near-field heat transfer is the least for 10^{21} cm^{-3} doped Si due to strong metallic behavior. Also, increase in doping level of Si increases the scattering rate which results in a smaller but broader peak of the spectral heat flux curve.

For doped Si, TM wave contribution is more significant till a doping level of 10^{20}cm^{-3} while for 10^{21}cm^{-3} doped Si, the TE wave is more dominant till around 30 nm. Interestingly, while the near-field heat transfer due to TM wave varies as d^{-2}, the TE wave contribution saturates in the near-field. Analytical expressions are provided for the LDOS in the vacuum gap when the effect of the receiver is considered. It is seen that the receiver tends to affect the LDOS only at distances around 0.6d.

The study on near-field heat transfer for doped Si raises an important question about the upper limit on the near-field radiative heat transfer. The question is two-fold (i) what is the upper limit of near-field heat transfer? and (ii) what should be the criterion to determine the maximum near-field energy flux? Previous studies have calculated the maximum possible heat transfer only when $d \to 0$ and cannot be looked upon as the maximum near-field heat transfer at finite separation distances. In this dissertation, the maximum achievable energy transfer in the near-field is investigated at finite separation distances by considering identical frequency independent dielectric functions for both the emitter and the receiver. An upper bound is imposed to the parallel wavevector component in the analysis based on fluctuation-dissipation theory. Due to the cutoff in the wavevector, the energy transfer deviates from the d^{-2} dependence at sub-nanometer distances. It is observed that the maximum enhancement occurs when ε' is around -1 which corresponds to SPP resonance. Furthermore, the maximum heat flux depends on the vacuum gap and ε'' value when ε' is set to -1. As ε'' decreases, the spectral heat flux curve peaks towards longer β values. Hence, setting a cutoff on the upper limit of β has a greater influence on the near-field heat transfer for materials with a smaller ε'' value.

The results obtained from the analysis of maximum near-field heat transfer helps in the parametric optimization of dielectric functions for determining the maximum achievable near-field heat transfer in real materials. The Drude model predicting the dielectric function of good conductors and the Lorentz model predicting the permittivity of dielectrics is considered for the optimization. The effect of different adjustable parameters in the two dielectric functions on the radiative heat transfer is investigated and optimal sets of parameters that maximize the near-field heat transfer are determined. It is seen that the real and imaginary parts of the dielectric function determine the location and width of the spectral heat flux peak, respectively. A smaller ε_∞ will result in an ε' close to -1 over a larger spectral region and is desired for near-field enhancement. For the Drude model, with increasing temperature, $\omega_{\mathrm{p,opt}}$ increases while $\gamma_{\mathrm{opt}}/\omega_{\mathrm{p,opt}}$ remains constant for maximum radiative transfer. For the Lorentz model, the maximum near-field heat flux monotonically decreases with increasing ω_0 for a given ε_∞. In other words, the Drude model $(\omega_0 = 0)$ when optimized provides the greatest near-field enhancement for any given ε_∞ and the near-field heat transfer is around one order of magnitude greater than that for any real material. Among the real materials, MgO provides greatest near-field enhancement since it has the smallest ε_∞ and the largest γ resulting in the broadest peak in the spectral heat flux curve.

While the objective of this dissertation is to study the near-field heat transfer between two semi-infinite parallel plates, it is important to estimate the physical dimensions of the emitter and the receiver for them to be considered semi-infinite. To this end, the unusual penetration depth and energy streamlines associated with near-field heat

transfer is investigated in this dissertation. Traditionally, the penetration depth in thermal radiation depends on the wave-length and extinction coefficient and is on the order of 1 micron. However, in case of near-field radiation, the penetration depth depends on the vacuum gap in addition to the material properties and the wavelength. When the vacuum gap between two parallel plates decreases the energy transfer is pushed towards larger β which reduces the penetration depth of the absorbed radiation. Such unusual behavior of penetration depth results in a 10 nm thick SiC film behaving as completely opaque when the vacuum gap is on the order of 10 nm. Also, the ultrasmall penetration depth in near-field radiation sets a limit on the minimum thickness of the emitter in order to avoid thermal emission from mono layers.

It is shown in this dissertation that simple thin film optics cannot be used to calculate energy streamlines in near-field radiation and a more rigorous approach using fluctuation electrodynamics is required. While predicting the streamlines in the emitter, vacuum gap, and the receiver, the direction of thermal emission must be correctly accounted for. Based on the analysis performed in this dissertation, it can be inferred that the lateral displacement of the streamlines inside the emitter can be greater than that in the vacuum gap or the receiver. As a result, it may not be correct to predict the lateral shift of energy streamlines based on the emitter. With increasing β, the magnitude of the z component of the Poynting vector decreases. Therefore, the lateral shift of the streamlines inside the emitter increases with β. However, due to the very small penetration depth, most of the energy is absorbed very close to the surface and the lateral shift inside the emitter can be considered to be $9d$.

In this dissertation, theoretical calculations of near-field heat transfer are limited to semi-infinite plane surfaces. There have also been a few studies on the near-field radiation between spheres due to the mathematical complexity involved in solving Maxwell's equations for bodies with arbitrary geometries. It will be interesting to study the near-field heat transfer between structured surfaces like gratings which will benefit the field of nanooptoelectronics. The study on near-field heat transfer between two spheres can be extended to that between spheres with coatings for biomedical applications. Instead of a semi-infinite homogenous emitter, a multilayered emitter can be used especially in TPV systems to provide greater spectral control of the thermal emission and thus improve their performances. Further study is also required in order to fully understand the effect of vacuum gap on the dielectric function of the materials participating in near-field radiation, especially at distances less than 1 nm. Furthermore, with the help of fluctuational electrodynamics, analysis of entropy generation during nanoscale radiation will help improve the efficiencies of near-field energy systems. However, it is difficult to define radiation entropy in the near-field regime, where the local density of states of photons is greatly enhanced due to photon tunneling and excitation of surface waves. At present, a satisfactory thermodynamic second-law interpretation of near-field thermal radiation does not exist. Nonequilibrium entropy needs to be employed to develop thermodynamic relations for near-field radiation and to provide a second-law analysis of photon tunneling and surface polariton phenomena.

Despite significant progress in understanding near-field thermal radiation, quantitative measurements remain a challenge at nanometer distances. It has only been in the past few years that there have been some meaningful measurement results in this

regard. In terms of difficulty, measuring near-field heat transfer between two flat surfaces is most challenging followed by that between sphere and flat surface and between two spheres. Surface roughness and non-parallelism of the heated plates make it very challenging to perform measurements between two flat plates at smaller vacuum gaps. Nevertheless, nanospacers such as dielectric nanowires or nanoparticles can be employed to achieve smaller vacuum gaps between two semi-infinite flat plates with little heat conduction. If one of the semi-infinite surfaces is replaced by a nanoparticle, then the heat flux is reduced and very sensitive instruments are required to detect the near-field enhancement. The problem associated with two semi-infinite surfaces or a nanoparticle and semi-infinite surface is overcome in the case of a microsphere and a flat surface. It is expected that this dissertation will aid in the material selection for optimization of near-field radiation.

It should be emphasized that improvement in computational resources and recent developments in nano/microfabrication techniques and the unprecedented growth in materials science in the past decade hold great promise for the future investigation and applications of near-field thermal radiative transfer. The field of nanoscale radiation is rich and exciting: it requires a deeper understanding of the interplay among optical, thermal, mechanical, and electrical properties of materials and structures at the nanoscale and it can have promising applications in biological sensing, materials processing and manufacturing, and energy systems.

REFERENCES

Antoniadis, D. A., Gonzalez, A. G., and Dutton, R. W., 1978, "Boron in Near-Intrinsic <100> and <111> Silicon under Inert and Oxidizing Ambients - Diffusion and Segregation," *Journal of Electrochemical Society*, Vol. 125, pp. 813-819.

Ashcroft, N. W., and Mermin, N. D., 1976, *Solid State Physics*, Saunders College, PA.

Baccarani, G., and Ostoja, P., 1975, "Electron-Mobility Empirically Related to Phosphorus Concentration in Silicon," *Solid-State Electronics*, Vol. 18, pp. 579-580.

Basu, S., Chen, Y. B., and Zhang, Z. M., 2007, "Microscale Radiation in Thermophotovoltaic Devices-A Review," *International Journal of Energy Research*, Vol. 31, pp. 689-716.

Basu, S., and Zhang, Z. M., 2009a, "Maximum Energy Transfer in Near-field Thermal Radiation at Nanometer Distances," *Journal of Applied Physics* Vol. 105, 093535.

Basu, S., and Zhang, Z. M., 2009b, "Ultrasmall Penetration Depth in Nanoscale Thermal Radiation," *Applied Physics Letters* Vol. 95, p. 133104.

Basu, S., Lee, B. J., and Zhang, Z. M., 2009a, "Infrared Radiative Properties of Heavily Doped Silicon at Room Temperature," *Journal of Heat Transfer* (in press).

Basu, S., Lee, B. J., and Zhang, Z. M., 2009b, "Near-field Radiation Calculated with an Improved Dielectric Function Model for Doped Silicon," *Journal of Heat Transfer* (accepted).

Basu, S., Zhang, Z. M., and Fu, C. J., 2009, "Review of Near-Field Thermal Radiation and its Application to Energy Conversion," *International Journal of Energy Research* (in press).

Beadle, W. E., Tsai, J. C. C., and Plummer, R. D., 1985, *Quick Reference Manual for Silicon Integrated Circuit Technology*, Wiley, N. Y.

Ben-Abdallah, P., Joulain, K., Drevellion, J., and Domingues, G., "Near-Field Heat Transfer Mediated by Surface Wave Hybridization between Two Films," Journal *of Applied Physics*, Vol. 106, p. 044306.

Biehs, S. A., 2007, “Thermal Heat Radiation, Near-field Energy Density and Near-field Radiative Heat Transfer of Coated Materials,” *European Physical Journal B*, Vol. 58, pp. 423-431.

Biehs, S. A., Reddig, D., and Holthaus, M., 2007, “Thermal Radiation and Near-field Energy Density of Thin Metallic Films,” *European Physical Journal B*, Vol. 55, pp. 237-251.

Biehs, S. A., Huth, O., and Ruting, F., 2008, “Near-field Radiative Heat Transfer for Structured Surfaces,” *Physical Review B*, Vol. 78, 085414.

Born, M., and Wolf, E., 1999, *Principles of Optics*, Cambridge University Press, UK.

Caughey, D. M., and Thomas, R. E., 1967, “Carrier Mobilities in Silicon Empirically Related to Doping and Field,” *Proceedings of the Institute of Electrical and Electronics Engineers*, Vol. 55, pp. 2192-2193.

Chapman, P. W., Tufte, O. N., Zook, J. D., and Long, D., 1963, “Electrical Properties of Heavily Doped Silicon,” *Journal of Applied Physics*, Vol. 34, pp. 3291-3295.

Chapuis, P. O., Volz, S., Henkel, C., Joulain, K., and Greffet, J. -J., 2008a, “Effects of Spatial Dispersion in Near-field Radiative Heat Transfer between Two Parallel Metallic Surfaces," *Physical Review B*, Vol. 77, p. 035431.

Chapuis, P. O., Laroche, M., Volz, S., and Greffet, J. -J., 2008b, “Radiative Heat Transfer between Metallic Nanoparticles,” *Applied Physics Letters*, Vol. 92, p. 201906.

Cravalho, E. G., Tien, C. L., and Caren, R. P., 1967, “Effect of Small Spacings on Radiative Transfer between Two Dielectrics,” *Journal of Heat Transfer*, Vol. 89, pp. 351-358.

De Wilde, Y., Formanek, F., Carminati, R., Gralak, B., Lemoine, P.A., Joulain, K., Mulet, J. P., Chen, Y., and Greffet, J. -J., 2006, “Thermal Radiation Scanning Tunneling Microscopy,” *Nature*, Vol. 444, pp. 740-743.

Domoto, G. A., Boehm, R. F., and Tien, C. L., 1970, “Experimental Investigation of Radiative Transfer between Metallic Surfaces at Cryogenic Temperatures,” *Journal of Heat Transfer*, Vol. 92, pp. 412-417.

Ebbesen, T. W., Lezec, H. J., Ghaemi, H. F., Thio, T., and Wolff, P. A., 1998, "Extraordinary Optical Transmission through Sub-wavelength Hole Arrays," *Nature*, Vol. 391, pp. 667-669.

Esaki, L., and Miyahara, Y., 1960, "A New Device Using the Tunneling Process in Narrow *p-n* Junctions," *Solid-State Electronics*, Vol. 1, pp. 13-21.

Finetti, M., Negrini, P., Solmi, S., and Nobili, D., 1981, "Electrical-Properties and Stability of Supersaturated Phosphorus-Doped Silicon Layers," *Journal of the Electrochemical Society*, Vol. 128, pp. 1313-1317.

Francoeur, M., and Menguc, M. P., 2008, "Role of Fluctuational Electrodynamics in Near-field Radiative Heat Transfer," *Journal of Quantitative Spectroscopy and Radiative Transfer*, Vol. 109, pp. 280-293.

Francoeur, M., Menguc, M. P., and Vaillon, R., 2008, "Near-field Radiative Heat Transfer Enhancement via Surface Phonon Polaritons Coupling in Thin Films," *Applied Physics Letters*, Vol. 93, p. 043109.

Francoeur, M., Menguc, M. P., and Vaillon, R., 2009, "Solution of Near-Field Thermal Radiation in One-Dimensional Layered Media using Dyadic Green's Functions and the Scattering Matrix Method," *Journal of Quantitative Spectroscopy and Radiative Transfer*, Vol. 110, pp. 2002-2018.

Fu, C. J., and Zhang, Z. M., 2006, "Nanoscale Radiation Heat Transfer for Silicon at Different Doping Levels," *International Journal of Heat and Mass Transfer*, Vol. 49, pp. 1703-1718.

Fu, C. J., and Tan, W. C., 2009, "Near-field Radiative Heat Transfer between Two Plane Surfaces with One having a Dielectric Coating," *Journal of Quantitative Spectroscopy and Radiative Transfer*, Vol. 110, pp. 1027-1036.

Gaylord, T. K., and Linxwiler, J. N., 1976, "Method for Calculating Fermi Energy and Carrier Concentrations in Semiconductors," *American Journal of Physics*, Vol. 44, pp. 353-355.

Griffiths, D. J., 1999, *Introduction to Electrodynamics*, Prentice Hall, N.J.

Hargreaves, C. M., 1969, "Anomalous Radiative Transfer between Closely Spaced Bodies," *Physics Letters A*, Vol. 30, pp. 491-492.

Hargreaves, C. M., 1973, "Radiative Transfer between Closely Spaced Bodies," *Philips Research Reports and Supplement*, Vol. 5, pp. 1-80.

Hesketh, P. J., Zemel, J. N., and Gebhart, B., 1988, "Polarized Spectral Emittance from Periodic Micromachined Surfaces. II. Doped Silicon - Angular Variation," *Physical Review B*, Vol. 37, pp. 10803-10813.

Howarth, L. E., and Gilbert, J. F., 1963, "Determination of Free Electron Effective Mass of *n*-type Silicon," *Journal of Applied Physics*, Vol. 34, pp. 236-237.

Hu, L., Narayanaswamy, A., Chen, X., and Chen, G., 2008, "Near-Field Thermal Radiation between Two Closely Spaced Glass Plates Exceeding Planck's Blackbody Radiation Law," *Applied Physics Letters*, Vol. 92, p. 133106.

Joulain, K., Mulet, J. P., Marquier, F., Carminati, R., and Greffet, J. -J., 2005, "Surface Electromagnetic Waves Thermally excited: Radiative Heat Transfer, Coherence Properties and Casimir Forces Revisited in the Near Field," *Surface Science Reports*, Vol. 57, pp. 59-112.

Joulain, K., 2008, "Near-field Heat Transfer: A Radiative Interpretation of Thermal Conduction," *Journal of Quantitative Spectroscopy and Radiative Transfer*, Vol. 109, pp. 294-304.

Kittel, A., Muller-Hirsch, W., Parisi, J., Biehs, S. A., Reddig, D., and Holthaus, M., 2005, "Near-field Heat Transfer in a Scanning Thermal Microscope," *Physical Review Letters*, Vol. 95, p. 224301.

Kittel, A., Wischnath, U. F., Welker, J., Huth, O., Ruting, F., and Biehs, S. A., 2008. Near-field Thermal Imaging of Nanostructured Surfaces. *Applied Physics Letters* Vol. 93, p. 193109.

Kuzmicz, W., 1986, "Ionization of Impurities in Silicon," *Solid-State Electronics*, Vol. 29, pp. 1223-1227.

Laroche, M., Carminati, R., and Greffet, J. -J., 2006, "Near-field Thermophotovoltaic Energy Conversion," *Journal of Applied Physics*, Vol. 100, p. 063704.

Lee, B. J., Khuu, V. P., and Zhang, Z. M., 2005, "Partially Coherent Spectral Transmittance of Dielectric Thin Films with Rough Surfaces," *Journal of Thermophysics and Heat Transfer*, Vol. 19, pp. 360-366.

Lee, B. J., Park, K., and Zhang, Z. M., 2007, "Energy Pathways in Nanoscale Thermal Radiation," *Applied Physics Letters*, Vol. 91, p. 153101.

Lee, B. J., and Zhang, Z. M., 2008, "Lateral Shifts in Near-field Thermal Radiation with Surface Phonon Polaritons," *Nanoscale and Microscale Thermophysical Engineering*, Vol. 12, pp. 238-250.

Lee, B. J., Chen, Y. B., and Zhang, Z. M., 2008, "Confinement of Infrared Radiation to Nanometer Length Scales through Metallic Slit Arrays," *Journal of Quantitative Spectroscopy and Radiative Transfer*, Vol. 109, pp. 608-619.

Liu, Z. W., Wei, Q. H., and Zhang, X., 2005, "Surface Plasmon Interference Nanolithography," *Nano Letters*, Vol. 5, pp. 957-961.

Loomis, J. J., and Maris, H. J., 1994, "Theory of Heat Transfer by Evanescent Electromagnetic Waves," *Physical Review B*, Vol. 50, pp. 18517-18524.

Marquier, F., Joulain, K., Mulet, J. P., Carminati, R., and Greffet, J. -J., 2004, "Engineering Infrared Emission Properties of Silicon in the Near Field and the Far Field," *Optics Communications*, Vol. 237, pp. 379-388.

Masetti, G., Severi, M., and Solmi, S., 1983, "Modeling of Carrier Mobility against Carrier Concentration in Arsenic-doped, Phosphorus-doped, and Boron-doped Silicon," *IEEE Transaction on Electron Devices*, Vol. 30, pp. 764-769.

May, G. S., and Sze, S. M., 2004, *Fundamentals of Semiconductor Fabrication*, Wiley, N. Y.

Morin, F. J., and Maita, J. P., 1954, "Electrical Properties of Silicon Containing Arsenic and Boron," *Physical Review*, Vol. 96, pp. 28-35.

Mousty, F., Ostoja, P., and Passari, L., 1974, "Relationship between Resistivity and Phosphorus Concentration in Silicon," *Journal of Applied Physics*, Vol. 45, pp. 4576-4580.

Mulet, J. P., Joulain, K., Carminati, R., and Greffet, J. -J., 2001, "Nanoscale Radiative heat Transfer between A Small Particle and a Plane Surface," *Applied Physics Letters*, Vol. 78, pp. 2931-2933.

Mulet, J. P., Joulain, K., Carminati, R., and Greffet, J. -J., 2002, "Enhanced Radiative Heat Transfer at Nanometric Distances," *Nanoscale and Microscale Thermophysical Engineering*, Vol. 6, pp. 209-222.

Narayanaswamy, A., and Chen, G., 2003, "Surface Modes for Near-field Thermophotovoltaics," *Applied Physics Letters*, Vol. 82, pp. 3544-3546.

Narayanaswamy, A., and Chen, G., 2008, "Thermal Near-field Radiative Transfer between Two Spheres," *Physical Review B*, Vol. 77, p. 075125.

Narayanaswamy, A., Shen, S., and Chen, G., 2008, "Near-field Radiative Heat Transfer between a Sphere and a Substrate," *Physical Review B*, Vol. 78, p.115303.

Palik, E. D., 1985, *Handbook of Optical Constants of Solids*, Academic Press, Orlando.

Pan, J. L., 2000, "Radiative Transfer over Small Distances from a Heated Metal," *Optics Letters*, Vol. 25, pp. 369-371.

Pan, J. L., Choy, H. K. H., and Fonstad, C. G., 2000, "Very Large Radiative Transfer over Small Distances from a Black Body for Thermophotovoltaic Applications," *IEEE Transactions on Electron Devices*, Vol. 47, pp. 241-249.

Park, K., Lee, B. J., Fu, C., and Zhang, Z. M., 2005, "Study of the Surface and Bulk Polaritons with a Negative Index Metamaterial," *Journal of the Optical Society of America B*, Vol. 22, pp. 1016-1023.

Park, K., Basu, S., King, W. P., and Zhang, Z. M., 2008, "Performance Analysis of Near-field Thermophotovoltaic Devices Considering Absorption Distribution," *Journal of Quantitative Spectroscopy and Radiative Transfer*, Vol. 109, pp. 305-316.

Park, K., Marchenkov, A., Zhang, Z. M., and King, W. P., 2007, "Low Temperature Characterization of Heated Microcantilevers," *Journal of Applied Physics*, Vol. 101, p. 094504.

Pendry, J. B., 1999, "Radiative Exchange of Heat between Nanostructures," *Journal of Physics-Condensed Matter*, Vol. 11, pp. 6621-6633.

Polder, D., and Van Hove. M., 1971, "Theory of Radiative Heat Transfer between Closely Spaced Bodies," *Physical Review B*, Vol. 4, pp. 3303-3314.

Riffe, D. M., 2002, "Temperature Dependence of Silicon Carrier Effective Masses with Application to Femtosecond Reflectivity Measurements," *Journal of the Optical Society of America B*, Vol. 19, pp. 1092-1100.

Rytov, S. M., Kr avtsov, Y. A., and Tatarski V. I., 1987, *Principles of Statistical Radiophysics*, Springer-Verlag, N. Y.

Shen, S., Narayanaswamy, A., and Chen, G., 2009, "Surface Phonon Polaritons Mediated Energy Transfer between Nanoscale Gaps," *Nano Letters*, Vol. 9, pp. 2909-2913.-

Siegel, R., and Howell, J. R., 2002, *Thermal Radiation Heat Transfer*, Taylor & Francis, NY.

Sipe, J., 1987, "New Green-Function Formalism for Surface Optics," *Journal of the Optical Society of America B*, Vol. 4, pp. 481-489.

Sze, S. M., and Irvin, J. C., 1968, "Resistivity, Mobility, and Impurity Levels in GaAs, Ge and Si at 300 K," *Solid-State Electronics*, Vol. 11, pp. 599-602.

Thurber, W. R., Mattis, R. L., Liu, Y. M., and Filliben, J. J., 1980, "Resistivity-Dopant Density Relationship for Boron-Doped Silicon," *Journal of the Electrochemical Society*, Vol. 127, pp. 2291-2294.

Thurber, W. R., Mattis, R. L., Liu, Y. M., and Filliben, J. J., 1980, "Resistivity-Dopant Density Relationship for Phosphorus-Doped Silicon," *Journal of the Electrochemical Society*, Vol. 127, pp. 1807-1812.

Tsang, L., Kong, J. A., and Ding, K. H., 2000, *Scattering of Electromagnetic Waves: Theories and Applications*, Wiley, N.Y.

Volokitin, A. I., and Persson, B. N. J., 2001, "Radiative Heat Transfer between Nanostructures," *Physical Review B*, Vol. 63, p. 205404.

Volokitin, A. I., and Persson, B. N. J., 2004, "Resonant Photon Tunneling Enhancement of the Radiative Heat Transfer," *Physical Review B*, Vol. 69, p. 045417.

Wagner, S., 1972, "Diffusion of Boron from Shallow Ion Implants in Silicon," *Journal of the Electrochemical Society*, Vol. 119, pp. 1570-1576.

Wang, L., Uppuluri, S. M., Jin, E. X., and Xu, X. F., 2006, "Nanolithography Using High Transmission Nanoscale Bowtie Apertures," *Nano Letters*, Vol. 6, pp. 361-364.

Wang, X. J., Basu, S., and Zhang, Z. M., 2009, "Parametric Optimization of Dielectric Functions for Maximizing Nanoscale Radiative Transfer," *Journal of Physics D: Applied Physics* (submitted).

Williams, C. C., and Wickramasinghe, H. K., 1986, "Scanning Thermal Profiler," *Applied Physics Letters*, Vol. 49, pp. 1587-1589.

Xu, J. B., Lauger, K., Moller, R., Dransfeld, K., and Wilson, I. H., 1994, "Heat Transfer between Two Metallic Surfaces at Small Distances," *Journal of Applied Physics* Vol. 76, pp. 7209-7216.

Zhang, Z. M., Hanssen, L. M., Datla, R. U., and Drew, H. D., 1996, "An Apparatus for Infrared Transmittance and Reflectance Measurements at Cryogenic Temperatures," *International Journal of Thermophysics*, Vol. 17, pp. 1441-1454.

Zhang, Z. M., and Fu, C. J., 2002, "Unusual Photon Tunneling in the Presence of a Layer with a Negative Refractive Index," Applied Physics Letters, Vol. 80, pp. 1097-1099.

Zhang, Z. M., and Wang, X. J., 2009, "Unified Wien's Displacement Law in Terms of the Logarithmic Frequency or Wavelength Scale," *Journal of Thermophysics and Heat Transfer* (accepted).

Zhang, Z. M., 2007, *Nano/Microscale Heat Transfer*, McGraw-Hill, N.Y.